Conformational and Spin Effects in Single-Molecule Electronic Transport

Hsu, C.

DOI
10.4233/uuid:1d3b6977-0abf-40fa-bc94-b7617e158b81

Publication date
2022

Document Version
Final published version

Citation (APA)
Hsu, C. (2022). *Conformational and Spin Effects in Single-Molecule Electronic Transport*. [Dissertation (TU Delft), Delft University of Technology]. https://doi.org/10.4233/uuid:1d3b6977-0abf-40fa-bc94-b7617e158b81

Important note
To cite this publication, please use the final published version (if applicable).
Please check the document version above.

Conformational and Spin Effects in Single-Molecule Electronic Transport

Conformational and Spin Effects in Single-Molecule Electronic Transport

Proefschrift

ter verkrijging van de graad van doctor
aan de Technische Universiteit Delft,
op gezag van de Rector Magnificus Prof.dr.ir. T.H.J.J. van der Hagen,
voorzitter van het College voor Promoties,
in het openbaar te verdedigen op vrijdag 4 November 2022 om 12:30 uur

door

Chunwei HSU

Master of Science in Applied Physics,
Delft University of Technology, Delft, The Netherlands,
geboren te Tainan, Taiwan.

Dit proefschrift is goedgekeurd door de promotoren.

Samenstelling promotiecommissie bestaat uit:

Rector Magnificus,	voorzitter
Prof. dr. ir. H. S. J. van der Zant,	Technische Universiteit Delft, promotor
Prof. dr. ir. J. M. Thijssen,	Technische Universiteit Delft, promotor

Onafhankelijke leden:

Prof. dr. F. Grozema,	Technische Universiteit Delft
Prof. dr. M. Mayor,	Universität Basel, Zwitserland
Prof. dr. F. Pauly,	Universität Augsburg, Duitsland
Prof. dr. P. Gehring,	Université catholique de Louvain, België
Prof. dr. N. Agraït,	Universidad Autónoma de Madrid, Spanje
Prof. dr. Y. M. Blanter,	Technische Universiteit Delft, reservelid

Keywords: single-molecule, molecular electronics, Kondo effect, thermoelectricity, mechanosensitivity, quantum interference, break junction, chirality-induced spin selectivity, quantum dot

Printed by: Gilderprint, Enschede

Front & Back: Depiction of a single-molecule break junction & Thermocurrent Coulomb stability diagram of a single-molecule junction. Image: Chunwei Hsu

Casimir PhD Series, Delft-Leiden 2022-26

ISBN 978-90-8593-537-7

An electronic version of this dissertation is available at
http://repository.tudelft.nl/.
The associated experimental data for this dissertation are available at
http://doi.org/10.4121/20017610.

The first principle is that you must not fool yourself — and you are the easiest person to fool.

Richard Feynman

Contents

Summary

This dissertation presents the experimental work on single-molecule charge transport, particularly on the aspects of spin and orbital conformational effects in single-molecule junctions. In this dissertation, we employ and develop various single-molecule techniques, the mechanically controlled break junction (MCBJ), thermoelectric electromigrated break junction (Th-EMBJ) and reversible spin Hall junction (RSHJ), to characterize the spin and conformational effects beyond simple charge transport.

In **Chapter 1**, we give a brief introduction to the field of molecular electronics and single-molecule charge transport studies. We discuss how careful single-molecule electrical characterization can unveil the rich physics of molecular junctions beyond charge transport, in particular conformational and spin effects. This also draws the outline of this dissertation, which includes the studies of conformational, spin and spin-orbit effects in single-molecule junctions.

Chapter 2 introduces the experimental methods and theoretical background for the work presented in this dissertation. First, we show the fabrication steps and working principles of MCBJ and Th-EMBJ devices, which we use extensively in other chapters. We then continue the discussion of the relevant theoretical background in single-molecule charge transport. This includes the Landauer formula, the weak-coupling regime and thermoelectric effects in single-molecule junctions.

In **Chapter 3**, we present experiments on conformation-induced quantum interference (QI) features in paracyclophane (PCP)-based and porphyrin-based (PC1) molecules. In the case of PCP, we show that the rules of constructive and destructive QI for paracyclophanes are the opposite from those in benzene rings. This means that for a *para* connection to the PCP, destructive QI (DQI) is present; whereas for a *meta* connection to the PCP, constructive QI (CQI) is manifested. In the case of PC1 molecules, we focus on studying the DQI features in the molecular junction. We observe multiple QI dip features when we apply mechanical manipulation in a single-molecule junction; this suggests several orbital energy crossings as a result of conformational changes.

Chapter 4 focuses on a mechanosenstive molecule. In this chapter, we study a porphyrin double-decker (PC2), where a two-order-of-magnitude conductance increase is observed in fast-breaking measurements *via* MCBJ. This feature is unique for its conductance upturn while stretching, which has never been observed before in organic molecules. This behavior is explained by an elegant interplay between the through-bond and through-space transport pathways in the single-molecule junction.

In **Chapter 5**, we introduce the first simultaneous electrical and thermoelectric measurement at the single-molecule level. This novel technique, for measuring the

thermocurrent in single-molecule junctions, is capable of capturing the full thermoelectric properties of molecular junctions. We further show that we can use this technique to obtain another thermodynamic quantity, the entropy difference, between different charge states.

Chapter 6 is dedicated to the application of this thermocurrent spectroscopy technique in studying more exotic systems. In this chapter, we measure a strongly Kondo-correlated molecular quantum dot, in which a clear zero-bias anomaly is observed. With the application of a finite temperature difference across the two electrodes, we realize a new hallmark of the Kondo effect, defined in terms of the thermocurrent. Specifically, the slope of zero-bias thermocurrent changes its sign when the critical magnetic field, B_c is reached. This is shown to be an universal feature of the Kondo effect and suggests the great potential of thermocurrent spectroscopy in studying fundamental transport processes.

Chapter 7 concerns the study of chirality-induced spin selectivity (CISS) in single-molecule junctions. The CISS effect is the phenomenon where a chiral molecule has charge transport properties that are spin dependent. This effect has opened a whole new field of molecular spintronics based on chiral molecules; however, its origin is still controversial. In this chapter, we aim to develop a novel technique to characterize the CISS effect at the single-molecule level, as in the community no experimental attempt has succeeded in demonstrating this unambiguously so far. We first show the MCBJ characterization of chiral molecules for the CISS study. We present the development of devices for the CISS study, including a H-shape platinum junction and the reversible spin Hall junction (RSHJ). In particular, we also propose a few measurement protocols using the RSHJ devices and the possible measurement outcomes.

Finally, we give an outlook for the study of conformational and spin effects in single-molecule junctions in **Chapter 8**.

Samenvatting

Dit proefschrift presenteert de experimenteel werk over ladingstransport van één molecuul, in het bijzonder over de aspecten van spin- en orbitale conformationele effecten in juncties van één molecuul. In dit proefschrift gebruiken en ontwikkelen we meerdere single-molecule technieken, de mechanisch gecontroleerde breekjunctie (MCBJ) en thermo-elektrische geëlektromigreerde breekjunctie (Th-EMBJ) en reversibele spin Hall junctie (RSHJ), om de spin- en conformationele effecten te karakteriseren die verder gaan dan eenvoudig ladingstransport.

In **Chapter 1** geven we een korte introductie op het gebied van moleculaire elektronica en enkel-molecuul ladingstransport studies. We bespreken hoe zorgvuldige elektrische karakterisering van een enkel molecuul de rijke fysica van moleculaire juncties buiten ladingstransport kan onthullen, in het bijzonder conformationele en spin-effecten. Dit schetst ook de contouren van dit proefschrift, dat de studies van conformationele, spin- en spin-baaneffecten in juncties van een enkel molecuul.

Chapter 2 introduceert de experimentele methoden en theoretische achtergrond voor de werken die in dit proefschrift worden gepresenteerd. Eerst laten we de fabricagestappen en werkingsprincipes zien van MCBJ- en Th-EMBJ-apparaten, die we in andere hoofdstukken uitgebreid hebben gebruikt. Vervolgens gaan we verder met de bespreking van de relevante theoretische achtergrond in het ladingstransport van een enkel molecuul. Dit omvat de Landauer-formule, het zwakke koppelingsregime en thermo-elektrische effecten in juncties met één molecuul.

In **Chapter 3** presenteren we experimenten met conformatie-geïnduceerde kwantuminterferentie (QI) kenmerken in op paracyclofaan (PCP) gebaseerde en op porfyrine gebaseerde (PC1) moleculen. In het geval van PCP laten we zien dat de regels van constructieve en destructieve QI voor paracyclofanen het tegenovergestelde zijn van die in benzeenringen. Dit betekent dat voor een *para* verbinding met de PCP destructieve QI (DQI) aanwezig is; terwijl voor een *meta*-verbinding met de PCP constructieve QI (CQI) wordt gemanifesteerd. In het geval van PC1-moleculen concentreren we ons op het bestuderen van de DQI-kenmerken in de moleculaire junctie. We observeren meerdere QI-dip-functies wanneer we mechanische manipulatie toepassen in een junctie van één molecuul; dit suggereert verschillende orbitale energieovergangen als gevolg van conformationele veranderingen.

Chapter 4 richt zich op een mechanosenstief molecuul. In dit hoofdstuk bestuderen we een porfyrine dubbeldekker (PC2), waar een twee-orde-van-magnitude geleidbaarheidstoename wordt waargenomen in snelle metingen *via* MCBJ. Deze eigenschap is uniek vanwege de toeneemende geleiding tijdens het strekken, wat nog nooit is waargenomen in organische moleculen. Dit gedrag wordt verklaard door een elegant samenspel tussen de moleculaire bindingen en transportroutes door de ruimte in juncties met een enkel molecuul.

In **Chapter 5** introduceren we de eerste gelijktijdige elektrische en thermo-elektrische meettechniek op het niveau van een enkel molecuul. Deze nieuwe techniek, om de thermostroom in juncties met een enkel molecuul te meten, is in staat om de volledige thermo-elektrische eigenschappen van moleculaire juncties vast te leggen. We laten verder zien dat we deze techniek kunnen gebruiken om een andere thermodynamische grootheid te verkrijgen, het entropieverschil, tussen verschillende ladingstoestanden.

Chapter 6 is gewijd aan de toepassing van deze thermostroom spectroscopie techniek bij het bestuderen van exotischere systemen. In dit hoofdstuk meten we een sterke Kondo-gecorreleerde moleculaire kwantumdot, waarin een duidelijke nul-bias anomalie wordt waargenomen. Met de toepassing van een eindig temperatuurverschil tussen de twee elektroden realiseren we een nieuw kenmerk van het Kondo-effect, gedefinieerd in termen van de thermostroom. In het bijzonder verandert de helling van de thermostroom bij nul voltage van teken wanneer het kritische magnetische veld B_c wordt bereikt. Dit is aangetoond een universeel kenmerk van het Kondo-effect te zijn en suggereert het grote potentieel van thermostroomspectroscopie bij het bestuderen van fundamentele transportprocessen.

Chapter 7 betreft de studie van chiraliteit-geïnduceerde spin-selectiviteit (CISS) in juncties van een enkel molecuul. Het CISS-effect is de transporteigenschappen van electronen door een chiraal molecuul spin-afhankelijk zijn. Dit effect heeft een heel nieuw veld van moleculaire spintronica geopend op basis van chirale moleculen; de oorsprong ervan is echter nog steeds controversieel. In dit hoofdstuk willen we een nieuwe techniek ontwikkelen om het CISS-effect op het niveau van een enkel molecuul te karakteriseren, aangezien in de gemeenschap tot nu toe geen enkele experimentele poging hiertoe ondubbelzinnig is geslaagd. We tonen eerst de MCBJ-karakterisering van chirale moleculen voor de CISS-studie. We presenteren de ontwikkeling van apparaten voor de CISS-studie, waaronder een H-vormige platina-overgang en de omkeerbare spin Hall-overgang (RSHJ). In het bijzonder stellen we ook enkele meetprotocollen voor met behulp van de RSHJ-apparaten en de mogelijke meetresultaten.

Ten slotte geven we in **Chapter 8** een vooruitblik op de studie van conformationele en spin-effecten in juncties van enkele moleculen.

1

Introduction

In this chapter, we introduce the field of molecular electronics and single-molecule charge transport. We discuss conceptually the interplay between conformational and spin effects in a single-molecule system. This idea leads to the three main topics in this dissertation: mechanosensitive molecules, thermoelectricity in single-molecule junctions and the chirality-induced spin selectivity effect.

1

1.1. Molecular electronics and single-molecule studies

Molecular electronics is the field of research which aims to utilize molecules as building blocks for electronic applications. The idea of constructing electronic components with molecules was introduced as early as in 1956 [1]. However, the real commencement of the field of molecular electronics is only after the revolutionary proposal by Aviram and Ratner for a molecular rectifier in 1974 [2]. Ever since, there have been a lot of efforts to experimentally realize molecule-based electronic devices. In the development of molecular electronics, the field has progressed in two main directions: single-molecule and molecular-layer studies. The main difference between the two approaches is the number of molecules involved in charge transport of the molecular devices. While both are valid approaches in making electronic components, it is the single-molecule studies which significantly improve our fundamental understanding of charge transport at the nanoscale, which may lead to electronic devices with the size of an individual molecule.

The main obstacle in the development of single-molecule devices was the lack of reliable methods for electrically contacting individual molecules. Fortunately, in the 1990s, there were a few important experimental breakthroughs in contacting single molecules with metallic electrodes. These single-molecule techniques are the scanning tunneling microscopy (STM) [3], mechanically controlled break junction (MCBJ) [4] and electromigrated break junction (EMBJ) [5, 6]. These have brought the single-molecule approach to a level where it has become a platform for studying novel physics and innovative applications. By now, there have been many experimentally demonstrated proof-of-concept single-molecule devices such as molecular wires [7, 8], rectifiers [9, 10], switches [11], optical switches [12, 13], thermoelectric devices[14, 15], mechanical sensors [16, 17], etc.

From a fundamental point of view, the single-molecule approach is more comprehensive than standard electronic transport. Single-molecule junctions provide the opportunity to study microscopic physical processes, including mechanics, thermoelectrics, spintronics or optoelectronics [18, 19]. These studies led to the discovery of peculiar physical phenomena including the Kondo effect [20], quantum interference [21, 22], inelastic tunneling [23], spin crossover [24], spin blockade[25], Yu-Shiba-Rusinov states [26, 27]. The single-molecule studies have thus provided countless examples of interesting physics and continue to serve as a platform for the research of novel physics and chemistry.

1.2. Orbital and spin effects in molecules

Molecular orbital (MO) is a mathematical description of the electronic wave functions in a molecule in the so-called independent-particle picture. Within this picture, a MO describes how an electron interacts with the nuclei and the average electric field generated by the other electrons. In MOs, electrons are filled from the lowest energy level according to the Aufbau principle; the electron spin configuration of the MOs follows the Hund's rule, as a result of the Pauli exclusion principle. MO is an important starting point for understanding and predicting the chemical and

physical properties of a molecule [28]. In the context of molecular electronics, MO is also the essential basis to study the electronic properties of a molecule. Particularly, it is crucial to address the highest occupied molecular orbital (HOMO) and the lowest unoccupied molecular orbital (LUMO), when one discusses charge transport in molecular junctions. The HOMO and LUMO are the closest MOs to the Fermi energy, which contribute significantly to charge transport in molecular junctions. They are analogous to the conduction band and valence band in a solid state system. The energetic arrangement of HOMO and LUMO governs the basic charge transport properties. However, to explore the more exotic physical phenomena in molecular systems, other degrees of freedom, need to be considered. For this, two important elements in MOs, conformational changes and spin configurations, are commonly examined in realizing novel physics beyond basic charge transport in single-molecule junctions.

1.2.1. Conformational change and mechanics

At the single-molecule level, the geometry of MOs in a molecule determines the probable junction configurations. Conversely, any conformational rearrangement of the molecular junction, and thus MO geometry, can cause a substantial modification of electronic transport in a single-molecule junction. This change can be purely due to the geometrical rearrangement of MOs, where the orbitals are displaced mechanically, and thus modifies their overlaps. Such a displacement can lead to the reduction or enhancement of through-bond and/or through-space coupling between the MOs, and therefore influence electronic transport in a single-molecule junction [22, 29]. Alternatively, the change of electronic transport can also be caused by a mechanically induced rearrangement of the MO energy levels. When multiple MOs are nearly degenerate, the electrons with the same energy can take multiple pathways, which can induce constructive or destructive quantum interference features in electronic transport [17, 30, 31]. The change of MOs by mechanical manipulation (mechanosensitivity), demonstrates the possibility to modify charge transport in a single-molecule junction.

1.2.2. Spin configuration and thermoelectricity

Another fundamental aspect of MOs is the spin configuration that follows the Hund's rule. In the weak coupling limit, the Pauli exclusion principle suggests that in a single-molecule junction, the type of electron spin allowed to cross a molecule from the electrodes is correlated with the electron spin that resides on the molecule. For example, in the absence of spin-flip, a singly occupied MO in a single-molecule junction only allows electrons with a particular spin orientation to cross the junction, following the Pauli exclusion principle; on the other hand, an unoccupied MO in a single-molecule junction allows both spin-up and spin-down electrons to sequentially tunnel from the source electrode to the MO and then to the drain electrode. Therefore, the exact spin ground state of a particular MO level provides information for spin-dependent charge transport. This leads to spin related phenomena in single-molecule junctions such as the aforementioned spin blockade [25], Kondo effect [20] and ground state spin transition [24], where electronic transport is spin

dependent.

Beyond the simple charge transport in single-molecule junctions by the application of bias voltage, these spin systems are particularly interesting to study in the context of thermodynamics. This is because spin configurations in MOs provide the occupation probability of an electron, and are thus directly related to the electronic entropy of the system. Thermoelectric studies provide a means to characterize these thermodynamic properties of a single-molecule junction, such as the spin transition between different MOs [32], and complement charge transport studies at finite bias voltage [33].

1.2.3. Spintronics and chiral molecules

The interplay of the molecular orbital conformation and spin configuration is yet another interesting concept to consider for spin-electronic transport in single-molecule junctions. In solid state systems, such interaction of spin-orbit coupling has led to many unconventional physical effects, such as the spin Hall effect, anomalous Hall effect and Rashba effect, etc. Therefore, it is intriguing to consider if similar effects can manifest themselves in single-molecule junctions. A particularly interesting subject regarding the MO conformation and spin-dependent transport is the chirality-induced spin selectivity (CISS) effect [34]. Originally, the CISS effect was studied in systems with large assemblies of chiral molecules [35]. It was proposed that due to the breaking of mirror symmetry, the spins of the transport electrons are polarized according to the chirality of the molecules. While the origin is still being debated, it demonstrates a possible novel combined effect of spin and orbital conformation in the context of charge transport in molecular junctions.

1.3. Dissertation outline

In this dissertation, we investigate charge transport in single-molecule junctions. Particularly, we study the conformational and spin effects that change the charge transport properties in single molecules. Figure 1.1 summarizes the approaches which we employ to study the conformational, spin and "spin-orbit" effects in single-molecule junctions. These effects are discussed in three different parts in this dissertation. First, we study how conformational effects influence charge transport in mechanosensitive molecules, by introducing mechanical manipulation in single-molecule junctions. In the second part, we study spin effects, such as the spin entropy and the Kondo effect, in radical molecules *via* thermoelectricity, where we apply a temperature difference across single-molecule junctions. Finally, we study the combined spin and conformational effect, the "CISS" effect, in chiral molecules.

The outline of this dissertation is described in the following. After this introductory chapter, the relevant experimental methods and theoretical background are discussed in chapter 2. We then discuss the mechanosensitive molecules in chapter 3 and 4. In chapter 3, we study how quantum interference, originating from energy crossings between molecular orbitals, can be tuned by mechanical deformation of the molecular structures. In chapter 4, we focus on a molecular conductance characteristic, where a two-order-of-magnitude conductance increase is observed

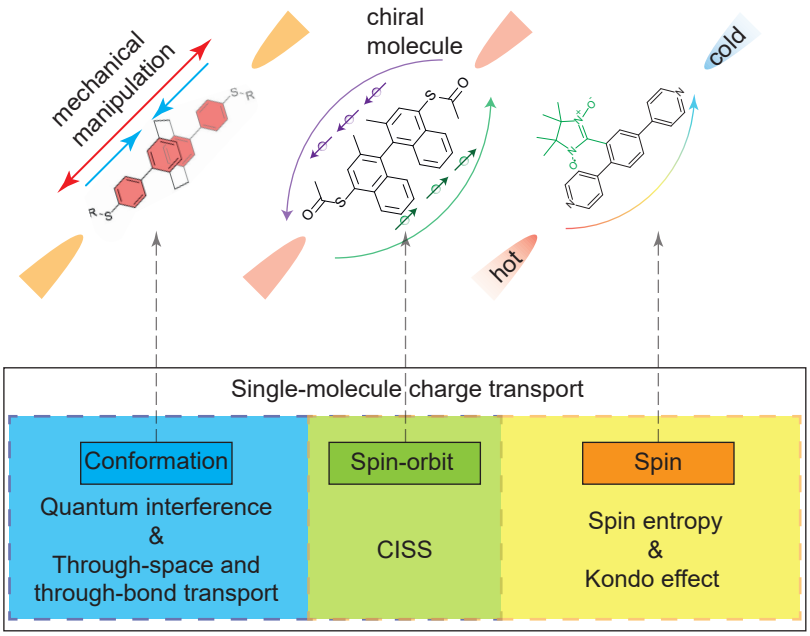

Figure 1.1: Outline of this dissertation. In this dissertation, we investigate the conformational, spin and the combined "spin-orbit" effect in single-molecule junctions. We go beyond the basic charge transport by including mechanics, thermoelectricity and spin-polarized current in single-molecule junctions.

while stretching the molecule, as a result of an elegant interplay between through-space and through-bond transport. Chapter 5 and 6 concern thermoelectric studies in single-molecule junctions. Particularly, in chapter 5, we demonstrate the ability to obtain thermoelectric properties and the entropy changes between charge states in single-molecule junctions. We apply the same technique in chapter 6 to study the magnetic-field dependent universality of the Kondo effect. Finally, in chapter 7, we present the development of experimental platforms for studying the CISS effect at the single-molecule level.

References

(1) Von Hippel, A. *Science* **1956**, *123*, 315–317.

(2) Aviram, A.; Ratner, M. A. *Chemical Physics Letters* **1974**, *29*, 277–283.

(3) Joachim, C.; Gimzewski, J. K.; Schlittler, R. R.; Chavy, C. *Physical Review Letters* **1995**, *74*, 2102–2105.

(4) Reed, M. A.; Zhou, C.; Muller, C. J.; Burgin, T. P.; Tour, J. M. *Science* **1997**, *278*, 252–254.

(5) Park, H.; Lim, A. K.; Alivisatos, A. P.; Park, J.; McEuen, P. L. *Applied Physics Letters* **1999**, *75*, 301–303.

(6) Park, H.; Park, J.; Lim, A. K. L.; Anderson, E. H.; Alivisatos, A. P.; McEuen, P. L. *Nature* **2000**, *407*, 57–60.

(7) Luo, L.; Choi, S. H.; Frisbie, C. D. *Chemistry of Materials* **2011**, *23*, 631–645.

(8) Huber, R.; González, M. T.; Wu, S.; Langer, M.; Grunder, S.; Horhoiu, V.; Mayor, M.; Bryce, M. R.; Wang, C.; Jitchati, R.; Schönenberger, C.; Calame, M. *Journal of the American Chemical Society* **2008**, *130*, 1080–1084.

(9) Elbing, M.; Ochs, R.; Koentopp, M.; Fischer, M.; von Hanisch, C.; Weigend, F.; Evers, F.; Weber, H. B.; Mayor, M. *Proceedings of the National Academy of Sciences* **2005**, *102*, 8815–8820.

(10) Lörtscher, E.; Gotsmann, B.; Lee, Y.; Yu, L.; Rettner, C.; Riel, H. *ACS Nano* **2012**, *6*, 4931–4939.

(11) Irie, M.; Fukaminato, T.; Sasaki, T.; Tamai, N.; Kawai, T. *Nature* **2002**, *420*, 759–760.

(12) Dulić, D.; van der Molen, S. J.; Kudernac, T.; Jonkman, H. T.; de Jong, J. J. D.; Bowden, T. N.; van Esch, J.; Feringa, B. L.; van Wees, B. J. *Physical Review Letters* **2003**, *91*, 207402.

(13) Kim, Y.; Hellmuth, T. J.; Sysoiev, D.; Pauly, F.; Pietsch, T.; Wolf, J.; Erbe, A.; Huhn, T.; Groth, U.; Steiner, U. E.; Scheer, E. *Nano Letters* **2012**, *12*, 3736–3742.

(14) Naher, M.; Milan, D. C.; Al-Owaedi, O. A.; Planje, I. J.; Bock, S.; Hurtado-Gallego, J.; Bastante, P.; Abd Dawood, Z. M.; Rincón-García, L.; Rubio-Bollinger, G.; Higgins, S. J.; Agraït, N.; Lambert, C. J.; Nichols, R. J.; Low, P. J. *Journal of the American Chemical Society* **2021**, *143*, 3817–3829.

(15) Gehring, P.; Sowa, J. K.; Hsu, C.; de Bruijckere, J.; van der Star, M.; Le Roy, J. J.; Bogani, L.; Gauger, E. M.; van der Zant, H. S. J. *Nature Nanotechnology* **2021**, *16*, 426–430.

(16) Quek, S. Y.; Kamenetska, M.; Steigerwald, M. L.; Choi, H. J.; Louie, S. G.; Hybertsen, M. S.; Neaton, J. B.; Venkataraman, L. *Nature Nanotechnology* **2009**, *4*, 230–234.

(17) Stefani, D.; Weiland, K. J.; Skripnik, M.; Hsu, C.; Perrin, M. L.; Mayor, M.; Pauly, F.; van der Zant, H. S. J. *Nano Letters* **2018**, *18*, 5981–5988.

(18) Aradhya, S. V.; Venkataraman, L. *Nature Nanotechnology* **2013**, *8*, 399–410.

(19) Gehring, P.; Thijssen, J. M.; van der Zant, H. S. J. *Nat. Rev. Phys.* **2019**, *1*, 381–396.

(20) Park, J.; Pasupathy, A. N.; Goldsmith, J. I.; Chang, C.; Yaish, Y.; Petta, J. R.; Rinkoski, M.; Sethna, J. P.; Abruña, H. D.; McEuen, P. L.; Ralph, D. C. *Nature* **2002**, *417*, 722–725.

(21) Arroyo, C. R.; Tarkuc, S.; Frisenda, R.; Seldenthuis, J. S.; Woerde, C. H.; Eelkema, R.; Grozema, F. C.; Van Der Zant, H. S. J. *Angewandte Chemie - International Edition* **2013**, *52*, 3152–3155.

(22) Frisenda, R.; Janssen, V. A. E. C.; Grozema, F. C.; van der Zant, H. S. J.; Renaud, N. *Nature Chemistry* **2016**, *8*, 1099–1104.

(23) Yu, L. H.; Keane, Z. K.; Ciszek, J. W.; Cheng, L.; Stewart, M. P.; Tour, J. M.; Natelson, D. *Physical Review Letters* **2004**, *93*, 266802.

(24) Frisenda, R.; Harzmann, G. D.; Celis Gil, J. A.; Thijssen, J. M.; Mayor, M.; van der Zant, H. S. J. *Nano Letters* **2016**, *16*, 4733–4737.

(25) De Bruijckere, J.; Gehring, P.; Palacios-Corella, M.; Clemente-León, M.; Coronado, E.; Paaske, J.; Hedegård, P.; van der Zant, H. S. J. *Phys. Rev. Lett.* **2019**, *122*, 197701.

(26) Winkelmann, C. B.; Roch, N.; Wernsdorfer, W.; Bouchiat, V.; Balestro, F. *Nature Physics* **2009**, *5*, 876–879.

(27) Island, J. O.; Gaudenzi, R.; de Bruijckere, J.; Burzurí, E.; Franco, C.; Mas-Torrent, M.; Rovira, C.; Veciana, J.; Klapwijk, T. M.; Aguado, R.; van der Zant, H. S. J. *Physical Review Letters* **2017**, *118*, 117001.

(28) Mulliken, R. S. *Nobel Lectures, Chemistry 1963-1970* **1972**.

(29) Li, J.; Shen, P.; Zhen, S.; Tang, C.; Ye, Y.; Zhou, D.; Hong, W.; Zhao, Z.; Tang, B. Z. *Nature Communications* **2021**, *12*, 167.

(30) Reznikova, K.; Hsu, C.; Schosser, W. M.; Gallego, A.; Beltako, K.; Pauly, F.; van der Zant, H. S. J.; Mayor, M. *Journal of the American Chemical Society* **2021**, *143*, 13944–13951.

(31) Schosser, W. M.; Hsu, C.-W.; Zwick, P.; Beltako, K.; Dulić, D.; Mayor, M.; van der Zant, H. S. J.; Pauly, F. *Nanoscale* **2022**, *14*, 984–992.

(32) Pyurbeeva, E.; Hsu, C.; Vogel, D.; Wegeberg, C.; Mayor, M.; van der Zant, H. S. J.; Mol, J. A.; Gehring, P. *Nano Letters* **2021**, *21*, 9715–9719.

(33) Hsu, C.; Costi, T. A.; Vogel, D.; Wegeberg, C.; Mayor, M.; van der Zant, H. S. J.; Gehring, P. *Physical Review Letters* **2022**, *128*, 147701.

(34) Naaman, R.; Waldeck, D. H. *The Journal of Physical Chemistry Letters* **2012**, *3*, 2178–2187.

(35) Göhler, B.; Hamelbeck, V.; Markus, T. Z.; Kettner, M.; Hanne, G. F.; Vager, Z.; Naaman, R.; Zacharias, H. *Science* **2011**, *331*, 894–897.

2

Experimental methods and theoretical background

In this chapter, we focus on two aspects of single-molecule studies, which we use throughout this dissertation: mechanically controlled break junction and thermoelectric eletromigrated break junction. Both devices for single-molecule studies are created with nanofabrication processes, which we describe in detail. We discuss the measurement set-ups and protocols used in the experimental studies of single molecules in these two devices. We also give a short description of the relevant theoretical background of single-molecule junction charge transport and thermoelectricity.

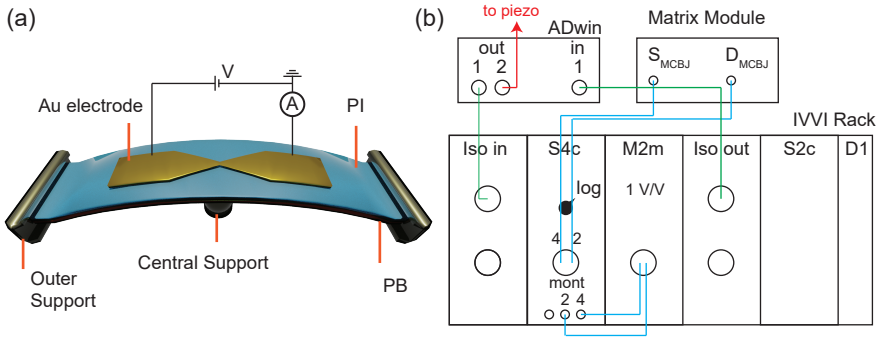

Figure 2.1: (a) MCBJ sample schematic. (b) Measurement set-up for MCBJ measurement. Here, we supply a constant bias voltage *via* the S4c voltage source and measure the corresponding current with a M2m voltmeter after the logarithmic current amplification. The piezoelectric element is continuously bending the substrate during a breaking event, controlled by the ADwin controller. The IVVI rack and Matrix module are homemade electronics for low-noise measurements[1].

2.1. Mechanically controlled break junction

Mechanically controlled break junction (MCBJ) is a versatile technique for single-molecule studies, owing to its high stability and excellent mechanical control. It was first proposed in the 80s as a method to characterize tunneling current at nanoscale [1, 2] and later realized to be an excellent platform for single-molecule studies [3]. It is now a well-established technique for studying quantum effects at the single-molecule level at room temperature [4].

The MCBJ devices we use in this dissertation were developed by C. Martin and the development of the technique is described in detail in Ref. [5–7]. The device structure of a MCBJ is shown in Fig. 2.1a, where a lithographically defined Au electrode is broken by the bending of a flexible Phosphor bronze (PB) substrate. The MCBJ device is fabricated *via* electron beam lithography at the Kavli Nanolab in Delft, and the fabrication steps can be found in Sec. 2.4.1. In short, the process starts by coating a flexible conductive substrate, PB, by an insulating layer of polyimide (PI). The treated substrate is then spin coated with MMA/PMMA double-layer resist and patterned with electron beam lithography. After the deposition of 5/80 nm of Ti/Au electrodes, the bridges of the MCBJ sample are suspended *via* an isotropic reactive ion etching process. Afterwards, the MCBJ sample is firmly clamped onto a MCBJ set-up for reference and single-molecule measurements.

2.1.1. Measurement and experimental set-up

In a typical measurement routine, we use a motor to pre-bend the MCBJ substrate in the set-up; once a junction in the device is broken, we switch to a piezoeletric element to perform the "fast-breaking" measurement. In a fast-breaking measurement, a constant bias voltage of typically 100 mV is applied across the MCBJ, and the associated current is monitored simultaneously. The piezoelectric element continuously pushes the central support of the MCBJ with a lever, and stretches the

suspended gold bridge. During this process of stretching, the gold wire thins down and eventually reaches a conductance value of $G = G_0 = 2e^2/h \approx 7.75 \times 10^{-5}\mathrm{S}$. Here, G_0 is the conductance quantum, e is the electron charge and h is the Planck's constant. This indicates the formation of a single-atom Au contact, which we then rupture to create a nano gap. After the formation of the nano gap, the electrodes continue to displace until reaching the current noise floor and the recorded conductance vs. electrode displacement curve is the so-called "breaking trace".

Generally, prior to the characterization of a molecule of interest, a reference measurement with 3000 breaking traces is performed on a clean gold MCBJ sample. This ensures the quality of the MCBJ sample and also serves as a way to calibrate the electrode separation in the measurement [8]. Afterwards, the molecule of interest is dissolved in an appropriate solvent, typically with a concentration from $1\ \mu\mathrm{M}$ to $1\ \mathrm{mM}$. The single-molecule fast-breaking measurement is then performed after the dropcasting of the molecular solution. When a molecule with decent electron transmission is present and forms a junction with the Au electrodes, a conductance plateau is observed in the conductance vs. electrode displacement curve, with a length associated with the molecular length. We overlay these curves and plot them in two-dimensional (2D) conductance-displacement histograms, which allow us to observe the statistical behavior of a single-molecule junction.

Figure 2.1b shows the electrical connection for the fast-breaking measurement. The IVVI rack and Matrix module are Delft-made electronics for low-noise electrical measurements[1]. Before the measurement, we load a home-made fast-breaking process in the ADwin microprocessor/controller, which allows us to control and monitor the experiment at a high frequency of up to 200 kHz. During the measurement, a constant bias voltage is sent *via* the ADwin to the signal input, Iso-in. This signals the voltage source, S4c, to supply a constant bias voltage to the source electrode, $\mathrm{S}_{\mathrm{MCBJ}}$, with the drain lead, $\mathrm{D}_{\mathrm{MCBJ}}$, grounded. The corresponding current is monitored with a logarithmic amplifier in the S4c module, which allows us to measure the large dynamical range (conductance change up to 10 orders of magnitude) of a breaking trace. The voltmeter, M2m, then measures the output of the logarithmic amplifier and sends the signal back *via* the Iso-out to the ADwin, which is connected to the computer.

2.2. Electromigrated break junction for thermoelectric measurement

Electromigration (EM) is a common process in an electrical circuit where ions inside a material move as a result of a strong electrical field. In the case of electrical interconnects, this is an unwanted process because it essentially causes electrical failure in electronics. However, with a proper design, it is possible to exploit this process to create a nano gap by EM [9]; the size of nano gaps can also be electrically controlled by means of computer-controlled feedback loops [10]. This is an especially attractive method for contacting subjects with sizes of a few nanometers, for example, molecules [11]. Such a method for contacting single molecules is the

[1]The details of the electronics can be found at QT work: https://qtwork.tudelft.nl/

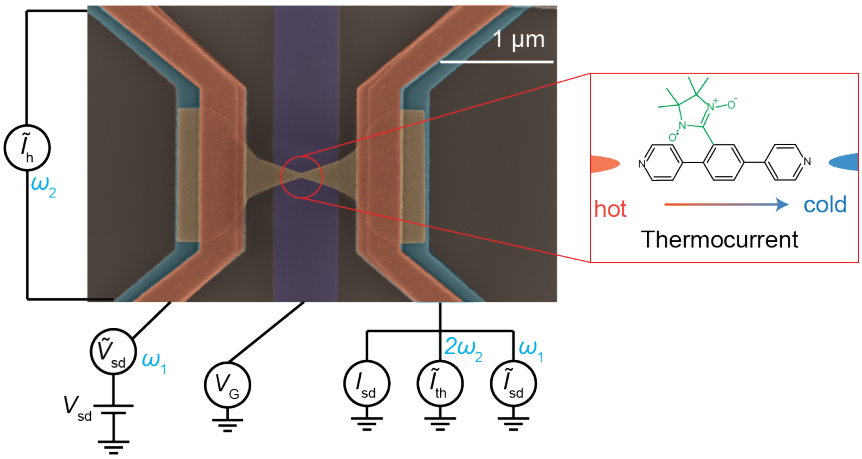

Figure 2.2: Electrical connections of Th-EMBJ. At the center of the sample, the EMBJ is opened and a molecule of interest is deposited. A NNR molecule, studied in Chap. 6, is used as an example for the Th-EMBJ device.

so-called electromigrated break junction (EMBJ), which is now commonly used to form stable single-molecule junctions [12].

The electromigrated break junction thermoelectric device (Th-EMBJ) is an extension of the EMBJ for the possibility to detect thermoelectric signals in molecules. Th-EMBJ was first developed by P. Gehring and M. van der Star, and the detailed development of the device can be found in Ref. [13, 14]. The device structure is shown in Fig. 2.2, where a pair of heaters are included right below the EMBJ with an electrical insulation. The Th-EMBJ device is fabricated by standard electron-beam lithography with double-layer PMMA 495K/950K resists, followed by electron-beam evaporation deposition. In short, the local back gate (purple) with Ti/Pd thicknesses of 1/7 nm is patterned on a SiO_2/Si substrate with an oxide thickness of 817 nm. The heaters (light blue) are made with Ti/Pd with thicknesses of 3/27 nm. Afterwards, a 10-nm Al_2O_3 gate-oxide layer is deposited *via* atomic layer deposition at 300°C. The Au bridge (gold) is fabricated with a thickness of 15 nm without an adhesive layer. Finally the contact pads (orange pattern) of Ti/Au with thicknesses of 5/65 nm are made to connect the Au bridge made in the previous step. The full fabrication steps can be found in App. 2.4.1.

2.2.1. Measurement and experimental set-up

To perform a thermoelectric measurement in a single-molecule junction, electromigration of the EMBJs is first performed in a vacuum dipstick. The EM technique we use is controlled by a feedback loop with a microprocessor/controller (ADwin) with a homemade software. Essentially, we start the EM by sending a bias voltage in the range of a few hundred mV and simultaneously monitoring the current across the EMBJ. We then slowly ramp up the voltage to a value close to 1 V, where an

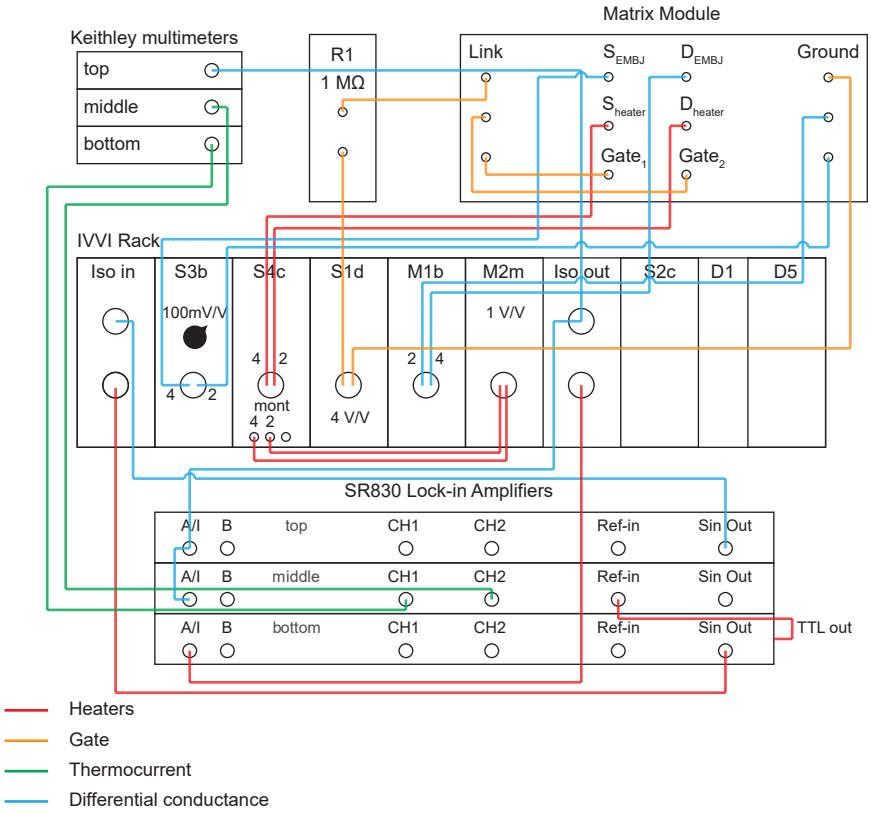

Figure 2.3: Measurement set-up for thermoelectric study of single molecules. Here, we perform the simultaneous characterization of differential conductance and thermocurrent with a dual lock-in technique. The differential conductance measurement is performed by the top lock-in amplifier at frequency of 13 Hz and thermocurrent measurement is sourced by a heater current from the bottom lock-in at a frequency of 3 Hz. The IVVI rack and matrix module are the homemade electronics for low-noise measurement.

increasing of junction resistance is observed as a result of EM. With the feedback control to avoid sudden changes in junction conductance, the junction slowly opens up and eventually reaches a conductance value around $G = G_0$, indicating a single-atom contact. The EMBJ is then left alone for a self-breaking process, which creates a nano gap for contacting molecules [15].

The electromigration is immediately followed by the dropcasting of a molecular solution of interest, and vacuum pumping. Afterwards, the dipstick is loaded into a Helium cooled superconducting magnet set-up. The cryogenic temperature is beneficial for the single-molecule junction stability and reduces the thermal broadening of the Fermi-Dirac distribution in energy. After device formation and cool down, the electrical and thermoelectric measurements are carried out. In order to measure the electrical and thermoelectric signals simultaneously, we employ a lock-in technique,

where the AC thermal bias $\Delta\tilde{T}$ and electrical bias $\tilde{V}_{\mathrm{sd}}$ are applied at two different frequencies. The differential conductance ($\mathrm{d}I/\mathrm{d}V_{\mathrm{sd}}$) of the single-molecule junction is directly obtained with a lock-in amplifier. In a typical experiment $\tilde{V}_{\mathrm{sd}} = 100$ μV at $\omega_1 = 13$ Hz is used. A thermal bias at a frequency $\omega_2 = 3$ Hz is applied by the heater and the resulting thermocurrent (I_{th}) through the molecule is measured at the second harmonic $2\omega_2$ with respect to the excitation. The factor of 2 in the detection frequency of thermocurrent directly comes from the assumption of Joule heating: $P = I^2R \propto \sin^2(\omega_2) \propto -\cos(2\omega_2)$, where P, I and R are the power, current and resistance of the heater.

Figure 2.3 shows the complete measurement set-up for the thermoelectric measurement. Essentially, there are two main electrical pathways of the measurement set-up, which are referred to as differential conductance and heaters in Fig. 2.3. In the case of differential conductance, the bias voltage is sourced with the top lock-in amplifier through Iso-in, together with a DC voltage sourced internally with the D5 module. The combined AC+DC bias voltage is sent with a ten-times voltage divider, S3b, to the source electrode $\mathrm{S}_{\mathrm{EMBJ}}$. The resulted signal is read out at the drain electrode $\mathrm{D}_{\mathrm{EMBJ}}$ by an nano-ammeter, M1b, whose signal is sent by Iso-out to the top and middle lock-in amplifiers for differential conductance and thermocurrent measurement and to the top Keithley for DC current measurement. In the case of heaters, the heater current is sent by the bottom lock-in amplifier through the Iso-in. The heater current is supplied by the current source, S4c, across the heater source and drain electrodes, $\mathrm{S}_{\mathrm{heater}}$ and $\mathrm{D}_{\mathrm{heater}}$. The voltage drop across the heater is also monitored in S4c and measured by a voltmeter, M2m. This voltage is sent back to the bottom lock-in amplifier for the exact heater resistance. Importantly, the thermocurrent, excited by the heater current, is mixed with the AC+DC electrical current in the same $\mathrm{S}_{\mathrm{EMBJ}}$-$\mathrm{D}_{\mathrm{EMBJ}}$ electrodes. Therefore, we separate these three signals by monitoring them at different frequencies with lock-in amplifiers.

2.3. Charge transport in single molecules

2.3.1. Landauer formula

In macroscopic solid state systems, charge transport can be captured by the simple Ohm's law. However, this transport relation becomes invalid when we shrink the size of the system down to the nanoscale. Single molecules are nanostructures and quantum mechanics is needed to describe the behavior of the electrons in these systems. At first sight it seems to be a hopeless problem to solve, because it suggests that we need to consider the microscopic geometry of the system and all the particles involved in the charge transport. However, it turns out that it is possible to describe the charge transport properties in a complex nanostructure in terms of a small set of transmission functions, provided that the scattering in the system is elastic and phase-coherent [16]. This scattering relationship is essentially summarized by the famous Landauer formula [17]:

$$G(E) = G_0 \sum_n T_n(E), \tag{2.1}$$

where the summation is over all the conduction channels n, $G_0 = 2e^2/h$ is the conductance quantum and $T_n(E)$ are the transmission functions of the channels. This scattering relation can be written in a different form in terms of physical parameters which is relevant to an electrical measurement [18, 19]:

$$I(V) = G_0/e \int_{-\infty}^{\infty} dE[f_s(E) - f_d(E)]\tau(E), \tag{2.2}$$

where $\tau(E)$is the energy-dependent transmission function, $f_s(E) = (e^{(E-\mu_s)/k_BT} + 1)^{-1}$ and $f_d(E) = (e^{(E-\mu_d)/k_BT} + 1)^{-1}$ are the Fermi-Dirac distributions of the source (s) and drain (d) electrodes, with the chemical potentials defined as:

$$\begin{aligned} \mu_s &= E_F + eV/2, \\ \mu_d &= E_F - eV/2. \end{aligned} \tag{2.3}$$

In the simplest case of a single-level model, $\tau(E)$ takes the form of a Lorentzian peak following the Breit-Wigner formula for generic resonances, $\frac{4\Gamma_s\Gamma_d}{(E-E_0)^2+(\Gamma_s+\Gamma_d)^2}$ [19]. Here, Γ_s and Γ_d are the electronic coupling strengths between the source and drain electrodes to the molecular level. In the limit of $k_BT \ll eV$, the single-level model yields the following expression for the current across the junction [19]:

$$\begin{aligned} I =& \frac{2e}{h}\frac{4\Gamma_s\Gamma_d}{\Gamma} \\ &\times \left[\arctan\left(\frac{eV/2 - E_0}{\Gamma}\right) + \arctan\left(\frac{eV/2 + E_0}{\Gamma}\right)\right], \end{aligned} \tag{2.4}$$

where $\Gamma = \Gamma_s + \Gamma_d$. However, this single-level model is not sufficient for the single-molecule study we performed in this dissertation. Generally, the function $\tau(E)$ is difficult to find and it requires the precise understanding of the molecular orbital, for example, through a combined density functional theory - nonequilibrium Green's function (DFT-NEGF) calculation [20].

2.3.2. Weak-coupling regime

In the weak-coupling regime, the physics of the single-molecule systems can be described by the theory of Coulomb blockade [16, 21], where the electron-electron interactions dominate. In this regime, the molecular orbitals in a single-molecule junction are well separated in energy and can be treated as discrete energy levels. We call this the quantum dot limit. In a three-terminal junction geometry, the electrostatic energy for the N electrons can be written as:

$$U(N) = E_cN^2 - eNV_{ext} + \sum_{n=1}^{N} E_n, \tag{2.5}$$

where $E_c = e^2/2C$ is the charging energy; $C = C_s + C_d + C_G$ is the total capacitance of the quantum dot, with the capacitive contributions from the source, drain and

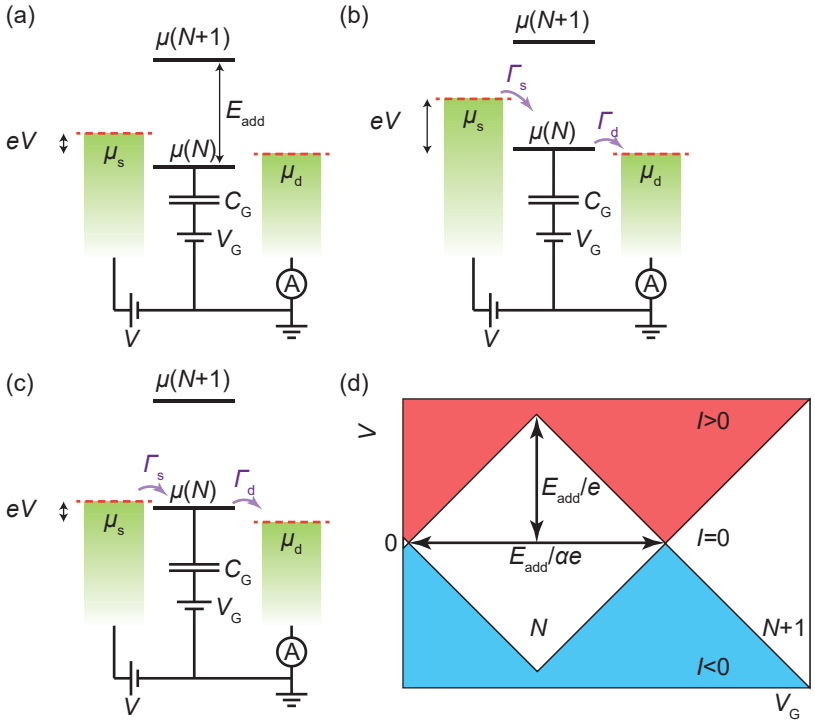

Figure 2.4: (a)-(c) Diagrams of chemical potential and molecular levels. (a) Off-resonance (Blockade). (b) Resonant transport, induced by high bias voltage. (c) Resonant transport, induced by gate-tuned molecular levels. (d) Coulomb stability diagram. The picture here is for a symmetrically coupled quantum dot with $C_d = C_s$.

gate electrodes. V_{ext} is the external electric potential, taking the form: $V_{\text{ext}} = (C_s V_s + C_d V_d + C_G V_G)/C$. E_n are the single-particle energy levels which correspond to the states of n electrons, similar to the concept of molecular orbitals in an isolated molecule. Summing the Coulomb interactions between all pairs of electrons at occupied levels gives the total electrostatic energy of the quantum dot. However, when we want to calculate the current through the quantum dot or molecule in contact with electrodes, we need to consider the energy required to add an extra electron into the dot. This energy is by definition the chemical potential, written as:

$$\begin{aligned} \mu(N) &= U(N) - U(N-1) \\ &= (N - \frac{1}{2})\frac{e^2}{C} - eV_{\text{ext}} + E_N, \end{aligned} \tag{2.6}$$

where E_N is the quantum energy of the N^{th} electron level discarding Coulomb interactions. Similarly, the chemical potential for $N+1$ electrons in the dot can be obtained in the same fashion. We can then calculate the chemical potential differ-

ence between $N+1$ and N states, which is called the "addition energy":

$$\begin{aligned} E_{\text{add}} &= \mu(N+1) - \mu(N) \\ &= E_{N+1} - E_N + \frac{e^2}{C}. \end{aligned} \tag{2.7}$$

E_{add} basically tells us how far two electronic levels are separated in a quantum dot junction.

The relevant levels discussed above are summarized in Fig. 2.4a. Figures 2.4a-c provide an intuitive way to see if charge transport is possible in the quantum dot. In the most basic picture, without considering higher-order processes, charge transport is inhibited in the case of Fig. 2.4a, where $\mu(N)$ does not lie between μ_{s} and μ_{d}. The absence of states within the bias window indicates a blockade of charge transport, which is also referred to as "Coulomb blockade". It is only possible for a charge to sequentially tunnel through the quantum dot when a level lies within the bias window. This is shown in the cases of Figs. 2.4b and c, where the level $\mu(N)$ is brought into the bias window either by a higher applied external voltage or by the electric field from the gate.

By measuring the current across the quantum dot as functions of V and V_{G}, the "Coulomb stability diagram" can be obtained, as shown in Fig. 2.4d. Here, we can see that the current is inhibited in the white-colored region of the Coulomb blockade. In the vertical direction, we can directly obtain E_{add} between N to $N+1$ states, by the taking the vertical distance between the two vertices of the Coulomb blockade above and below the zero-bias axis; in the horizontal direction, we can also obtain E_{add}/α for N to $N+1$, where $\alpha = C_{\text{G}}/C$ is the gate coupling. The Coulomb stability diagram provides a spectroscopic tool for single-charge transport in quantum dots.

2.3.3. Thermoelectric effect in single molecules

Thermoelectricity is the coupling between thermal and electric transport. In macroscopic systems in the linear regime, the electrical-temperature relation can be written as:

$$\begin{aligned} I_{\text{electric}} &= VG - L\Delta T, \\ I_{\text{heat}} &= \Pi I_{\text{electric}} - (\kappa_e + \kappa_p)\Delta T, \end{aligned} \tag{2.8}$$

where, $L = GS$ is the thermal response coefficient, G is (as usual) the conductance, S is the so-called Seebeck coefficient, ΔT is the temperature difference between the two electrodes, Π is the Peltier coefficient and κ_e and κ_p are the thermal conductivity from electronic and phononic contributions. These parameters are particularly interesting material properties for thermoelectric device applications. Fundamentally, it is also interesting to study these quantities in charge transport at the nanoscale. A simple single-particle thermopower formalism in the linear response regime for charge transport can be obtained by introducing a temperature difference into the Landauer formula in Eq. 2.2 [22–25]. Essentially, this temperature difference is captured in the difference of the Fermi-Dirac distributions between the source and

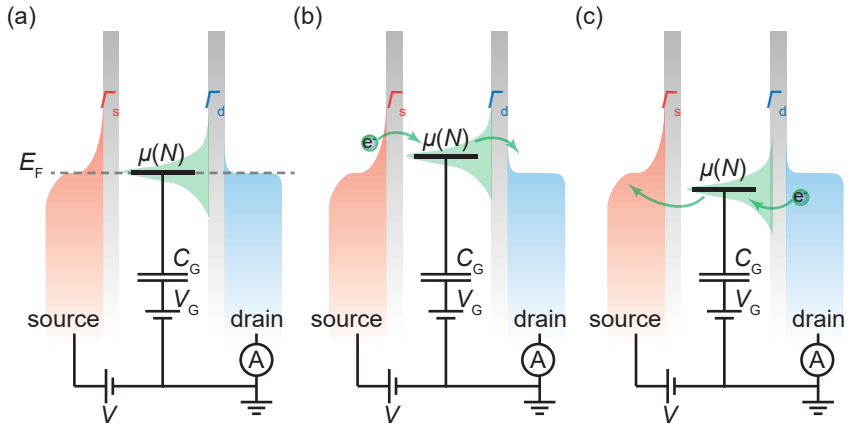

Figure 2.5: Diagrams of Fermi energy and molecular levels with the source electrode at a higher temperature. The green-shaded Lorentzian distribution represents the transmission function of the level. For non-zero L, the derivative of the transmission function at Fermi energy, $\tau'(E_F)$, needs to be non-zero. By taking the slope of the Lorentzian transmission function, $\tau'(E_F)$ is zero in the case of (a), positive for the case of (b) and negative for the case of (c), giving zero, positive and negative L, respectively.

drain electrodes, which we can expand for small bias and temperature difference:

$$f_s(E) - f_d(E) = -\frac{\partial f}{\partial E}\Delta\mu - \frac{\partial f}{\partial E}\left(\frac{E - E_F}{T}\right)\Delta T, \tag{2.9}$$

where $\Delta\mu = \mu_s - \mu_d = e\Delta V$. By introducing Eq. 2.9 into the full integral of Eq. 2.2, there are two main components which contribute to the current $I_{electric}$, written as:

$$I_{electric} = G\Delta V + L\Delta T \tag{2.10}$$

where, G and L are the previously mentioned conductance and thermal response coefficient [25]:

$$G = \frac{2e^2}{h}\int_0^\infty dE\tau(E)\left(-\frac{\partial f}{\partial E}\right), \tag{2.11}$$

$$L = GS = \frac{2e}{h}\frac{1}{T}\int_0^\infty dE\tau(E)(E - E_F)\left(-\frac{\partial f}{\partial E}\right). \tag{2.12}$$

Interestingly, this recovers the relation as shown in Eq. 2.8, but now with integral expressions for the coefficients G and S.

An important observation from this formalism is that it is possible to create a current solely due to a temperature difference across the electrodes, which we refer to as "thermocurrent", I_{th}. This generation of thermocurrent is best illustrated in Fig. 2.5, where we show the diagrams of the Fermi-Dirac distributions and energy levels with the absence of bias voltage. In the simplest case in Fig. 2.5a, the chemical potential of the molecule is aligned with the Fermi energy of the electrodes

($E = E_F$), resulting $L = 0$, as shown in Eq. 2.12. This means that there is no current or thermocurrent across electrodes, suggested by Eq. 2.10. In the case of Fig. 2.5b, the chemical potential of the molecule is slightly higher than the Fermi energy, which leads to a thermocurrent where electrons are moving to the right, in a typical case of Lorentzian transmission function in the level. This thermocurrent can be seen from Eq. 2.12. Intuitively, the hot electrode has a more broadened Fermi-Dirac distribution, which allows electrons to populate higher energy states, leading to the possibility to sequentially tunnel from the left electrode to the molecule, and to the right electrode. The opposite process happens when the chemical potential of the molecule is slightly lower than the Fermi energy of the electrodes, as shown in Fig. 2.5c. In this case, the hot electrode has empty states available for the electron to sequentially tunnel from the right electrode to the molecule, and then to the left electrode.

It is possible to approximate G, L and S in Eq. 2.11 and 2.12, by means of the Sommerfeld expansion at low temperature. This gives [25]:

$$G = G_0 \tau(E_F), \tag{2.13}$$

$$L(T) = G_0 \frac{\pi^2}{3} \frac{k_B^2 T}{e} \tau'(E_F), \tag{2.14}$$

$$S(T) = \frac{\pi^2}{3} \frac{k_B^2 T}{e} \frac{\tau'(E_F)}{\tau(E_F)}. \tag{2.15}$$

Eqs. 2.14 and 2.15 show that the thermal response and thermopower depend on the derivative of the transmission function of the molecule, close to the Fermi energy. For a high-performance thermoelectric molecular junction or nanostructure, it is thus favorable to have a sharp transmission function at the Fermi energy for device applications.

2.4. Appendix

2.4.1. Fabrication procedures

Here, we provide the fabrication steps for the MCBJ and Th-EMBJ devices discussed in this chapter.

MCBJ

We use standard electron-beam lithography processes to fabricate the MCBJ devices on flexible substrates. The fabrication steps are described below.

- Substrate preparation

1. Hot acetone cleaning of a phosphor bronze substrate at 50°C for 10 min, followed by the rinsing with isopropanol (IPA) for 2 min.
2. Hot-plate baking at 110°C for 1 min.
3. Spin coating of 0.1 vol% of VM651 adhesion promoter in IPA at 3000 rpm, followed by a hot-plate baking at 110°C for 1 min.
4. Spin coating of polyimide, PI2610, at 800 rpm.

5. Vacuum oven baking at 300°C for 30 min.

■ MCBJ structure

6. Spin coating MMA(8.5) in 8% ethyl lactate at 3000 rpm and PMMA 950K A4 at 6000 rpm, both followed by a hot-plate baking at 190°C for 7 min each.
7. Electron beam patterning for MCBJ structure with doses of 1200 $\mu C/cm^2$ for the fine structure and 1050 $\mu C/cm^2$ for the coarse structure at an acceleration voltage of 100 keV.
8. Development in MIBK:IPA with 1:3 ratio for 90 s and stopping in IPA for 30 s.
9. Electron beam evaporation of Ti/Au with thicknesses of 5/80 nm, followed by lift-off in hot acetone at 50°C.

■ Cutting and RIE etching

10. Spin coating a protective layer of PMMA 950K A2 at 1500 rpm, followed by a hot-plate baking at 190°C for 3 min.
11. Cutting the substrate into 10 samples with a bench-top metal shear or laser cutter.
12. Cleaning in hot acetone at 50°C for 10 min, followed by IPA rinsing for 2 min.
13. Reactive ion etching (RIE) with oxygen for 32 min. RF power = 30 W, pressure = 200 μbar, flow rate = 50 sccm, bias voltage= -75 V.

Th-EMBJ

The Th-EMBJ devices also employs standard electron-beam lithography processes. Here, we provide the recipe we used for the fabrication and suggestions for future improvements.

1. Hot acetone cleaning for a SiO_2/Si (oxide thickness of 817 nm) at 50°C for 10 min, followed by rinsing in IPA for 2 min.
2. Oxygen plasma cleaning (TEPLA) at 600 W with a flow rate of 200 sccm for 5 min.

■ Alignment markers

3. Spin coating MMA(8.5) in 8% ethyl lactate at 6000 rpm with hot-plate baking at 190°C for 3 min.
4. Spin coating PMMA 950K A2 at 3000 rpm with hot-plate baking at 190°C for 3 min.
5. Electron beam patterning for markers with a dose of 1200 $\mu C/cm^2$ at an acceleration voltage of 100 keV.
6. Development in MIBK:IPA with 1:3 ratio for 90 s and stopping in IPA for 30 s.
7. Electron beam evaporation of Ti/Au with thicknesses of 5/55 nm, followed by lift-off in hot acetone at 50°C.

■ Local back gate

8. Oxygen plasma cleaning (TEPLA) at 300 W with a flow rate of 200 sccm for 5 min.
9. Spin coating MMA(8.5) in 8% ethyl lactate at 6000 rpm with hot-plate baking at 190°C for 3 min.
10. Spin coating PMMA 950K A2 at 3000 rpm with hot-plate baking at 190°C for 3 min.

11. Electron beam patterning for the back back gate with a dose of 1560 $\mu C/cm^2$ at an acceleration voltage of 100 keV.
12. Development in MIBK:IPA with 1:3 ratio for 90 s and stopping in IPA for 30 s.
13. Electron beam evaporation of Ti/Pd with thicknesses of 1/7 nm, followed by lift-off in hot NMP (N-Methyl-2-pyrrolidone) at 80°C and cleaning acetone and IPA.

- Heaters

14. Oxygen plasma cleaning (TEPLA) at 300 W with a flow rate of 200 sccm for 5 min.
15. Spin coating MMA(8.5) in 8% ethyl lactate at 6000 rpm with hot-plate baking at 190°C for 3 min.
16. Spin coating PMMA 950K A2 at 3000 rpm with hot-plate baking at 190°C for 3 min.
17. Electron beam patterning for the back back gate with a dose of 1560 $\mu C/cm^2$ at an acceleration voltage of 100 keV.
18. Development in MIBK:IPA with 1:3 ratio for 90 s and stopping in IPA for 30 s.
19. Electron beam evaporation of Ti/Pd with thicknesses of 3/27 nm, followed by lift-off in hot NMP at 80°C and cleaning acetone and IPA.

- ALD of Aluminum gate oxide

20. Oxygen plasma cleaning (TEPLA) at 300 W with a flow rate of 200 sccm for 5 min.
21. Atomic layer deposition (ALD) (Oxford Instrument) of 10 nm Aluminum oxide at 300°C.

- EMBJ structure

22. Oxygen plasma cleaning (TEPLA) at 300 W with a flow rate of 200 sccm for 5 min.
23. Spin coating MMA(8.5) in 8% ethyl lactate at 6000 rpm with hot-plate baking at 190°C for 3 min.
24. Spin coating PMMA 950K A2 at 3000 rpm with hot-plate baking at 190°C for 3 min.
25. Electron beam patterning for EMBJ constriction with a dose of 1560 $\mu C/cm^2$ at an acceleration voltage of 100 keV.
26. Development in MIBK:IPA with 1:3 ratio for 90 s and stopping in IPA for 30 s.
27. Electron beam evaporation of Au with a thickness of 15 nm, followed by lift-off in hot acetone at 50°C.

- Contact pads

28. Spin coating MMA(8.5) in 8% ethyl lactate at 6000 rpm with hot-plate baking at 190°C for 3 min.
29. Spin coating PMMA 950K A2 at 3000 rpm with hot-plate baking at 190°C for 3 min.
30. Electron beam patterning for EMBJ constriction with a dose of 1560 $\mu C/cm^2$ at an acceleration voltage of 100 keV.
31. Development in MIBK:IPA with 1:3 ratio for 90 s and stopping in IPA for 30 s.
32. Electron beam evaporation of Au with a thickness of 15 nm, followed by lift-off in hot acetone at 50°C.

We have also proposed an improvement for the recipe of Th-EMBJ by combining the first three steps of alignment markers, local back gate and heaters in the same lithographic step. This is done by embedding the three structures with RIE, so that the height of the patterns is the same as that of the SiO_2 substrate. The proposed first three steps, right before ALD, can be combined as the following:

1. Hot acetone cleaning for a SiO_2/Si (oxide thickness of 817 nm) at 50°C for 10 min, followed by rinsing in IPA for 2 min.

2. Oxygen plasma cleaning (TEPLA) at 600 W with a flow rate of 200 sccm for 5 min.

■ Alignment markers, local back gate and heaters

3. Spin coating PMMA 495K A6 at 3000 rpm with hot-plate baking at 190° for 3 min. This gives a resist thickness of about 350 nm.

4. Spin coating PMMA 950K A8 at 3000 rpm with hot-plate baking at 190° for 15 min. This gives a resist thickness of about 600 nm.

Note: The choice of the thick resist layer is for the reactive ion etching (RIE) step performed later.

5. Electron beam patterning for all the structures with a dose of 1560 $\mu C/cm^2$ at an acceleration voltage of 100 keV.

Note: Importantly, to prevent drift between different electron beams, all the three patterns have to be written by the same electron beam.

6. Development in MIBK:IPA with 1:3 ratio for 90 s and stopping in IPA for 30 s.

7. RIE etching (Sentech) for 6 min: RF power =50 W, P =100 μbar CHF_3=25 sccm, Ar 25 sccm. Typical bias voltage is around -200 V. This gives an etched depth of 50 nm. (The exact depth needs to be measured by ellipsometry.)

8. Electron beam evaporation of Ti/Pt with thicknesses of 3/52 nm, followed by lift-off in hot acetone at 50°C.

Note: For better smoothness, it is possible to use Pd instead of Pt in the evaporation. However, in this case, the etching time should be around 10 minutes, for a trench of around 85 nm. The Pd thickness should be increased to around 82 nm. This larger thickness of Pd is necessary for a good contrast for marker alignment.

References

(1) Moreland, J.; Ekin, J. W. *Journal of Applied Physics* **1985**, *58*, 3888–3895.

(2) Muller, C. J.; van Ruitenbeek, J. M.; de Jongh, L. J. *Physica C: Superconductivity and its applications* **1992**, *191*, 485–504.

(3) Reed, M. A.; Zhou, C.; Muller, C. J.; Burgin, T. P.; Tour, J. M. *Science* **1997**, *278*, 252–254.

(4) Agraït, N.; Yeyati, A. L.; van Ruitenbeek, J. M. *Physics Reports* **2003**, *377*, 81–279.

(5) Martin, C. A.; Smit, R. H. M.; Egmond, R. V.; van der Zant, H. S. J.; van Ruitenbeek, J. M. *Review of Scientific Instruments* **2011**, *82*, 053907.

(6) Martin, C. A.; Ding, D.; van der Zant, H. S. J.; van Ruitenbeek, J. M. *New Journal of Physics* **2008**, *10*, 065008.

(7) Martin, C. A. *Ph.D. thesis, TU Delft* **2011**.

(8) Untiedt, C.; Yanson, A. I.; Grande, R.; Rubio-Bollinger, G.; Agraït, N.; Vieira, S.; van Ruitenbeek, J. M. *Physical Review B - Condensed Matter and Materials Physics* **2002**, *66*, 854181–854186.

(9) Park, H.; Lim, A. K.; Alivisatos, A. P.; Park, J.; McEuen, P. L. *Applied Physics Letters* **1999**, *75*, 301–303.

(10) Campbell, J. M.; Knobel, R. G. *Applied Physics Letters* **2013**, *102*, 1–5.

(11) Van Der Zant, H. S. J.; Osorio, E. A.; Poot, M.; O'Neill, K. *Physica Status Solidi (B) Basic Research* **2006**, *243*, 3408–3412.

(12) Hoffmann-Vogel, R. *Applied Physics Reviews* **2017**, *4*, 031302.

(13) Gehring, P.; van der Star, M.; Evangeli, C.; Le Roy, J. J.; Bogani, L.; Kolosov, O. V.; van der Zant, H. S. J. *Appl. Phys. Lett.* **2019**, *115*, 073103.

(14) Van der Star, M. *Master thesis, TU Delft* **2019**.

(15) O'Neill, K.; Osorio, E. A.; van der Zant, H. S. J. *Applied Physics Letters* **2007**, *90*, 2005–2008.

(16) Nazarov, Y. V.; Blanter, Y. M., *Quantum Transport*; Cambridge University Press: Cambridge, 2009.

(17) Landauer, R. *IBM Journal of Research and Development* **1957**, *1*, 223–231.

(18) Cuevas, J. C.; Heurich, J.; Pauly, F.; Wenzel, W.; Sch n, G. *Nanotechnology* **2003**, *14*, R29–R38.

(19) Cuevas, J. C.; Scheer, E., *Molecular Electronics: An Introduction to Theory and Experiment*, 2nd Edition; World Scientific: Singapore, 2017.

(20) Pauly, F.; Viljas, J. K.; Huniar, U.; Häfner, M.; Wohlthat, S.; Bürkle, M.; Cuevas, J. C.; Schön, G. *New Journal of Physics* **2008**, *10*, 125019.

(21) Thijssen, J. M.; Van der Zant, H. S. J. *physica status solidi (b)* **2008**, *245*, 1455–1470.

(22) Bergfield, J. P.; Stafford, C. A. *Nano Letters* **2009**, *9*, 3072–3076.

(23) Finch, C. M.; García-Suárez, V. M.; Lambert, C. J. *Physical Review B - Condensed Matter and Materials Physics* **2009**, *79*, 2–5.

(24) Lunde, A. M.; Flensberg, K. *Journal of Physics: Condensed Matter* **2005**, *17*, 3879–3884.

(25) Rincón-García, L.; Evangeli, C.; Rubio-Bollinger, G.; Agraït, N. *Chemical Society Reviews* **2016**, *45*, 4285–4306.

3

Mechanosensitivity in single molecules: Destructive quantum interference

Quantum interference (QI) of electron waves is a ubiquitous phenomenon in electronic transport in single-molecule junctions. Thanks to the recent advancement in the single-molecule studies, it is now an essential ingredient to integrate for designs of molecular electronics. Here, we show how small structural changes in a single-molecule junction can introduce great effects in its electronic transmission. Such QI-origin mechanosensitivity is manifested in the paracyclophane and cofacial porphyrin molecules, studied in mechanically controlled break junctions. QI of molecules not only gives the fundamental insight into quantum transport at the single-molecule level but also suggests potential molecule-based electro-mechanical sensor applications.

Parts of this chapter have been published in *Journal of the American Chemical Society* **2021**, *143*, 13944–13951 [1] and *Nanoscale* **2022**, *14*, 984–992 [2].

3.1. Introduction

In recent years, great advancements have been made in the field of molecular electronics toward single-molecule junction studies [3]. The visionary idea of Aviram and Ratner [4] to profit from single molecules as functional units in electronic devices led to the development of several proof-of-concept molecular devices, such as molecular wires [5, 6], switches [7, 8], rectifiers/diodes [9, 10], and thermoelectronic devices [11, 12]. The design of molecules incorporated in such electrode-molecule-electrode junctions is guided by our understanding of charge transport through the molecules. Indeed, even small structural modifications such as substituent effects [13, 14], conformational flexibility [15], and changes in the anchoring groups and their positions [16–20] can result in large conductance variations. Particularly strong variations are predicted for quantum interference (QI) effects originating from the interplay between different transport pathways. Destructive QI (DQI) or constructive QI (CQI) between the pathways can occur, reflected in a low or high conductance, respectively [21]. QI effects thus become essential molecular design elements, on the one hand enriching the variety of functionalities emerging from the molecular structure but on the other hand making a full comprehension of the molecule's electronic transport behavior more challenging. A detailed understanding of these QI effects and of their origin in the molecule's structure is thus crucial to realize their full potential in future electronic components and devices.

In this chapter, we discuss two single-molecule systems: [2.2]paracyclophane and cofacial porphyrin cyclphane. Both of these systems are three dimensional entities with large π-orbital overlaps within their double-decker structures. We study the changes in their orbital overlaps induced by mechanical deformation, which gives rise to QI effects that depend on the symmetry in the molecular structures. These works provide deeper insight into QI effects in complex molecular structures and show the potential molecular devices as nanoscale mechanical sensors.

3.2. [2.2]Paracyclophane

Relationships between substitution pattern and single-molecule conductance were already theoretically predicted and experimentally confirmed in a variety of examples, ranging from simple phenyl rings [22] connected directly to the electrodes to more sophisticated oligo(phenylene vinylene) (OPV) [23] and oligo(phenylene ethynylene) (OPE)-based molecular wires [17]. Unanimously, these studies report a decrease in electronic transparency upon shifting the anchoring groups from the *para* to the *meta* position. This observation was rationalized by Yoshizawa and co-workers [24–26], who considered frontier orbital theory for simple organic molecules. Their set of rules predicts for benzene the *para* connection to be the symmetry-allowed one for charge transport, while charge transport involving the *meta* connection is symmetry-forbidden, resulting in high and low conductance, respectively.

Because the effects of substitution patterns in planar π-systems are well described and understood, our focus moved to three-dimensional structures like [2.2]-

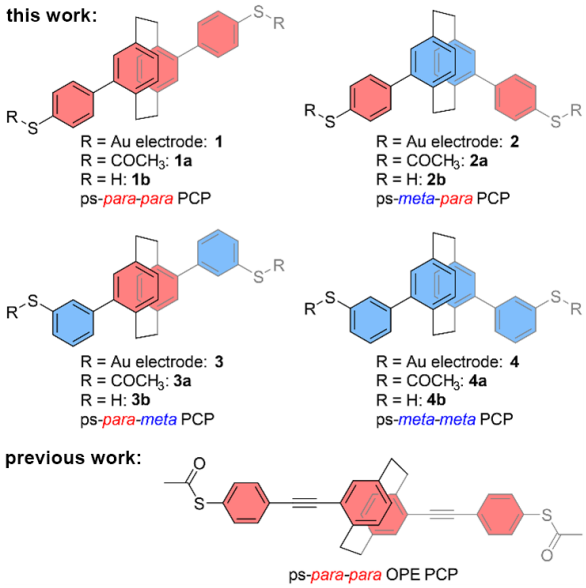

Figure 3.1: Schematic representation of target structures **1-4** together with the already reported model compound. The four molecules include either *para* or *meta* connection patterns in both the central PCP subunit and the peripheral phenyl subunits labeled in red and blue, respectively. For simplicity, the following text refers to the structures by their prefixes, with ps as an abbreviation for pseudo, followed by the prefix referring to the substitution pattern of the central PCP, and finally the prefix referring to the substitution pattern of the thiol anchor group in the phenyl subunits.

paracyclophane (PCP), with two benzene systems facing each other interlinked by a pair of C_2H_4 bridges [27]. Initially, we considered the structure as a model to investigate the through-space coupling of the stacked π-systems [28, 29] but realized quickly that their behavior is much richer. Already the first model compound [30] (ps-*para*-*para*-OPE PCP in Fig. 3.1) displayed a sharp destructive QI feature close to the Fermi level, but the phenomenon also depends substantially on the mechanical stress exposed to the molecule. It thus seemed that the rigid but squeezable PCP subunit provided mechanosensitivity to the molecular junction. Interestingly, Yoshizawa and co-workers [31] already provided their orbital view of PCP subunits and predicted that charge transport through the pseudo-*para*-substituted PCP should be suppressed due to DQI, while CQI would prevail for pseudo-*meta*-substituted PCP. It thus seems that the rule-of-thumb (*para* → good transport due to CQI; *meta* → bad transport due to DQI) is inverted for the PCP subunit.

Excited by this hypothesis, we explored the effects of the substitution pattern in more detail and designed the four PCP model compounds **1–4** (see Fig. 3.1) consisting of comparable subunits but with various substitution patterns. The oligo-(phenylene)-type PCP structures combine the compactness favoring electronic transparency on a detectable level with straightforward synthetic accessibility. Terminal acetyl masked thiol anchor groups enable their immobilization in a mechanically

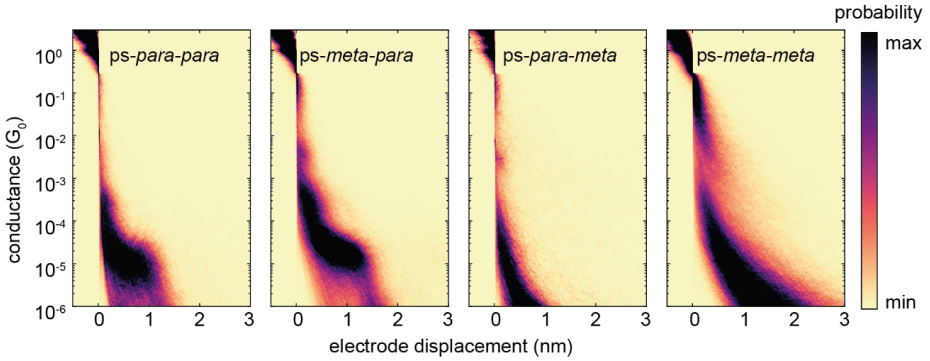

Figure 3.2: Two-dimensional conductance vs electrode displacement density histograms. The first (from the left) and second histograms are built up from 6834 and 9638 traces at 100 mV with ps-*para*-*para*- and ps-*meta*-*para*-PCP molecules, respectively. The third and fourth 2D histograms correspond to 3780 and 10000 traces at a bias voltage at 250 mV with ps-*para*-*meta*- and ps-*meta*-*meta*-PCP molecules, respectively

controlled break junction (MCBJ) by covalent S–Au bonds, guaranteeing both electronic coupling and mechanical stability. The latter is of particular importance to enable subtle mechanical manipulation of the integrated single molecule. The investigation of their transport properties and the influence of mechanical manipulations are studied with MCBJ experiments. The findings are rationalized by QI effects emerging from the interplay of frontier molecular orbitals, discussed with a theoretical model based on density functional theory (DFT). The electronic transport is described in terms of the Landauer formalism [32], expressed through nonequilibrium Green's function (NEGF) methods.

3.2.1. Results and Discussion

The synthesis of the PCP-based model compounds were performed by our collaborators, K. Reznikova and A. Gallego, in Prof. M. Mayor's group, and the details of the synthesis protocol can be found in the supporting information of Ref. [1].

The single-molecule electronic transport properties of PCPs **1-4** were investigated by integrating them into an electronic circuit using an MCBJ setup operated at ambient conditions. Two types of measurements were performed: fast-breaking and electrode displacement modulation experiments. Details of the MCBJ technique, providing a pair of mechanically adjustable electrodes with a distance resolution of atomic dimensions, have been reported previously [33, 34] and are already discussed in chapter 2.

In the fast-breaking experiments, several thousand conductance traces for each investigated molecule were collected and plotted as two-dimensional (2D) histograms displayed in Fig. 3.2. For the case of ps-*para*-*para*- and ps-*meta*-*para*-PCPs with a constant bias voltage of 100 mV, clear conductance plateaus with a length of 12.5 Å were observed, distinguished from direct gold-to-gold tunneling features. Through a reference-free clustering method [35] on the unfiltered data, the pure

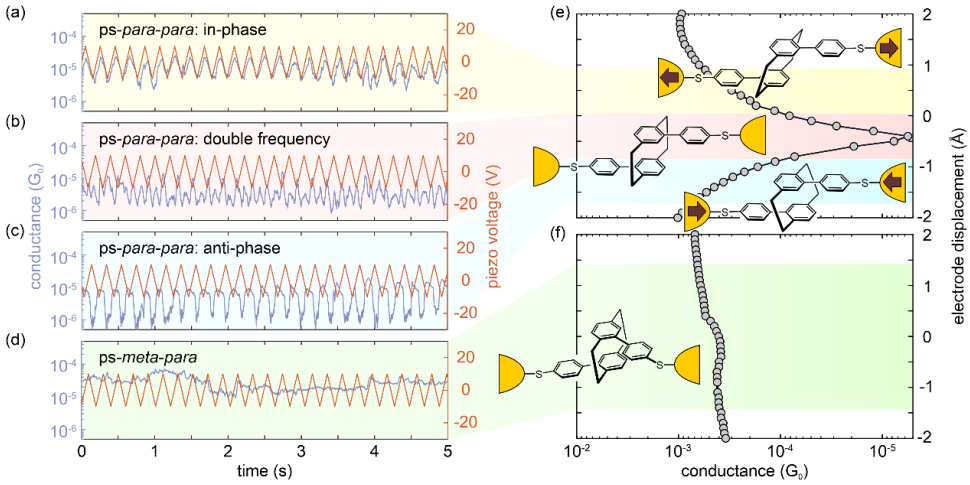

Figure 3.3: (a-c) Conductance traces of modulation experiments with ps-*para*-*para*-PCP (**1**), displaying (a) in-phase, (b) double-frequency and (c) antiphase modulations. (d) Conductance traces of the modulation experiments with ps-*meta*-*para*-PCP (**2**). The red line in the distance-modulation traces represents the voltage applied to the piezoelectric stack, whereas blue represents the meas-ured conductance. The total modulation time of the experiments is 15 s; for better visibility, only 5 s are displayed. (e) Calculated conductance of the ps-*para*-*para*-PCP molecular junction during the gap opening. The conductance displacement data is extracted from Fig. 3.5b, by evaluating the transmission function at the Fermi energy. The sketches rationalize the variety of conductance vs electrode displacement modulation behaviors observed for ps-*para*-*para*-PCP in dependence of the position of the DQI dip with respect to the trapping state of the molecule in the individual junction; see panels a–c and e. In particular, light background colors (yellow, red, and blue) relate the different situations of junctions, including molecules in prestretched, relaxed, or precompressed states, respectively, to the behavior in modulation experiments. (f) Same plot as in panel e but for ps-*meta*-*para*-PCP, where mechanosensitivity is basically absent. The green background color connects the conductance that is rather insensitive to electrode displacements to the observations made in the modulation measurements in panel d.

gold-to-gold tunneling traces and the molecular traces were separated. The molecular conductances of ps-*para*-*para*- and ps-*meta*-*para*-PCPs were obtained through a log-normal fit distribution yielding values of $1.3 \times 10^{-5}\ G_0$ and $2.2 \times 10^{-5}\ G_0$, respectively, where $G_0 = 2e^2/h$ is the quantum of conductance, as shown in the corresponding one-dimensional (1D) conductance histograms (see SI. 2.2 [1]).

For the molecules with the *meta*-phenyl anchoring (ps-*para*-*meta* and ps-*meta*-*meta*) the bias voltage in the transport experiment was increased to 250 mV in order to bring molecular levels closer to resonance, as the conductance of these PCPs was below the detection limit at a bias of 100 mV. However, even at this increased bias voltage, no clear conductance plateaus were detected, even when using the earlier-mentioned clustering method. Whether the lack of clear plateaus is due to molecular conductances below the detection threshold of the experimental setup of $10^{-6}\ G_0$ or the molecules' inability to form stable molecular junctions cannot be distinguished. The very short-breaking traces visible in Fig. 3.2 at higher conductance values for both ps-*para*-*meta*- and ps-*meta*-*meta*-PCP are most likely due to direct electron injection into the molecules' π-systems without controlled

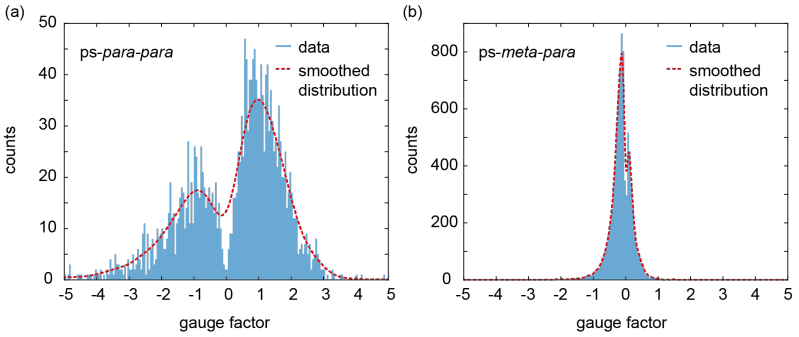

Figure 3.4: Gauge factors obtained from (a) 1442 ps-*para*-*para*-PCP traces and (b) 2236 ps-*meta*-*para*-PCP traces in modulation experiments. The counts are collected from fast Fourier transform (FFT) spectra over 1 s intervals of the traces, which means that there are 15 counts, with different GFs for each recording, lasting 15 s.

sulfur-to-sulfur immobilization.

Of particular interest are the distance-dependent single-molecule junction charge-transport studies of ps-*para*-*para*- and ps-*meta*-*para*-PCPs, as substantial differences in the transport behavior under mechanical stress are expected between the central ps-*para*- and ps-*meta*-PCP subunits. While the mechanosensitivity of the ps-*para*-PCP subunit was already evidenced in modulation experiments for the ps-*para*-*para*-OPE PCP (Fig. 3.1) [30] and rationalized as being due to a distance-dependent conductance dip close to the Fermi level originating from DQI, similar behavior is not expected for the ps-*meta*-PCP subunit, as CQI has been predicted [31].

To study the presence of DQI in more detail, modulation experiments are useful. The modulation procedure consists of constricting the gold wire down to a conductance of $2\ G_0$ with the piezo control [30]. The junction will break by itself due to its surface tension [36]. The electrodes are then separated by 7.5 Å, and a pulse of a triangular waveform with an amplitude of 20 $V_{\text{peak-to-peak}}$ is applied to the piezoelectric element, which corresponds to a modulation amplitude of 5 Å between the electrodes. The conductance is continuously monitored, and the modulation is applied at a frequency of 5 Hz for 15 s. Hereafter, the junction is fused again, and a new modulation trace is recorded. The results of electrode-modulation experiments on PCPs **1** and **2** are summarized in Fig. 3.3.

Similar to ps-*para*-*para*-OPE PCP,[30] a rich variety of distance-modulated conductance responses has been observed for ps-*para*-*para*-PCP (**1**). The periodic electrode displacement caused a substantial conductance modulation, which was either in-phase (Fig. 3.3a), anti-phase (Fig. 3.3c), or even two times the frequency (Fig. 3.3b) of the voltage applied to the piezo stack. As sketched in Fig. 3.3e, this observed mechanosensitivity is caused by the DQI dip in the conductance versus molecular length relation (insets in Fig. 3.3e), with the variety of observed behaviors reflecting the exact position of the conductance dip in the particular molecular junction. We take the in-phase case as an example to explain the observed behav-

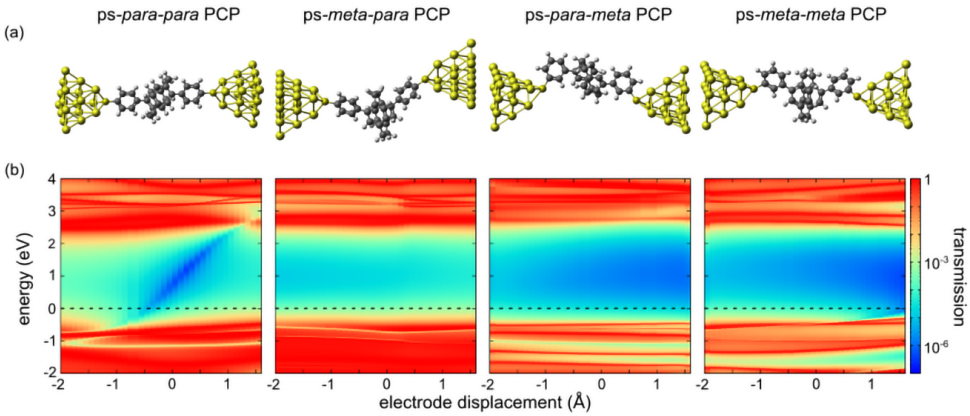

Figure 3.5: (a) Illustration of PCP derivatives **1–4** immobilized in junctions between two gold electrodes. (b) Transmission maps of the four types of PCP single-molecule junctions. The horizontal red resonances in the maps arise from molecular frontier orbitals. For the ps-*para*-*para*-PCP molecule, an antiresonance is observed inside the HOMO−LUMO gap that shifts in energy as the displacement is varied. Similar tunable DQI effects are absent for all other molecules, in particular for ps-*meta*-*para*-PCP junctions and ps-*meta*-*meta*-PCP junctions with central ps-*meta*-PCP systems. The position of the Fermi energy is indicated as a horizontal dashed line.

ior. This corresponds to a starting position in which the molecule is prestretched, as depicted in Fig. 3.3e (top, light yellow background). In this case, whenever the molecule is stretched by increasing the voltage applied to the piezoelectric element, the conductance goes up, and the conductance goes down when the piezo voltage decreases, *i.e.*, the conduction follows the applied piezo-voltage modulation in-phase.

The striking similarity of the mechanosensitivity of ps-*para*-*para*-PCP (**1**) and ps-*para*-*para*-OPE PCP, both comprising a central *para*-PCP subunit, not only points at this structural motif as the origin of the phenomenon but also further corroborates its rationalization based on the presence of a DQI dip in proximity of the Fermi level. Equally interesting are the modulation experiments performed with the ps-*meta*-*para*-PCP (**2**). As displayed in parts d and f of Fig. 3.3, single-molecule junctions with this structure do not feature significant conductance changes during the modulation experiments. Remarkably, the absence of mechanosensitivity of the ps-*meta*-*para*-PCP has not been reported experimentally before. Particularly, this behavior indicates the absence of a transmission dip as a function of electrode displacement (within the displacement window probed by the experiment), suggesting that DQI does not occur in the case of ps-*meta*-PCP cores. This is in agreement with previous predictions of π-stacked systems by the groups of Solomon [28, 29] and Yoshizawa [31].

To quantify the mechanosensitivity of the molecule under investigation, the gauge factor (GF) was determined as the ratio between logarithmic conductance variation and linear electrode displacement (see Sec. 3.4.1 for more details). Fig. 3.4

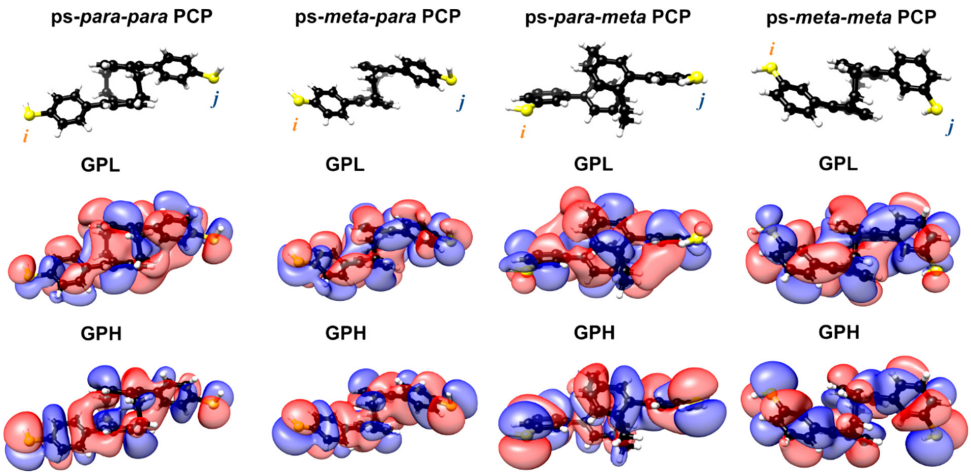

Figure 3.6: HOMO and LUMO molecular frontier orbitals of the ps-*para-para*-, ps-*meta-para*-, ps-*para-meta*-, and ps-*meta-meta*-PCPs. The anchoring sulfur atoms are marked i and j, respectively. Extended representations also including GPH−1 and GPL+1 for each molecule can be found in the SI3.3 [1].

displays the GFs for (a) ps-*para-para*-PCP and (b) ps-*meta-para*-PCP. Indeed, the GFs of the measurements of both structures visualize their difference. While the absence of mechanosensitivity of ps-*meta-para*-PCP results in a sharp peak close to zero (Fig. 3.4b), the GF values recorded for ps-*para-para*-PCP (Fig. 3.4a) display a broad distribution with a minimum at GF = 0, documenting its pronounced mechanosensitivity.

To rationalize the experimental observations described earlier, extensive DFT calculations were performed by our collaborators W. M. Schosser and K. Beltako in Prof. F. Pauly's group. In summary, the four model compounds ps-*para-para*-PCP (**1b**), ps-*meta-para*-PCP (**2b**), ps-*para-meta*-PCP (**3b**), and ps-*meta-meta*-PCP (**4b**) were first optimized in the gas phase. The hydrogen atoms of the terminal thiol groups were then removed, and the molecules were placed in model junctions, consisting of pairs of tetrahedral gold leads (Fig. 3.5a). Optimizing the junction geometry, only the top three gold atoms in the first layer of each tip were allowed to relax, while the rest of the gold cluster remained fixed. Then, the systems were stretched in steps of 0.1 Å, and a geometry optimization was performed at every single step. A detailed description of the established approach [37] and explanations of the calculations are provided in SI. 3.1 [1].

A closer look at the two-dimensional contour plots of transmission, in dependence of energy and electrode displacement in Fig. 3.5, reveals important information about the transmission behavior of the molecular junctions inside the electronic gap between the highest occupied molecular orbital (HOMO) and the lowest unoccupied molecular orbital (LUMO). In the case of the ps-*para-para*-PCP, a transmission valley (blue diagonal trace) with transmission values lower than 10^{-5} is observed between the molecular frontier orbitals (red horizontal traces). The transmission valley corresponds to the DQI conductance dip, as shown in Fig. 3.3e. The energy

position of the transmission minimum can be tuned by mechanical manipulation of the junction. It should be noted that the DQI crosses the complete HOMO−LUMO gap, making it a robust feature for experimental detection, because it does not depend on the precise position of the Fermi energy. A similar valley is not present for the ps-*meta*-*para*-PCP junction. Instead, the transmission stays rather constant in the range of $\approx 10^{-3} - 10^{-4}$ inside the molecule's HOMO−LUMO gap. Rather uniform transmission values are furthermore predicted in the molecules' electronic gap for both ps-*para*-*meta*- and ps-*meta*-*meta*-PCP. Interestingly, for this pair of model compounds with terminal *meta*-benzene linkers, about one order of magnitude lower transmission values were calculated compared to the pair with terminal *para*-benzene linkers. This is also in line with the absence of measurable conductance plateaus for the *meta*-phenyl-connected PCPs in Fig. 3.2.

The conductance computed within the DFT-NEGF formalism [37] at the Fermi energy is plotted in parts e and f of Fig. 3.3 for ps-*para*-*para*- and ps-*meta*-*para*-PCP derivatives, respectively. Considering the example of the ps-*para*-*para*-PCP single-molecule junction, the conductance features a dip that is shifted toward negative displacements and is about two orders of magnitude lower than the base value. Molecular contacts constructed from ps-*meta*-*para*-PCP show instead a rather constant behavior in the studied displacement range without a DQI dip.

While the calculated transmission plots perfectly support the hypothesis that mechanosensitivity can exclusively be observed for structures with a central ps-*para*-PCP subunit providing DQI, another qualitative argument is provided by considering orbital symmetry rules, as suggested by Yoshizawa and coworkers [31, 38]. The qualitative prediction of QI phenomena is based on the interplay of molecular frontier orbitals, especially the HOMO and LUMO, in transport models using Landauer−Büttiker scattering theory and Green's function methods (details are provided in the SI. 3.3 [1]). Thus, the gas-phase frontier orbitals of the model compounds with terminal thiol groups were calculated and are displayed in Fig. 3.6.

Assuming that the Fermi energy of the electrodes lies between the molecule's HOMO and LUMO energies due to charge neutrality, two orbital rules apply for the electronic transport properties [31, 38]. (1) The weights of the HOMO and LUMO wave functions on the anchoring atoms i and j (see Fig. 3.6) need to be of decent size to yield a fair contribution to the transmission. (2) If the parities of the molecule's HOMO and LUMO on the anchoring atoms are different in sign, transport is symmetry-supported through CQI, which is typically reflected in a high transmission inside the HOMO−LUMO gap. If HOMO and LUMO parities are the same instead, the related molecular orbital resonances cancel each other out at a certain energy inside the HOMO−LUMO gap. As a consequence, transport is symmetry-inhibited, resulting in a DQI dip in the energy-dependent transmission function, typically leading to a reduced conductance of the single-molecule junction; provided that HOMO and LUMO orbital wave functions are of similar character on the termini i and j.

The analysis of the molecules started by defining the terminal sulfur atoms as anchoring sites i and j (see Fig. 3.6). Comparing orbital wave functions on the terminal sulfur atoms shows that gas-phase HOMO (GPH) and gas-phase LUMO (GPL) of

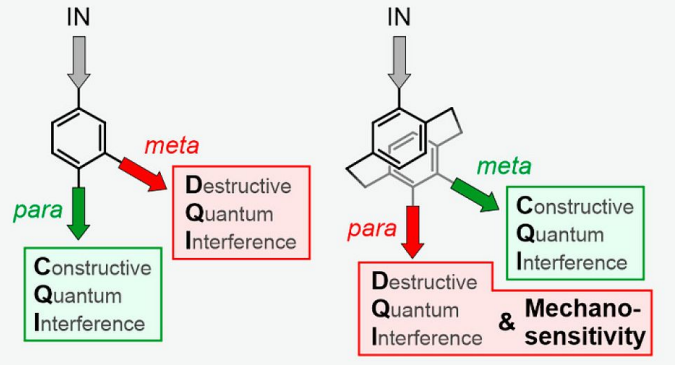

Figure 3.7: Summary of the orbital rules in the PCP model compounds.

both model compounds comprising a central *para*-PCP (ps-*para*-*para*- and ps-*para*-*meta*-PCP) are of similarly oriented π-character at the sulfur atoms and have the same parities; thus, these structures should show DQI. In contrast, both molecules with a ps-*meta*-PCP subunit have different parities in their GPH and GPL on the terminal sulfur atoms and thus exhibit CQI. The orbital symmetry rules thus rationalize the experimental observations and numerical computations reported earlier, which identify the central ps-*para*-PCP subunit as the origin of DQI.

Let us point out that ferrocene recently emerged as a related 3D system to the PCP, where the angle between two cyclopentadienyl decks can be tuned rather continuously around the central Fe core atom [39]. The torsion can be compared to changing from *meta* to *para* connection to the PCP. The mechanical distortion that explains the experimental results here is mainly the displacement of two benzene rings as compared to a rotation.

3.2.2. Conclusion

We have studied the electronic transport properties of single-molecule junctions based on π-stacked hydrocarbons. Our study confirms previous theoretical predictions for model compounds in terms of molecular orbital symmetry rules with regard to the suppression of electronic transport in PCP subunits when contacted in ps-*para* geometry as compared to ps-*meta* geometry. While the ps-*meta* subunit generally shows high conductance in comparison to the ps-*para* geometry (still relatively low compared to other conjugated molecular wires such as OPE3-dithiol [40]) and little sensitivity to mechanical manipulation, the ps-*para* subunit offers an exceptional mechanoelectric sensitivity. This result is summarized in Fig. 3.7. Notably, our theoretical calculations predict that the DQI can be tuned through the complete electronic gap region, explaining the experimental robustness of the feature, as observations are largely independent of the precise location of the Fermi energy. Similar to an optical Fabry–Pérot interferometer, the DQI feature can be used to detect minute displacement changes and hence serves as a quantum sensor operating at ambient conditions, *i.e.*, at room temperature.

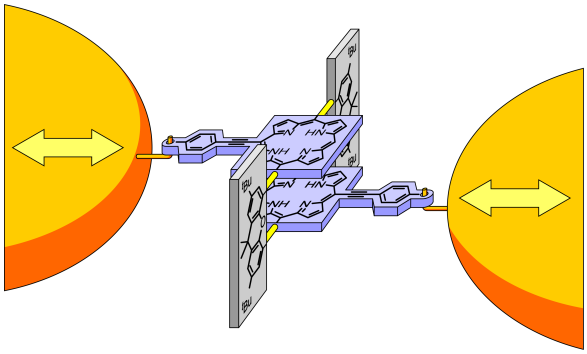

Figure 3.8: Cartoon representation of the molecular architecture embedded between two gold electrodes for distance modulation experiments. *para*-ethynylbenzenethiol expanded porphyrin decks are sketched in light blue, planar bridging xanthene units in grey, and the revolving acetylene joints in light yellow. The anchoring S-Au bonds, mounting the molecule to the electrodes, are depicted as hooks. While the chemical structure is already indicated, please see Fig. 3.9 for the exact representations of the studied molecules PC1 and ZnPC1.

3.3. Cofacial porphyrin cyclophane

To explore the potential and limitations of mechanically triggered molecular structures, cyclophanes providing significantly increased π-surfaces are interesting target structures. Porphyrins are especially promising building blocks for molecular devices [41]. Recently, the successful synthesis and characterization of mechanically fixed and flexible cofacial porphyrin cyclophanes were demonstrated [42, 43]. The molecular concept is sketched in Fig. 3.8: Two porphyrins are expanded by a *para*-ethynylbenzenethiol subunit to enable their fixation at the electrode surface (blue in Fig. 3.8). To integrate mechanosensitivity, both porphyrins are interconnected by a pair of rigid xanthene subunits (grey in Fig. 3.8), which are mounted by acetylenes as revolving joints (light yellow bars in Fig. 3.8). As a consequence the integrated porphyrin cyclophane (PC) can adapt to distance variations of both electrodes in a sliding motion between both porphyrins. It is, however, worth mentioning that upon pulling and pushing also the distance between both porphyrin planes varies due to the variation of the angle between the interlinking xanthene subunits and the porphyrin planes. By integration of the model compounds PC1 and ZnPC1, displayed in Fig. 3.9, into a MCBJ experiment, the resulting mechanosensitivity is investigated and benchmarked with simulated expectations. Preliminary results with ZnPC1 in a MCBJ set-up showed sufficient electronic transparency of the structure for the envisioned single-molecule transport experiments, in spite of its dimension [43].

Here, we report on the DFT-NEGF analysis and MCBJ experiments of the mechanosensitive charge transport through molecular junctions formed by the cofacial porphyrin cyclophanes PC1 and ZnPC1. Particularly, we present MCBJ studies, directly probing the theoretically predicted multiple destructive quantum interference (DQI) features by periodic electrode modulations. Distance-dependent energetic arrangements of the frontier orbitals explain the multiple interference features, which for a

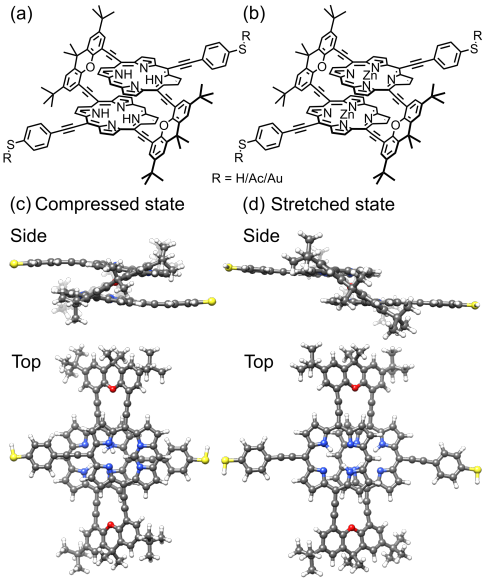

Figure 3.9: Chemical structure of the studied molecules (a) PC1 and (b) ZnPC1. Each of the two central metal Zn ions in ZnPC1 is replaced by two H atoms in PC1. In solution, R represents an acetate (Ac), as synthesized. After *in situ* deprotection on the gold wire, R is either a hydrogen (H) atom or gold (Au). Side and top views of ball-and-stick representations of calculated (c) compressed and (d) stretched states of PC1 in the gas phase with R = H. Note that compressed and stretched geometries in panels (c) and (d) are both energetic minima.

stack of two porphyrins are richer than for the previously reported paracyclophane stacks of single benzene rings [1, 30]. The richness stems from the more extended intramolecular π-systems and the higher mechanical flexibility, enabling larger sliding distances of the two covalently linked molecular porphyrin decks with respect to each other.

3.3.1. Results and Discussion

In the following sections, we present the results of PC1, synthesized by P. Zwick from M. Mayor's group at University of Basel, see Figs. 3.8 and 3.9. Since ZnPC1 shows a similar behavior, it is discussed in the supporting information in Ref. [2]. The theoretical calculations were performed by W. Schosser and K. Beltako from F. Pauly's group at University of Augsburg. Here, we only discuss the outcome of the calculations, and the details of the simulations can be found in Ref. [2].

Theoretical

The mechanical motion of the molecule during the stretching process is first described in detail in the following. Starting from the compressed molecular state, see Fig. 3.10a, the junction's total energy increases initially to a local maximum at 5.3 Å, see Fig. 3.11a. Up to this point both porphyrin planes glide over each other in a well-aligned manner, while they slightly separate due to the spatial constraints

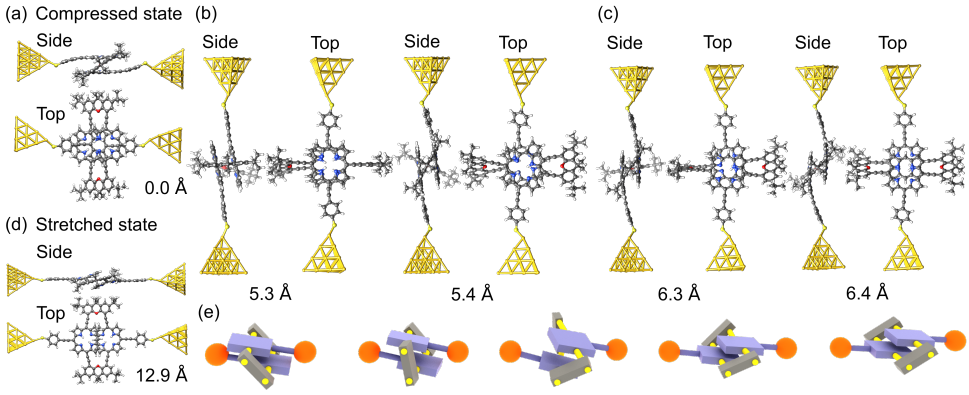

Figure 3.10: PC1 junction geometries in side and top views during the stretching process (a) in the compressed molecular state at an electrode displacement of $d \approx 0$ Å, (b) at the first and (c) at the second bridge flip at $d \approx 5.3$ Å and $d \approx 6.3$ Å, respectively, and (d) in the stretched state at $d = 12.9$ Å. In the junctions, hydrogen atoms at the thiol termini are removed as compared to the gas phase geometries in Fig. 3.9c and d. (e) Sketch of the evolution of the molecular geometry of PC1 with increasing electrode separation. The molecule is connected to gold tip atoms through terminal sulfur atoms on each side. The electrodes are not displayed in this simplified representation.

set by the rigid bridges. The bridges themselves evolve in this displacement interval from a rather flat orientation to a perpendicular angle with respect to the porphyrin planes. At 5.3 Å the total energy decreases abruptly, as the junction releases its tension. This happens through a conformational rearrangement of the molecule, which involves the flipping of a single bridge, see Fig. 3.10b. The process reduces the distance between the porphyrin planes and at the same time twists them with respect to each other. Due to the attractive van der Waals interactions between the π-systems of the two decks, this intermediate state is energetically favorable. Between 5.3 Å and 6.3 Å the energy rises slightly, while the twist is gradually removed and the porphyrin planes separate. At 6.4 Å the energy of the junction decreases again. This is the result of the flipping of the second bridge, see Fig. 3.10c. The molecule has now reached a state that resembles the stretched one in Fig. 3.10d, where the porphyrin planes are aligned in parallel without any twist, as is visible in Fig. 3.10c at an electrode displacement of $d = 6.4$ Å. With growing electrode separation the xanthene bridges flatten, the porphyrin planes get closer to each other, while the sliding continuously reduces the intramolecular overlap of the electronic π-systems. In this final elastic phase the total energy rises, until the molecule is fully stretched out, see Fig. 3.10d, and the contact ruptures at 13 Å. Note that the porphyrins decks are slightly bent before the junction breaks. This differs from the planar configuration in the energy-optimized stretched state of the gas phase, see Fig. 3.9d, and is due to the mechanical tension exerted by the electrodes. As the inset of Fig. 3.11a depicts, the junction breaks at an applied force or around 1.3 nN. The mechanical motion of the molecule during the stretching is summarized in a simplified illustration in Fig. 3.10e.

The conductance shows a pronounced distance dependence during the stretch-

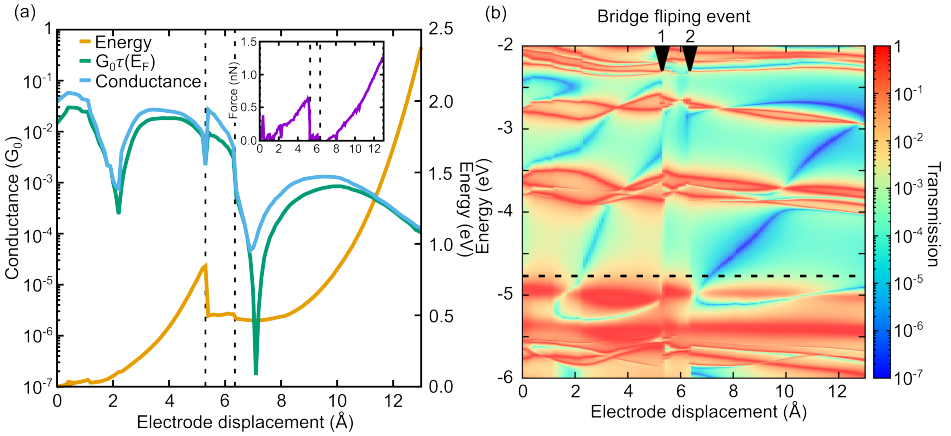

Figure 3.11: (a) Energy and conductance as a function of electrode displacement. The inset shows the force applied to the junction. The room-temperature conductance at $T = 300$ K, computed from the Landauer formula, is compared to the low-temperature approximation $G \approx G_0\tau(E_F)$. Zero displacement corresponds to the compressed junction state, shown in Fig. 3a. The vertical dashed lines indicate bridge flipping events, see Fig. 3.10b and c. (b) Transmission as a function of energy and electrode displacement for the single-molecule junction of Fig. 3.10. Arrows at the top of the plot mark bridge flipping events. The horizontal dashed line shows the Fermi energy E_F. Running along it yields the low-temperature approximation of the conductance $G \approx G_0\tau(E_F)$, shown in panel (a).

ing process, as evident from Fig. 3.11a, where conductance is expressed in units of the conductance quantum, G_0. Especially the two sharp dips at 2.1 Å and 7.3 Å emphasize the large mechanical tunability of the conductance. In the low-temperature approximation $G \approx G_0\tau(E_F)$ (green curve), it can be tuned by two or four orders of magnitude, respectively, while a substantial increase of dip values is present when taking an electronic thermal broadening at $T = 300$ K into account (light blue curve) (see Ref. [2] on how the temperature-dependent conductance from the energy-dependent transmission $\tau(E)$ is determined). For a better understanding of electron transport, the energy- and distance-dependent transmission of the molecular junction is studied, as displayed in Fig. 3.11b. The two bridge-flipping processes, discussed above, manifest themselves in the transmission map as sharp vertical discontinuities at 5.3 Å and 6.3 Å , respectively. The dips in the distance-dependent conductance of Fig. 3.11a (light blue and green curves) are caused by two (light blue and dark blue) valleys in Fig. 3.11b. They correspond to transmission values below $10^{-3}$and 10^{-6} inside the electronic gap between HOMO and LUMO states. More precisely, they arise between the almost horizontal red resonance lines at about -5 eV and -3.7 eV, which are related to the molecular frontier orbitals. Since the energy position of the transmission trenches depends on the electrode separation, the conductance can be tuned mechanically. Let us emphasize that since these two transmission valleys cross the entire HOMO-LUMO gap, they are robust features that can be experimentally observed independent of the precise position of the Fermi energy. It is found that ZnPC1 shows a similar molec-

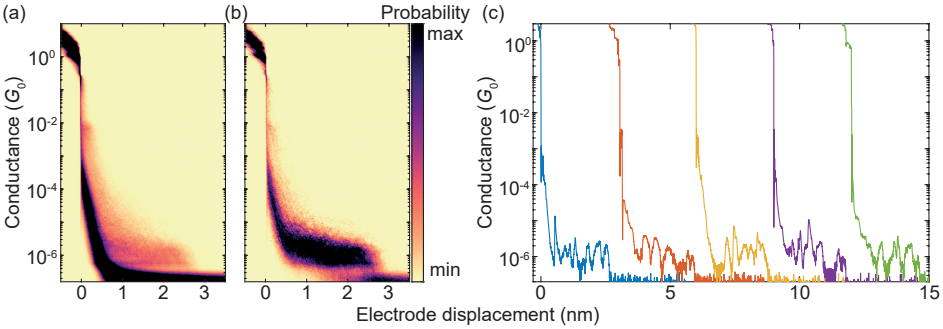

Figure 3.12: Fast-breaking measurement of PC1. (a) 2D conductance-displacement density plot consisting of 10000 consecutive fast-breaking traces. (b) 2D histogram containing only molecular traces, obtained through a reference-free clustering algorithm [35]. (c) Five examples of individual breaking traces, each displaced by hand by 3 nm to ensure good visibility.

ular motion and corresponding DQI features [2].

Experimental

A two-dimensional (2D) histogram with 10000 consecutive fast-breaking traces obtained with PC1 is displayed in Fig. 3.12a. A reference-free clustering algorithm [35] was used to separate traces with molecular features from the direct tunneling ones. The result of the extraction is shown in Fig. 3.12b. A clear conductance plateau around 2×10^{-6} is identified, excellently matching the value of its derivative ZnPC1, as reported previously [42]. From this fast-breaking measurement an average length of the breaking trace of 2.3 nm is obtained, lying between the calculated sulfur-to-sulfur lengths of the compressed (2.07 nm) and stretched (2.77 nm) states of the molecule. This finding not only confirms PC1's remarkable single-molecule junction stability in the desired sulfur-connected configuration, which is similar to its Zn derivative, but further suggests that the underlying transport mechanism is influenced negligibly by the presence or absence of Zn atoms in the cyclophane-embedded porphyrins. This conclusion is in agreement with studies on single-porphyrin junctions [44].

Figure 3.12c shows five individual breaking traces of PC1. Multiple oscillations in the conductance up to 1.5 orders of magnitude are visible during the breaking events, demonstrating the largest reported mechanosensitivity in the case of cyclophane-like systems [45]. Similar conductance variations in [2.2]paracyclophane single-molecule junctions have been attributed to a stick-slip motion between the anchoring group and the gold electrodes, which enables the molecule to get close to or even cross the DQI-related transmission dip several times in a single breaking event [30]. As shown in Fig. 3.11a, the theoretically predicted breaking trace of a single-molecule junction formed by PC1 features two large conductance oscillations as a result of DQI even without stick-slip motion. It is difficult to distinguish, however, if multiple conductance oscillations arise from crossing several valleys in the transmission-displacement landscape or if they are caused by repeated

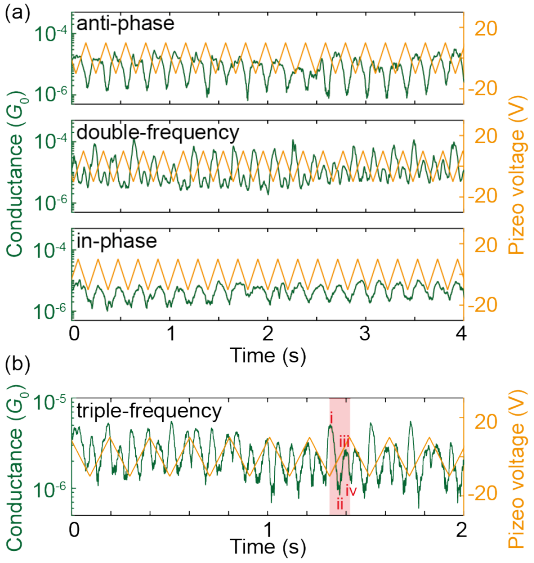

Figure 3.13: Electrode-displacement modulation experiments with PC1. (a) Anti-phase, double-frequency and in-phase responses to the piezo voltage. The dip-to-peak piezo voltage modulation corresponds to an electrode displacement of 5 Å. We apply the piezo voltage signal at a frequency of 5 Hz. Note that the electrode displacement increases (decreases) as the piezo voltage increases (decreases). (b) Triple-frequency response to the piezo voltage. The red-shaded area is a guide to the eye for a half-period modulation.

stick-slip events in a particular breaking trace or both.

Electrode-displacement modulation measurements were performed to repetitively probe the predicted transmission-displacement landscape of Fig. 3.11b. Figure 3.13a shows anti-phase, double-frequency and in-phase responses, which can be assigned to different starting positions of the modulation measurements in the transmission map in a similar way as described for PCP in Fig. 3.3. The anti-phase behavior corresponds to a starting position at the left of a DQI dip, where the conductance decreases as the electrodes separate, while the in-phase response results from a starting position at the right of a DQI dip, where the conductance increases as the electrodes move further apart. Finally, the double-frequency case coincides with a starting position so close to a DQI dip that the conductance increases as the electrodes either open or close. These three response behaviors experimentally verify the presence of at least one valley in the energy-displacement transmission map.

In addition to these three responses, we observed higher frequency conductance oscillations, which was not present in the case PCP molecules. Figure 3.13b shows an example of a triple-frequency response (see SI. 2.4 for more examples with both PC1 and ZnPC1 [2]). In this case, in one modulation cycle the conductance oscillates up and down three times. Zooming in on one single increase of electrode displacement in Fig. 3.13b, *i.e.*, half of a period (the red shaded area for

example), the molecule starts in (i) a high-conductance state, (ii) passes a pronounced minimum, (iii) recovers to a high-conductance state and (iv) decreases again to a minimal value. To understand this behavior, we take Fig. 3.11a as a guide to trace the conductance change. When the molecule is stretched starting from its initial position at $d = 0$ Å, the computed conductance (i) takes a high value, (ii) drops when approaching the first DQI dip, (iii) increases when leaving the first DQI dip, (iv) decreases again when approaching the second DQI dip. The experimental observations are thus in agreement with the interpretation of the molecule fully crossing one DQI dip and partially entering the second DQI dip. This interpretation is furthermore consistent with the applied modulation amplitude of 5 Å, which does not allow the molecule to fully cross two DQI dips according to the calculations.

To realize a full crossing of two DQI dips, a larger modulation amplitude is required. Excitingly, electrode-displacement modulation experiments with an amplitude of 10 Å were successfully conducted without losing contact to the molecule, while the conductance signal was recorded continuously as a function of time. In rare cases quadruple frequency responses were observed (see bottom panel of Fig. 3.15 for an exemplary single trace of a 1 nm gap-size modulation using ZnPC1, embracing the full crossing of both DQI dips in the predicted transmission landscape of Fig. 3.11b) [2]. The characteristic is not as clear as the triple-frequency response in Fig. 3.13b, and the large gap-size manipulation is expected to increase the chance of inducing a slipping motion of the anchoring group on the gold electrodes, which we cannot distinguish.

3.3.2. Conclusion

We have presented a combined theoretical and experimental study of charge transport through the porphyrin cyclophane PC1 as well as its derivative ZnPC1. DFT-based calculations predict that during the pulling of the molecular junctions, π-orbitals do not continuously slide over each other. Instead, typically one of the two bridges flips first, followed by the second bridge flip at a later stage. The complex motion of the two conjugated molecular decks leads to two dips in conductance-displacement curves, since there are two such transmission features crossing the entire HOMO-LUMO gap as a function of electrode separation.

We have experimentally demonstrated a large mechanosensitivity of PC1 at room temperature with conductance variations of up to 1.5 orders of magnitude in fast-breaking measurements. Electrode-displacement modulation experiments show that in addition to the in-phase, anti-phase and double-frequency response, higher frequency modes are observed. This remarkable experimental detection of higher frequency responses may evidence the presence of the two theoretically predicted robust conductance dips.

For future work, the twisting of molecular decks might be avoided by attaching two bridges at each side of π-stacked dimer, thus lowering angular freedom and hence stabilizing a more continuous sliding. At the same time the increased rigidity needs to be balanced against the interfacial stiffness, *i.e.*, Au-Au and Au-S bond strengths, to preserve the possibility of mechanical manipulation. Further

molecular designs need to be explored in order to better understand the rich variety of mechanosensitive responses and to create novel quantum sensors based on mechanosensitive molecular systems.

3.4. Appendix

3.4.1. Gauge factor analysis

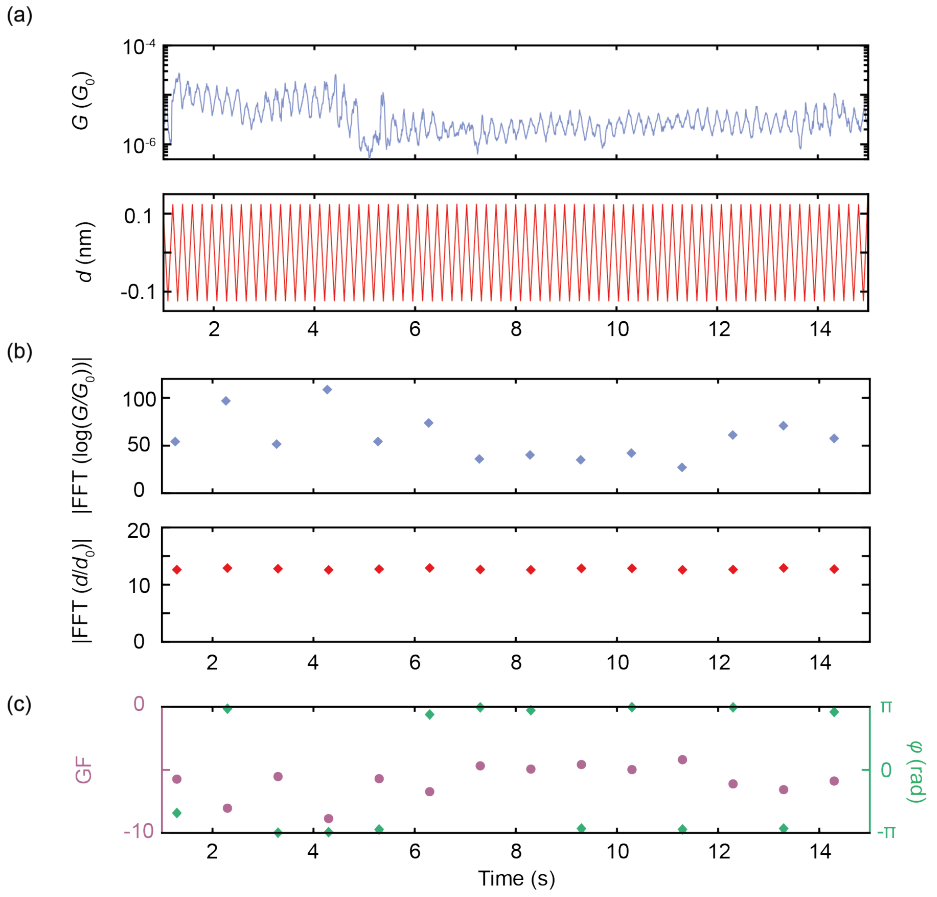

Figure 3.14: GF analysis. (a) Raw data of an electrode displacement modulation measurement of the PC2 molecule, shown in Chapter 4. The top panel shows the conductance trace as a function of time, and the bottom panel displays the modulated electrode displacement as a function of time. The modulation amplitude is 2.5 Å. (b) Raw data after the FFT. The top panel visualizes the FFT amplitude of $\log(G/G_0)$ and the bottom panel is the FFT amplitude of d/d_0. Both FFT amplitudes are evaluated at the driving frequency $f = 5$ Hz. (c) GFs and phases of the example data. The GF and phase φ are obtained by taking the ratio of FFT amplitudes shown in panel (b), see Eqs. (3.1) and (3.2).

The displacement modulation measurements, described in the main text, provide a means to study the conductance response of the single-molecule junctions around a selected initial electrode displacement. The general procedure of the statistical gauge factor (GF) analysis is explained in Fig. 3.14. We take the raw signals of conductance and displacement as a starting point, see Fig. 3.14a. Next we perform a fast Fourier transform (FFT) on the two signals, $\log(G/G_0)$ and d/d_0, for

every five cycles of the driving signal. Here, G is the conductance, G_0 is the quantum of conductance $G_0 = 2e^2/h$, d is the electrode displacement, and d_0 is the average length of a single-molecule plateau, as determined from the fast-breaking measurements. To illustrate, how the FFT affects the two input signals, the absolute values of the results are visualized in Fig. 3.14b. Then, we take the ratio of the two FFT results, which gives the complex number

$$z(f) = r(f)e^{i\varphi(f)} = \frac{\mathrm{FFT}(\log(G/G_0))(f)}{\mathrm{FFT}(d/d_0)(f)}, \tag{3.1}$$

with a corresponding frequency-dependent amplitude $r(f)$ and phase $\varphi(f)$. Finally, we define

$$\mathrm{GF} = r(f) \times s, \tag{3.2}$$

with

$$s = \begin{cases} 1, & \text{if } |\varphi(f)| \leq \pi/2, \\ -1, & \text{if } |\varphi(f)| > \pi/2, \end{cases} \tag{3.3}$$

where the phase is assumed to take values in the interval $\varphi(f) \in [-\pi, \pi]$, see also Fig. 3.14, and $f = 5$ Hz is chosen to be the driving frequency of our displacement modulation experiment. Therefore, the GF is positive, if the two signals are in phase, and negative, if they are out of phase.

Let us consider Fig.3.4a as an example. The GF is predominantly positive, suggesting an in-phase relation between G and d. This means that if the electrode displacement increases at this initial electrode displacement position, the conductance typically goes up.

3.4.2. Higher order frequency responses

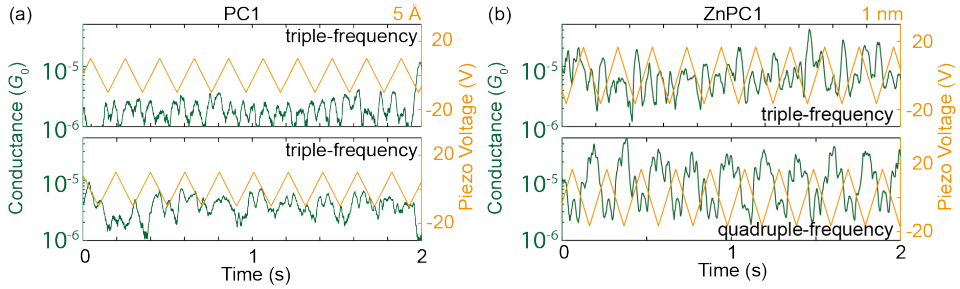

Figure 3.15: Higher order frequency responses of molecular junctions containing PC1 and ZnPC1. (a) Examples of triple-frequency response for PC1. The modulation setting is the same as in the main text with an amplitude of 5 Å (piezo voltage of ± 10 V). (b) Examples showing higher order frequency responses for ZnPC1. The top panel displays a triple-frequency response and the bottom panel shows a quadruple-frequency response. Note that a larger modulation amplitude of 1 nm (piezo voltage of 20 V) was used for both measurements with ZnPC1.

Further examples of higher order frequency modes are presented in Fig. 3.15 for PC1 and ZnPC1. For PC1 an electrode-displacement amplitude of 5 Å is used and triple-frequency behavior is observed, similar to what we describe in the main text. For ZnPC1, a larger modulation amplitude of 1 nm yields in addition to the triple-frequency mode, see the upper panel of Fig. 3.15b, a quadruple-frequency mode, see the bottom panel of Fig. 3.15b. This latter case may be attributed to a full crossing of two DQI dips, as discussed in the main text. However, the characteristic is not as clear as the triple-frequency response, and the large modulation amplitude used here may possibly induce a slipping of the molecule in the junction.

References

(1) Reznikova, K.; Hsu, C.; Schosser, W. M.; Gallego, A.; Beltako, K.; Pauly, F.; van der Zant, H. S. J.; Mayor, M. *Journal of the American Chemical Society* **2021**, *143*, 13944–13951.

(2) Schosser, W. M.; Hsu, C.-W.; Zwick, P.; Beltako, K.; Dulić, D.; Mayor, M.; van der Zant, H. S. J.; Pauly, F. *Nanoscale* **2022**, *14*, 984–992.

(3) Van der Molen, S. J.; Naaman, R.; Scheer, E.; Neaton, J. B.; Nitzan, A.; Natelson, D.; Tao, N. J.; van der Zant, H. S. J.; Mayor, M.; Ruben, M.; Reed, M.; Calame, M. *Nature Nanotechnology* **2013**, *8*, 385–389.

(4) Aviram, A.; Ratner, M. A. *Chemical Physics Letters* **1974**, *29*, 277–283.

(5) Luo, L.; Choi, S. H.; Frisbie, C. D. *Chemistry of Materials* **2011**, *23*, 631–645.

(6) Huber, R.; González, M. T.; Wu, S.; Langer, M.; Grunder, S.; Horhoiu, V.; Mayor, M.; Bryce, M. R.; Wang, C.; Jitchati, R.; Schönenberger, C.; Calame, M. *Journal of the American Chemical Society* **2008**, *130*, 1080–1084.

(7) Irie, M.; Fukaminato, T.; Sasaki, T.; Tamai, N.; Kawai, T. *Nature* **2002**, *420*, 759–760.

(8) Liao, J.; Agustsson, J. S.; Wu, S.; Schõnenberger, C.; Calame, M.; Leroux, Y.; Mayor, M.; Jeannin, O.; Ran, Y. F.; Liu, S. X.; Decurtins, S. *Nano Letters* **2010**, *10*, 759–764.

(9) Elbing, M.; Ochs, R.; Koentopp, M.; Fischer, M.; von Hanisch, C.; Weigend, F.; Evers, F.; Weber, H. B.; Mayor, M. *Proceedings of the National Academy of Sciences* **2005**, *102*, 8815–8820.

(10) Lörtscher, E.; Gotsmann, B.; Lee, Y.; Yu, L.; Rettner, C.; Riel, H. *ACS Nano* **2012**, *6*, 4931–4939.

(11) Naher, M.; Milan, D. C.; Al-Owaedi, O. A.; Planje, I. J.; Bock, S.; Hurtado-Gallego, J.; Bastante, P.; Abd Dawood, Z. M.; Rincón-García, L.; Rubio-Bollinger, G.; Higgins, S. J.; Agraït, N.; Lambert, C. J.; Nichols, R. J.; Low, P. J. *Journal of the American Chemical Society* **2021**, *143*, 3817–3829.

(12) Stadler, R.; Markussen, T. *The Journal of Chemical Physics* **2011**, *135*, 154109.

(13) Markussen, T.; Stadler, R.; Thygesen, K. S. *Nano Letters* **2010**, *10*, 4260–4265.

(14) Jiang, F. et al. *Angewandte Chemie - International Edition* **2019**, *58*, 18987–18993.

(15) Venkataraman, L.; Klare, J. E.; Nuckolls, C.; Hybertsen, M. S.; Steigerwald, M. L. *Nature* **2006**, *442*, 904–907.

(16) Aradhya, S. V.; Meisner, J. S.; Krikorian, M.; Ahn, S.; Parameswaran, R.; Steigerwald, M. L.; Nuckolls, C.; Venkataraman, L. *Nano Letters* **2012**, *12*, 1643–1647.

(17) Mayor, M.; Weber, H. B.; Reichert, J.; Elbing, M.; Von Hänisch, C.; Beckmann, D.; Fischer, M. *Angewandte Chemie - International Edition* **2003**, *42*, 5834–5838.

(18) Koga, J.; Tsuji, Y.; Yoshizawa, K. *Journal of Physical Chemistry C* **2012**, *116*, 20607–20616.

(19) Arroyo, C. R.; Tarkuc, S.; Frisenda, R.; Seldenthuis, J. S.; Woerde, C. H.; Eelkema, R.; Grozema, F. C.; Van Der Zant, H. S. J. *Angewandte Chemie - International Edition* **2013**, *52*, 3152–3155.

(20) Kiguchi, M.; Kaneko, S. *Physical Chemistry Chemical Physics* **2013**, *15*, 2253–2267.

(21) Lambert, C. J. *Chemical Society Reviews* **2015**, *44*, 875–888.

(22) Kiguchi, M.; Nakamura, H.; Takahashi, Y.; Takahashi, T.; Ohto, T. *Journal of Physical Chemistry C* **2010**, *114*, 22254–22261.

(23) Arroyo, C. R.; Frisenda, R.; Moth-Poulsen, K.; Seldenthuis, J. S.; Bjørnholm, T.; van der Zant, H. S. J. *Nanoscale Research Letters* **2013**, *8*, 2–7.

(24) Li, X.; Staykov, A.; Yoshizawa, K. *Journal of Physical Chemistry C* **2010**, *114*, 9997–10003.

(25) Yoshizawa, K.; Tada, T.; Staykov, A. *Journal of the American Chemical Society* **2008**, *130*, 9406–9413.

(26) Yoshizawa, K. *Accounts of Chemical Research* **2012**, *45*, 1612–1621.

(27) BROWN, C. J.; FARTHING, A. C. *Nature* **1949**, *164*, 915–916.

(28) Solomon, G. C.; Herrmann, C.; Vura-Weis, J.; Wasielewski, M. R.; Ratner, M. A. *Journal of the American Chemical Society* **2010**, *132*, 7887–7889.

(29) Solomon, G. C.; Vura-Weis, J.; Herrmann, C.; Wasielewski, M. R.; Ratner, M. A. *Journal of Physical Chemistry B* **2010**, *114*, 14735–14744.

(30) Stefani, D.; Weiland, K. J.; Skripnik, M.; Hsu, C.; Perrin, M. L.; Mayor, M.; Pauly, F.; van der Zant, H. S. J. *Nano Letters* **2018**, *18*, 5981–5988.

(31) Li, X.; Staykov, A.; Yoshizawa, K. *Bulletin of the Chemical Society of Japan* **2012**, *85*, 181–188.

(32) Perdew, J. P. *Physical Review B* **1986**, *34*, 7406.

(33) Martin, C. A.; Ding, D.; van der Zant, H. S. J.; van Ruitenbeek, J. M. *New Journal of Physics* **2008**, *10*, 065008.

(34) Martin, C. A.; Smit, R. H. M.; Egmond, R. V.; van der Zant, H. S. J.; van Ruitenbeek, J. M. *Review of Scientific Instruments* **2011**, *82*, 053907.

(35) Cabosart, D.; El Abbassi, M.; Stefani, D.; Frisenda, R.; Calame, M.; van der Zant, H. S. J.; Perrin, M. L. *Applied Physics Letters* **2019**, *114*, 143102.

(36) O'Neill, K.; Osorio, E. A.; van der Zant, H. S. J. *Applied Physics Letters* **2007**, *90*, 2005–2008.

(37) Pauly, F.; Viljas, J. K.; Huniar, U.; Häfner, M.; Wohlthat, S.; Bürkle, M.; Cuevas, J. C.; Schön, G. *New Journal of Physics* **2008**, *10*, 125019.

(38) Tsuji, Y.; Yoshizawa, K. *Journal of Physical Chemistry C* **2017**, *121*, 9621–9626.

(39) Camarasa-Gómez, M.; Hernangómez-Pérez, D.; Inkpen, M. S.; Lovat, G.; Fung, E. D.; Roy, X.; Venkataraman, L.; Evers, F. *Nano Letters* **2020**, *20*, 6381–6386.

(40) Frisenda, R.; Perrin, M. L.; Valkenier, H.; Hummelen, J. C.; Van der Zant, H. S. J. *Physica Status Solidi (B) Basic Research* **2013**, *250*, 2431–2436.

(41) Zwick, P.; Dulić, D.; van der Zant, H. S. J.; Mayor, M. *Nanoscale* **2021**, *13*, 15500–15525.

(42) Zwick, P.; Weiland, K. J.; Malinčík, J.; Stefani, D.; Häussinger, D.; van der Zant, H. S. J.; Dulić, D.; Mayor, M. *The Journal of Organic Chemistry* **2020**, *85*, 118–128.

(43) Zwick, P.; Hsu, C.; El Abbassi, M.; Fuhr, O.; Fenske, D.; Dulić, D.; van der Zant, H. S. J.; Mayor, M. *The Journal of Organic Chemistry* **2020**, *85*, 15072–15081.

(44) El Abbassi, M.; Zwick, P.; Rates, A.; Stefani, D.; Prescimone, A.; Mayor, M.; van der Zant, H. S. J.; Dulić, D. *Chem. Sci.* **2019**, *10*, 8299–8305.

(45) Li, J.; Shen, P.; Zhen, S.; Tang, C.; Ye, Y.; Zhou, D.; Hong, W.; Zhao, Z.; Tang, B. Z. *Nature Communications* **2021**, *12*, 167.

4

Mechanosensitivity in single molecules: Intra-molecular interactions

Intra- and intermolecular interactions are dominating chemical processes, and their concerted interplay enables complex nonequilibrium states like life. While the responsible basic forces are typically investigated spectroscopically, a conductance measurement to probe and control these interactions in a single molecule far out of equilibrium is reported here. Specifically, by separating macroscopic metal electrodes, two π-conjugated, bridge-connected porphyrins decks are peeled off on one side, but compressed on the other side due to the covalent mechanical fixation. We observe that the conductance response shows an exceptional exponential rise by two orders of magnitude in individual breaking events during the stretching. Theoretical studies atomistically explain the measured conductance behavior by a mechanically activated increase in through-bond transport and a simultaneous strengthening of through-space coupling. Our results not only reveal the various interacting intramolecular transport channels in a molecular set of levers, but also the molecules' potential to serve as molecular electro-mechanical sensors and switches.

Parts of this chapter have been published in *Chemical Science* **2022**, *13*, 8017-8024 [1]. The theoretical calculation was performed by W. M. Schosser and the synthesis was carried out by P. Zwick.

4.1. Introduction

In recent years it has been demonstrated that by stretching molecular junctions, their conductance can change from a few times to even a few orders of magnitude [2–19]. This mechanosensitivity is interpreted either as arising from mechanical manipulation of the molecule-electrode contact or from mechanically triggered structural variations of the integrated molecule. The origin, however, is not always clear. For example, the mechanosensitivity in ferrocene derivatives has been attributed both to redox activity [2] and destructive quantum interference [3]. Another example are conductance measurements of thiophene based molecular rods and a benzil derivative [4, 5]. While both exhibit a very similar two order-of-magnitude conductance change, the former has been explained by hemilabile ligands [5], the latter as the folding of the 1,2-dione subunit [4]. A well-controlled and careful study of single-molecule mechanosensitivity is thus key to gain insights into inter- and intramolecular transport phenomena and the related interactions. This requires a molecular design tailoring either the flexibility of the molecular subunit arrangement or the structural configuration in the molecular junction. For instance, the overlap of molecular orbitals can be controlled mechanically either *via* changing the relative position or the angle between π-orbitals [11, 13–15, 19]. The underlying changes in transport mechanisms resulting from quantum interference [11, 13, 14, 19] and the size of tunnel couplings [15] are revealed by single-molecule measurements.

To explore the interplay between through-bond and through-space intramolecular transport pathways under non-equilibrium conditions, porphyrin cyclophanes have been synthesized as mechanosensitive model compounds [20]. From the perspective of molecular design, these porphyrin cyclophanes are particularly attractive because of the extended π-orbital system with the possibility of further tuning the building blocks' physicochemical properties, *e.g.* by coordinating different metals [21].

In the model compounds 2HPC2 and ZnPC2 studied here, two porphyrin planes are cofacially arranged in a three-dimensional cyclophane architecture (see Fig. 4.1a). While a pair of rigid xanthene bridges separates the two porphyrin planes, these subunits are interconnected by acetylenes as revolving joints. This combination of planar rigid building blocks and revolving linkers provides the intended mechanosensitivity. Both porphyrin decks are further expanded on the same side of the cyclophane, laterally to the bridge, with rigid-rod type phenylacetylenes, exposing each a thioacetate as anchoring group. The nature and the position of the terminal acetyl-masked thiol anchoring groups is of particular importance for the experiments reported in this paper, as the thiol-gold bonds formed upon deprotection are robust enough to allow substantial mechanical manipulation of the immobilized compound. When the molecule is embedded in a mechanically controlled break junction (MCBJ), pulling on the anchoring groups triggers the rotation of both porphyrin planes around aforementioned revolving acetylene joints. In this mechanically controlled process, the porphyrin planes are turned out of their cofacial orientation and, like operating a pair of pincers, the decks are separated in the part above the bridges, while the inter-plane distance below the bridges is decreased

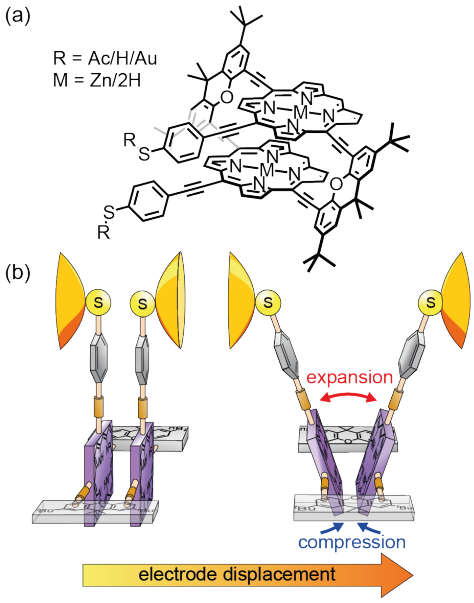

Figure 4.1: (a) Chemical structures of the studied molecules 2HPC2 (M = 2H) and ZnPC2 (M = Zn). R represents an acetate (Ac) as synthesized or a hydrogen (H) or gold (Au) atom after in-situ deprotection on the gold surface. (b) Cartoon-representation of the hypothesized mechanosensitivity of the intramolecularly π-stacked dimer PC2 in an MCBJ experiment.

(see Fig. 4.1b). This change is reflected in the breaking traces by a unique conductance upturn, reaching up to two orders of magnitude. We explain the related changes in transport pathways through detailed atomistic calculations.

4.2. Results & Discussion

Single-molecule characterization

The ZnPC2 molecule studied in this chapter, see Fig. 4.1a, was synthesized following a reported protocol, and its identity was corroborated by its complete characterization including the solid-state structure of a derivate [20]. To characterize its mechanosensitive response, we use the MCBJ technique to perform single-molecule conductance measurements as a function of electrode displacement under dark ambient conditions. A schematic of a MCBJ sample and details of the MCBJ technique can be found in Chap. 2 and in previous reports [23, 24]. First, to examine the possibility to integrate ZnPC2 into a single-molecule junction and characterize its single-molecule conductance, we perform fast-breaking experiments. Data of the fast-breaking measurements with ZnPC2, comprising 10000 consecutive traces, is presented in a two-dimensional (2D) density plot of conductance versus electrode displacement in Fig. 4.2a, at a bias voltage of $V = 250$ mV. Additional fast-breaking results at $V = 100$ mV or without zinc in the porphyrin centers can be found in Apps.4.4.1 and 4.4.2. In Fig. 4.2a we observe two main signatures. First, the

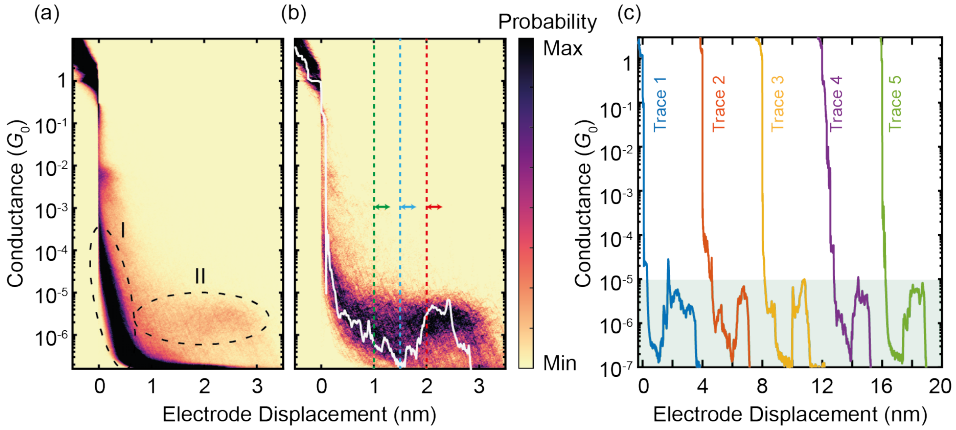

Figure 4.2: (a) Raw data of 10000 consecutive fast-breaking traces, illustrated in a 2D density plot of conductance versus electrode displacement. (b) Same as panel (a) but for 596 molecular traces, corresponding to around 6% of all junctions formed, where pure tunneling traces without molecular conductance signatures are filtered out by a reference-free clustering method [22]. A representative individual breaking trace (white) is plotted, illustrating features visible in the 2D plot. A characteristic rise in the conductance as a function of electrode displacement can be observed after around 1.5 nm. The dashed lines indicate the initial positions of the modulation experiments discussed later. (c), Examples of individual fast-breaking traces. The traces are horizontally offset by 4 nm for clarity. Traces feature a clear conductance increase after a steep initial drop. This conductance increase reaches two orders of magnitude, from $G = 10^{-7}G_0$ to $10^{-5}G_0$ (shaded in green).

conductance decreases as a function of displacement, representing the gold-to-gold direct tunneling transport (region I). Second, a broad plateau with a length of around 2.8 nm appears at conductance values between $10^{-5}G_0$ and $10^{-6}G_0$ (region II), with the quantum of conductance, $G_0 = 2e^2/h$ where e is the electron charge and h is the Planck constant. For further study of the molecular traces, we use a reference-free clustering algorithm to filter out the gold-to-gold direct tunneling traces, yielding the density plot shown in Fig. 4.2b [22].

The extracted molecular traces show a minimum in conductance at an electrode displacement of around 1.5 nm, a subsequent rise and a shorter plateau with a length of 1 nm. These features are robust over many junction configurations, as no further data selection has been applied, and they are evident in the representative individual traces shown in Fig. 4.2c. From the minimum to the subsequent plateau, the conductance increase may amount up to two orders of magnitude in individual breaking events, rivaling the highest switching factor reported for single-molecule junctions of *ortho*-pentaphenylene foldamers [15]. It is worth noting that a conductance increase upon electrode separation has only been documented in a few reports [9, 10, 12, 25]. Generally, they show conductance enhancement by less than a factor of 10. Particularly in the cases of germanium and silicon molecular wires, it is a contact effect rather than an intrinsic molecular feature [9, 10]. This conductance upturn is distinct from the conductance decrease upon electrode separation in *ortho*-pentaphenylene and other single molecules with large

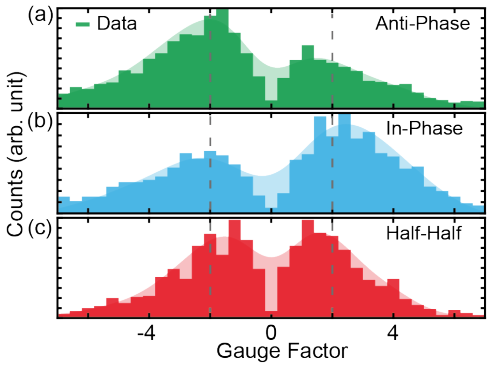

Figure 4.3: (a)-(c) Gauge factors for the different initial electrode displacements, indicated in panel Fig. 4.2b by dashed colored lines. The starting positions for modulations are 1.0, 1.5 and 2.0 nm for (a), (b) and (c), respectively. In all cases, the modulation amplitude is 2.5 Å at a frequency of 5 Hz, applied for a duration of 15 s. The shaded areas represent the smoothed distribution, from which the peak positions are determined. Dotted vertical lines indicate $|\mathrm{GF}| = 2$.

mechanosensitivity studied so far [7, 8, 15]. Evidently, the conductance increase with increasing electrode spacing excludes an explanation involving direct tunneling transport but necessitates transport mechanisms sensing complex rearrangements inside the molecular structure.

To further quantify the conductance response of the single-molecule junctions, we perform electrode displacement modulation experiments. In the modulation measurement (also see Chap. 3 for the modulation method), we modulate the electrode separation with an amplitude of 2.5 Å at different initial electrode displacements, sampling different regions of a molecular breaking trace. After collecting thousands of these modulation traces for the ZnPC2 molecule at different initial displacements, we analyze the gauge factor (GF) to quantify the conductance variations. In the GF analysis we apply a Fourier transform on the conductance data, which specifies both the magnitude and complex phase of a conductance change for a corresponding change in electrode displacement, see Sec. 3.4.1 for more details. For example, a molecular junction with a large in-phase conductance modulation, *i.e.*, an increase of conductance with increasing electrode displacement, is characterized by a large positive GF. Based on the conductance-displacement traces in Fig. 4.2b, we expect the size and sign of the GF to depend on the initial displacement.

GFs of the modulation experiments with initial electrode displacements of 1.0, 1.5 and 2.0 nm, indicated by the green, blue and red dotted vertical lines in Fig. 4.2b, are displayed in Fig. 4.3. Notably, each initial electrode displacement corresponds to a different prevalent phase relation in the GF. In the case of an initial electrode displacement of 1.0 nm we observe more anti-phase (negative) GFs. This means that the conductance of the molecular junction statistically decreases when the junction is opened, in agreement with the negative slope observed in Fig. 4.2b. Similarly, when in-phase behavior (positive GF) predominates at an initial displace-

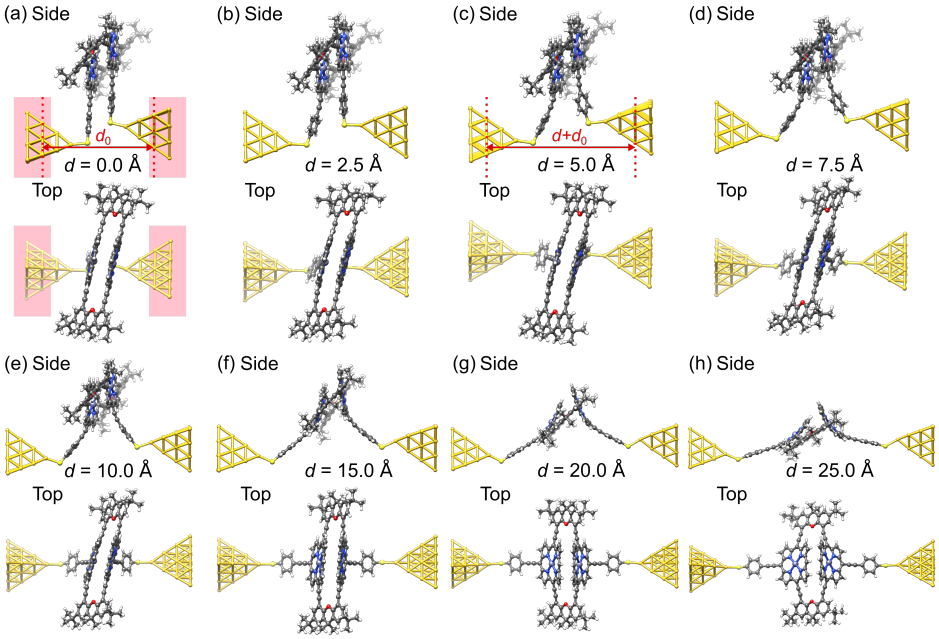

Figure 4.4: (a)-(h) Geometries obtained for a simulated unfolding process of a ZnPC2 single-molecule junction. The junction geometries are shown in side and top views at various displacements d of the gold electrodes. The displacement d is defined as the horizontal shift between the fixed layers of the gold electrodes with respect to their initial separation d_0, see panels (a) and (c). For $d = 0$ Å the red background indicates, which atoms of the extended central cluster are kept fixed, while the rest is optimized. Panels (a) and (b) belong to geometries in region (i), (c) and (d) to region (ii), (e) and (f) to region (iii), and (f) and (h) to region (iv), as defined in Fig. 4.5.

ment of 1.5 nm, molecular conductance essentially increases with increasing electrode separation, corresponding to the upturn in conductance. For the modulation starting in the flat region at 2.0 nm, we find that the GF exhibits an equal weight between anti-phase and in-phase behaviors. We classify this situation as "half-half". When considering the peak positions of GF distributions, we observe that $2 > |\mathrm{GF}| \gtrsim 1$ for the conductance plateau, *i.e.* GFs are smaller as compared to the previous two cases, for which $|\mathrm{GF}| \gtrsim 2$. We note that there are statistical variations in the GF histograms as there are many possible junction configurations for the molecule. By taking a large set of modulation measurements without data selection, GFs at different initial displacements demonstrate statistically the conductance features of ZnPC2, revealing the exponential conductance decay, increase and plateau.

DFT and transport analysis

To understand the underlying transport mechanisms of the observed conductance changes during stretching, theoretical modeling has been performed for the geometries of ZnPC2 single-molecule junctions during the unfolding process, and for the related electronic transport in terms of the phase-coherent and elastic Lan-

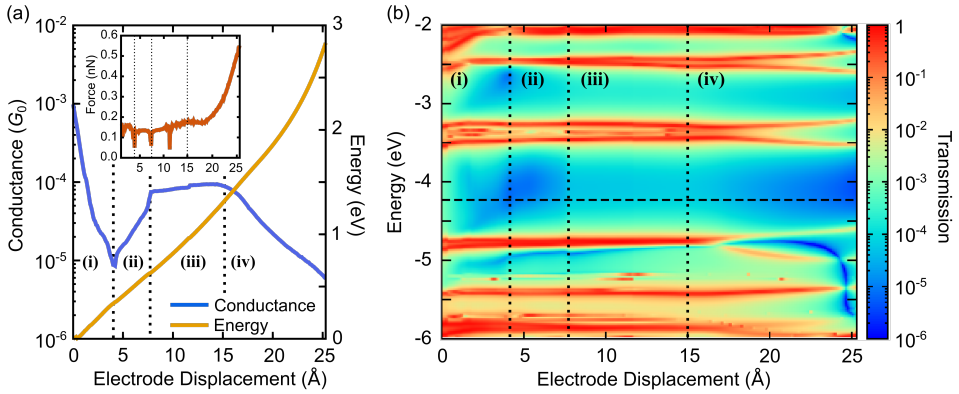

Figure 4.5: (a) Conductance at room temperature $T = 300$ K and total DFT energy as a function of electrode displacement. The inset shows the tension force during the unfolding process, obtained by taking the derivative of the total DFT energy with respect to d. (b) Contour plot of transmission as a function of energy and electrode displacement. The horizontal dashed line shows the Fermi energy $E_F = -4.24$ eV. In both panels vertical dotted lines separate the four characteristic conductance regions: (i) Exponential decrease, (ii) exponential increase, (iii) plateau, and (iv) exponential decrease.

dauer scattering theory [26]. The conductance at room temperature is computed *via* the linear response expression

$$G = G_0 \int_{-\infty}^{\infty} dE \left(-\frac{\partial f(E)}{\partial E} \right) \tau(E). \tag{4.1}$$

Here, $\tau(E)$ is the energy-dependent transmission function and $f(E)$ is the Fermi distribution. The transmission $\tau(E)$ is determined *ab initio*, *i.e.*, without free parameters, by combining DFT with the nonequilibrium Green's function formalism, as explained in detail in Ref. [27].

The junction geometries are obtained from DFT through energy optimization as follows: First, the isolated ZnPC2 molecule, see Fig. 4.1a, is optimized in the gas phase. Second, the molecule is placed between two Au_{20} clusters, see Fig. 4.4, forming the extended central cluster of the molecular junction [27]. In this step, the molecule and the four gold atoms of the two innermost layers of each gold pyramid closest to the molecule are optimized, while other gold atoms in the two outermost layers of each metal cluster are kept fixed in a face-centered cubic bulk lattice configuration, see Fig. 4.4a. Third, the stretching process is started from the initial geometry and continued until the point of rupture. During the process the two outermost fixed layers of the gold clusters are separated in steps of 0.1 Å, and the geometry is optimized in each step in the same way, as described before under point two. This yields the simulated junction geometries that are visualized *via* snapshots at various electrode displacements, d, in Fig. 4.4.

The transmission $\tau(E)$ and the conductance G are calculated at $T = 300$ K from Eq. (4.1), using the electronic structure of the obtained geometries. Figure 4.5 characterizes electrical and mechanical properties of the simulated ZnPC2 single-molecule junction. Figure 4.5a visualizes the conductance G and the total

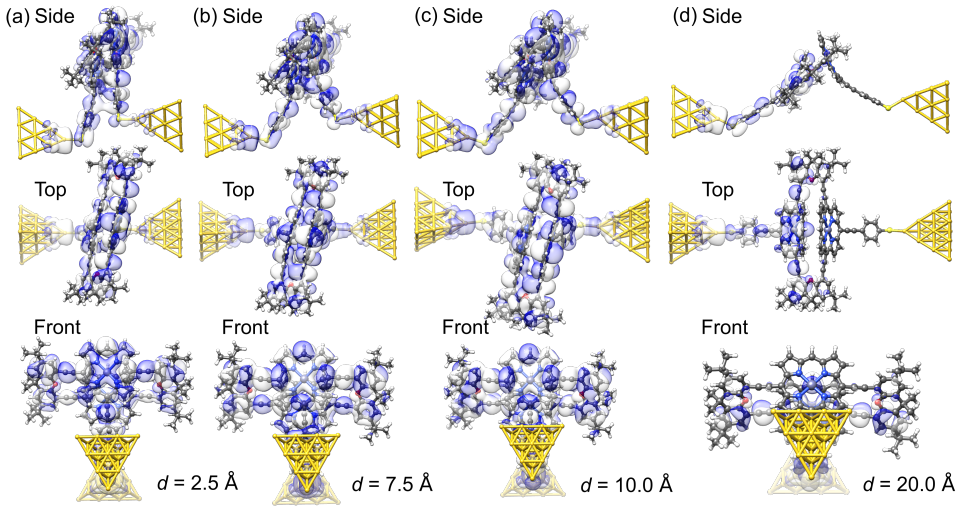

Figure 4.6: (a)-(d),Wave function of the most transparent left-incoming transmission eigenchannel in side, top and front views for several electrode displacements, d, as indicated below the panels. The transmission eigenchannels are evaluated at the Fermi energy E_F. Panel (a) belongs to a geometry in region (i), (b) to region (ii), (c) to region (iii), and (d) to region (iv), as defined in Fig. 4.5

DFT energy of the system in dependence on the electrode displacement d. The conductance behavior can be divided into four regions: (i) exponential decrease from $G = 10^{-3}G_0$ to $6 \cdot 10^{-6}G_0$ for $d = 0$ Å to 4.4 Å, (ii) exponential increase from $6 \cdot 10^{-6}G_0$ to $8 \cdot 10^{-5}G_0$, by more than one order of magnitude, for 4.4 Å to 7.8 Å, (iii) plateau from $8 \cdot 10^{-5}G_0$ to $9 \cdot 10^{-5}G_0$ for 7.8 Å to 15 Å, (iv) exponential decrease from $9 \cdot 10^{-5}G_0$ to $5 \cdot 10^{-6}G_0$ for 15 Å to the point of rupture at 25.3 Å. Throughout the unfolding process the total energy rises rather monotonically. Taking the derivative of the total DFT energy with respect to the electrode displacement yields the tensile force, shown in the inset of Fig. 4.5a. The force is rather constant in regions (i)-(iii), while it increases sharply towards the end in region (iv), where the molecule is far away from of its equilibrium position. At the point of rupture, the force amounts to 0.57 nN.

For a better understanding of electronic transport, the energy- and distance-dependent transmission of the molecular junction is displayed in Fig. 4.5b. Vertical dashed lines separate the four conductance regions, introduced in Fig. 4.5a. Transmission values are relatively high for small electrode displacements around $d = 0$ Å at all energies inside the HOMO-LUMO gap, which is located between the horizontal red resonance lines of frontier orbitals at about -4.7 eV and -3.8 eV. Interestingly, a blue area of suppressed transmission is visible that extends between regions (i) and (ii), while the transmission is comparatively high at all energies inside the HOMO-LUMO gap in region (iii). The transmission finally decays in region (iv). This plot shows that the overall conductance behavior of Fig. 4.5a is expected to be robust, since even for other choices of Fermi energies or level alignments, *i.e.*, a constant shift of molecular and metallic levels, a similar conductance behavior is

expected. Remarkably, the theoretically predicted behavior with the four regions (i)-(iv) agrees well with the experimental observations reported in Fig. 4.2 of a fast conductance decay, revival, plateau and final decay.

Let us now relate the different conductance regions of Fig. 4.5 to the complex atomic motion inside the junction, shown in Fig. 4.4. For this purpose, additional information is provided in SI. 2.1 [1], including transmissions as a function of energy at different electrode displacements d, corresponding to vertical cuts in Fig. 4.5b, and an analysis of various intramolecular distance changes. For a clear visualization, a video in Ref. [1] establishes the link between the simultaneous evolution of conductance and junction geometry.

The fast initial conductance decay in region (i) arises from the separation of *para*-ethynylbenzenethiol linkers, see in particular the side views in Fig. 4.4a-c. This is accompanied by the decay of an energy independent background of the transmission inside the HOMO-LUMO gap, resulting from the removal of the direct through-space tunneling pathway.

Region (ii) is characterized by a constant position of transmission resonances, but a changing energetic broadening, while *para*-ethynybenzenethiols are separated further, see Fig. 4.4c,d. Region (ii) starts and ends with fast molecular reconfigurations, which lead to the dips in the tensile force in Fig. 4.5a at $d = 4.4$ Å and 7.8 Å. They originate from sudden rotations of the left and right anchoring benzene rings, which consecutively align favorably to the Au electrodes and to the porphyrin's π-system, as the bending of the porphyrin-acetylene-benzene connections increase, see SI.2.3 [1]. The rising conductance is attributed to a combined effect of an increasing through-bond coupling within each deck and the strengthened through-space coupling between the decks. They result on the one hand from the alignment of the anchoring benzenes with the porphyrins and on the other hand from the simultaneous compression of the two porphyrins on the opposed side of the mechanically fixing xanthene bridges, while the porphyrin-porphyrin interaction area remains basically constant. Essentially, these mechanically induced reconfigurations make the conduction pathway through the porphyrin pincers the dominant one.

In region (iii), where energy-dependent transmission curves remain basically unchanged inside the HOMO-LUMO gap for different displacements d, porphyrins are peeled off. While the upper part of the porphyrin double decker is compressed, c.f. the side views in Fig. 4.4d-f, the lower part separates. These competing effects of separation and compression nearly compensate, leading to a weak growth of the conductance. A dip in the tensile force arises in the middle of region (iii) at $d = 11.7$ Å, when the porphyrins align rather abruptly to the pulling direction, while they are initially canted, see the top views in Fig. 4.4a-e in comparison to Fig. 4.4f. At this point, a small kink is visible in the conductance in Fig. 4.5a.

In region (iv) all such canting and twists inside the molecule are removed due to tensile stress. Further separation of the electrodes decreases the region of porphyrin-porphyrin overlap, leading to the collapse of the conduction pathway within the porphyrin pincers and a fast overall decay of the conductance. Ultimately, the pulling apart of the porphyrins is limited by the rigid xanthene bridges.

Figure 4.6 visualizes the wave functions of the left-incoming transmission eigenchannels with the highest transmission at the Fermi energy for selected electrode separations d within each of the four regions (i)-(iv) [28, 29]. It is found that the wave functions of the eigenchannels in regions (i)-(iii), see Fig. 4.6a-c, spread over the whole molecule. Remarkably the direct tunneling from one *para*-ethynylbenzenethiol to the other is directly visible in region (i), see Fig. 4.6a. In region (iv) at $d = 20$ Å, see Fig. 4.6d, the weight of the wave function quickly decays along the molecule instead. Here, a high weight is found only on the porphyrin deck that is directly connected through a sulfur anchor to the left electrode, while the weight on the right molecular deck is substantially reduced. Since the π-orbitals of the porphyrins at $d = 20$ Å stand nearly perpendicular to each other and the wave function is no longer efficiently propagated through the xanthene linkers, the intramolecular electronic coupling is low.

The above transmission calculations elucidate the four conductance regions as a result of changes in intramolecular conduction pathways. Initially the charge takes a shortcut *via* through-space tunneling, while it later on takes a much longer pathway through the porphyrin pincers, leading to the characteristic behavior of the conductance upturn upon electrode separation, plateau region and subsequent final decay. Two regions in the unfolding process are particularly interesting. One is related to the fast rotation of benzene rings and the other to the unfolding of porphyrin pincers, pivoting at the central xanthene bridges. The former suggests that by including components such as acetylenes in a molecular design, rotations under mechanical bending can act as a switch for through-space and through-bond conduction. The latter indicates that by changing the pivot points of a co-facial π-system with anchoring on the same sides, intramolecular interactions can be controlled, thereby serving as a starting point for more complex folded molecular origami designs.

4.3. Conclusion

We have presented a combined experimental and theoretical study of charge transport through a cofacial porphyrin cyclophane as a model compound representing molecular pincers. We have experimentally demonstrated a large mechanosensitivity of this molecule, exhibiting a conductance upturn by two orders of magnitude upon increasing the distance between the electrodes in individual breaking traces. While separating the electrodes, four regions have been identified: (i) exponentially decreasing conductance, followed by a region of (ii) exponentially increasing conductance, a region of (iii) constant conductance, and a region showing (iv) exponential decay before the contacts finally break. Compellingly, DFT-based calculations reproduce the four characteristic conductance regions during the molecular rearrangement in the molecular junctions and rationalize the effects by atomistic simulations. We find that the conduction pathways are mechanically controlled as a result of a subtle balance between through-bond and through-space contributions in intramolecular transport. The study highlights the precise unfolding that metal electrodes can evoke on single molecules, bringing the molecular system out of its natural equilibrium. We are currently interested in tuning the extent of the differ-

ent transport contributions by improved molecular designs. In particular, increased mechanosensitivity and analyte-mechanosensitive model compounds are crucial for a better understanding of molecular unfolding processes, paving the way to new sensing concepts relevant to biological systems or bioanalytics.

4.4. Appendix

4.4.1. ZnPC2 fast-breaking measurement at 250 mV

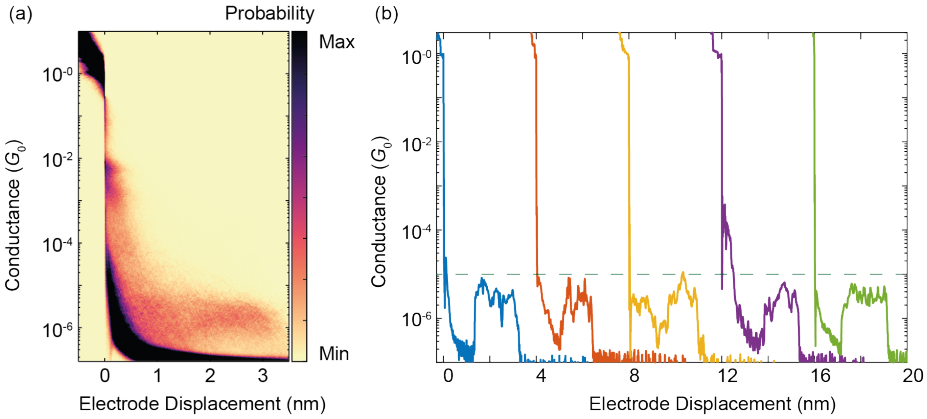

Figure 4.7: (a) Additional ZnPC2 fast-breaking measurements of sample 2 at an applied bias voltage of 250 mV. 10000 conductance traces are compiled in the 2D conductance vs. displacement density plot. (b)Five example traces, showing large conductance variations of up to two orders of magnitude. The horizontal dashed line at $G = 10^{-5}G_0$ is a guide to the eye.

Additional fast-breaking measurements of ZnPC2 on a different sample are displayed in Fig. 4.7 for a bias voltage of 250 mV. In Fig. 4.7a the two-dimensional (2D) conductance-displacement histogram is plotted without any data selection. A conductance plateau located at around $2 \times 10^{-6}G_0$ is observed, consistent with the 2D histogram shown in Fig. 4.2 of the main text. Individual fast-breaking traces are plotted in Figs. 4.7b. These example traces feature a conductance minimum of around an electrode displacement of 1.5 nm, then an increase of conductance followed by a plateau region that lasts about 1 nm, before the conductance decays exponentially and the contact finally breaks. These findings are consistent with the results reported in the main text.

4.4.2. Additional 2HPC2 fast-breaking measurements

Fast-breaking measurements at bias voltages of 250 mV and 100 mV are displayed in Figs. 4.8 and 4.9, respectively. Similar to ZnPC2, the 2D conductance-displacement histograms of 2HPC2 show a molecular conductance value of around $2 \times 10^{-6}G_0$, see Figs. 4.8a and 4.9a. Individual fast-breaking traces are plotted in Figs. 4.8b and 4.9b. These traces feature the same behavior as ZnPC2, following the four conductance regimes, described by the DFT calculations. The similarities suggest that the transport mechanism is the same for 2HPC2 and ZnPC2. Thus the metal center has little effect on the electronic transport in the cofacial porphyrin, consistent with previous studies [30].

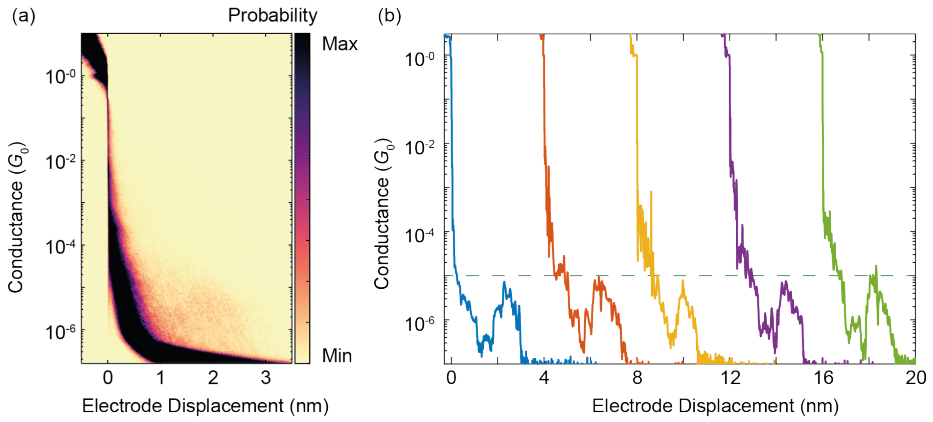

Figure 4.8: (a) Fast-breaking measurements on 2HPC2, measured at a bias voltage of 250 mV. The 2D conductance histogram consists of 7589 conductance-displacement traces. (b) Five example traces, offset by hand by 4 nm, showing the large conductance variations, which are similar to the case of ZnPC2.

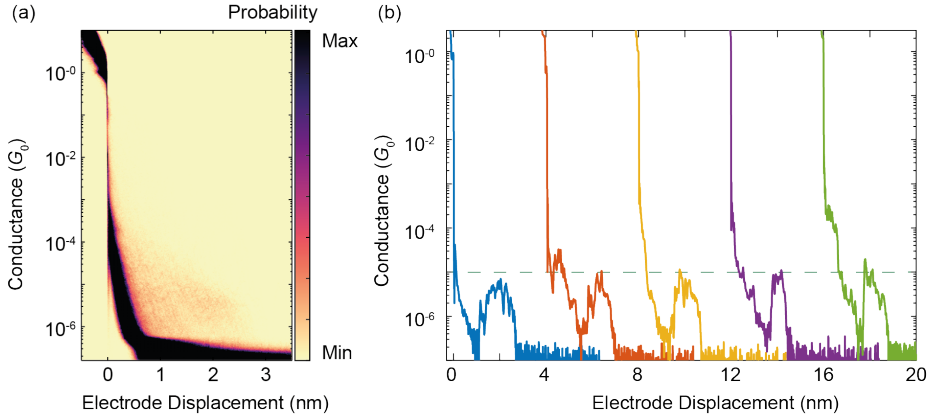

Figure 4.9: Same as Fig. 4.8 but at a bias voltage of 100 mV. The density plot now comprises 9225 conductance-distance traces.

References

(1) Hsu, C.-W.; Schosser, W. M.; Zwick, P.; Dulić, D.; Mayor, M.; Pauly, F.; van der Zant, H. S. J. *Chemical Science* **2022**, *13*, 8017–8024.

(2) Li, Y.; Haworth, N. L.; Xiang, L.; Ciampi, S.; Coote, M. L.; Tao, N. *Journal of the American Chemical Society* **2017**, *139*, 14699–14706.

(3) Camarasa-Gómez, M.; Hernangómez-Pérez, D.; Inkpen, M. S.; Lovat, G.; Fung, E. D.; Roy, X.; Venkataraman, L.; Evers, F. *Nano Letters* **2020**, *20*, 6381–6386.

(4) Wu, C.; Bates, D.; Sangtarash, S.; Ferri, N.; Thomas, A.; Higgins, S. J.; Robertson, C. M.; Nichols, R. J.; Sadeghi, H.; Vezzoli, A. *Nano Letters* **2020**, *20*, 7980–7986.

(5) Ferri, N.; Algethami, N.; Vezzoli, A.; Sangtarash, S.; McLaughlin, M.; Sadeghi, H.; Lambert, C. J.; Nichols, R. J.; Higgins, S. J. *Angewandte Chemie - International Edition* **2019**, *58*, 16583–16589.

(6) Kobayashi, S.; Kaneko, S.; Kiguchi, M.; Tsukagoshi, K.; Nishino, T. *Journal of Physical Chemistry Letters* **2020**, *11*, 6712–6717.

(7) Quek, S. Y.; Kamenetska, M.; Steigerwald, M. L.; Choi, H. J.; Louie, S. G.; Hybertsen, M. S.; Neaton, J. B.; Venkataraman, L. *Nature Nanotechnology* **2009**, *4*, 230–234.

(8) Meisner, J. S.; Kamenetska, M.; Krikorian, M.; Steigerwald, M. L.; Venkataraman, L.; Nuckolls, C. *Nano Letters* **2011**, *11*, 1575–1579.

(9) Su, T. A.; Li, H.; Zhang, V.; Neupane, M.; Batra, A.; Klausen, R. S.; Kumar, B.; Steigerwald, M. L.; Venkataraman, L.; Nuckolls, C. *Journal of the American Chemical Society* **2015**, *137*, 12400–12405.

(10) Su, T. A.; Li, H.; Steigerwald, M. L.; Venkataraman, L.; Nuckolls, C. *Nature Chemistry* **2015**, *7*, 215–220.

(11) Frisenda, R.; Janssen, V. A. E. C.; Grozema, F. C.; van der Zant, H. S. J.; Renaud, N. *Nature Chemistry* **2016**, *8*, 1099–1104.

(12) Frisenda, R.; Harzmann, G. D.; Celis Gil, J. A.; Thijssen, J. M.; Mayor, M.; van der Zant, H. S. J. *Nano Letters* **2016**, *16*, 4733–4737.

(13) Stefani, D.; Weiland, K. J.; Skripnik, M.; Hsu, C.; Perrin, M. L.; Mayor, M.; Pauly, F.; van der Zant, H. S. J. *Nano Letters* **2018**, *18*, 5981–5988.

(14) Reznikova, K.; Hsu, C.; Schosser, W. M.; Gallego, A.; Beltako, K.; Pauly, F.; van der Zant, H. S. J.; Mayor, M. *Journal of the American Chemical Society* **2021**, *143*, 13944–13951.

(15) Li, J.; Shen, P.; Zhen, S.; Tang, C.; Ye, Y.; Zhou, D.; Hong, W.; Zhao, Z.; Tang, B. Z. *Nature Communications* **2021**, *12*, 167.

(16) Franco, I.; George, C. B.; Solomon, G. C.; Schatz, G. C.; Ratner, M. A. *Journal of the American Chemical Society* **2011**, *133*, 2242–2249.

(17) Stefani, D.; Perrin, M.; Gutiérrez-Cerón, C.; Aragonès, A. C.; Labra-Muñoz, J.; Carrasco, R. D.; Matsushita, Y.; Futera, Z.; Labuta, J.; Ngo, T. H.; Ariga, K.; Díez-Pérez, I.; van der Zant, H. S. J.; Dulić, D.; Hill, J. P. *ChemistrySelect* **2018**, *3*, 6473–6478.

(18) Nejedlý, J.; Šámal, M.; Rybáček, J.; Sánchez, I. G.; Houska, V.; Warzecha, T.; Vacek, J.; Sieger, L.; Buděšínský, M.; Bednárová, L.; Fiedler, P.; Císařová, I.; Starý, I.; Stará, I. G. *Journal of Organic Chemistry* **2020**, *85*, 248–276.

(19) Schosser, W. M.; Hsu, C.-W.; Zwick, P.; Beltako, K.; Dulić, D.; Mayor, M.; van der Zant, H. S. J.; Pauly, F. *Nanoscale* **2022**, *14*, 984–992.

(20) Zwick, P.; Weiland, K. J.; Malinčík, J.; Stefani, D.; Häussinger, D.; van der Zant, H. S. J.; Dulić, D.; Mayor, M. *The Journal of Organic Chemistry* **2020**, *85*, 118–128.

(21) Zwick, P.; Dulić, D.; van der Zant, H. S. J.; Mayor, M. *Nanoscale* **2021**, *13*, 15500–15525.

(22) Cabosart, D.; El Abbassi, M.; Stefani, D.; Frisenda, R.; Calame, M.; van der Zant, H. S. J.; Perrin, M. L. *Applied Physics Letters* **2019**, *114*, 143102.

(23) Martin, C. A.; Ding, D.; van der Zant, H. S. J.; van Ruitenbeek, J. M. *New Journal of Physics* **2008**, *10*, 065008.

(24) Martin, C. A.; Smit, R. H. M.; Egmond, R. V.; van der Zant, H. S. J.; van Ruitenbeek, J. M. *Review of Scientific Instruments* **2011**, *82*, 053907.

(25) Shen, P.; Huang, M.; Qian, J.; Li, J.; Ding, S.; Zhou, X.-S.; Xu, B.; Zhao, Z.; Tang, B. Z. *Angewandte Chemie International Edition* **2020**, *59*, 4581–4588.

(26) Cuevas, J. C.; Scheer, E., *Molecular Electronics: An Introduction to Theory and Experiment*, 2nd Edition; World Scientific: Singapore, 2017.

(27) Pauly, F.; Viljas, J. K.; Huniar, U.; Häfner, M.; Wohlthat, S.; Bürkle, M.; Cuevas, J. C.; Schön, G. *New Journal of Physics* **2008**, *10*, 125019.

(28) Paulsson, M.; Brandbyge, M. *Physical Review B* **2007**, *76*, 115117.

(29) Bürkle, M.; Viljas, J. K.; Vonlanthen, D.; Mishchenko, A.; Schön, G.; Mayor, M.; Wandlowski, T.; Pauly, F. *Physical Review B* **2012**, *85*, 075417.

(30) El Abbassi, M.; Zwick, P.; Rates, A.; Stefani, D.; Prescimone, A.; Mayor, M.; van der Zant, H. S. J.; Dulić, D. *Chem. Sci.* **2019**, *10*, 8299–8305.

5

Single-molecule thermoelectricity: Thermocurrent spectroscopy and entropy

Thermoelectricity is the conversion between voltage and temperature differences in a system. While it has been a technologically important concept to integrate in electronics; fundamentally, it is the relationship between electronic and thermal properties of a material. Theoretical studies suggest that single-molecule devices can host strong thermoelectric effects. This advantage is achieved via different molecular designs for an optimized tunnel coupling or a sharp transmission close to the Fermi energy, etc. Recently, we have created single-molecule thermoelectric quantum dot devices, where valuable information such as the Seebeck coefficient and thermoelectric power factor are directly obtained from their strong thermoelectric responses. We further show that fundamental physical quantities, such entropy changes, can be determined in the thermoelectric quantum dot devices. The rich physics in thermoelectric quantum dot devices and their technological implications open another research direction for nanoscale devices.

Parts of this chapter have been published in *Nature Nanotechnology* **2021**, *16*, 426–430 [1] and *Nano Letters* **2021**, *21*, 9715–9719 [2].

5.1. Introduction

Intense theoretical scrutiny predicts that the interplay between the spin, vibrational and electronic degrees of freedom should result in high thermoelectric energy harvesting efficiencies [3–7], in ways strongly linked to the molecular design. These theoretical predictions are difficult to test experimentally: they require accurate measurements of minute thermocurrent signals (fA - pA) in a single molecule with a tunable electrochemical potential [8, 9], simultaneous control of temperature, T, bias and gate voltages, V_{sd} and V_{G}, and thermal bias, $\Delta\tilde{T}$, in a parameter space wide enough to access both the linear and non-linear regimes. Due to these difficulties, previous schemes typically relied on sequential measurements of the conductance G and the Seebeck coefficient S [4, 8–11] which can cause large errors in evaluating the power factor S^2G, because of molecular reconfiguration and drift in the measurement electronics [9, 12]. Methods that provide G and S simultaneously fundamentally prevent the possibility to apply gate and bias voltages [13]. Full maps, where electric- and thermocurrents are thoroughly separated were thus unavailable before the method described in this chapter.

We overcome these challenges by employing a measurement scheme that allows us to simultaneously record the complete maps of bias, V_{sd}, and gate voltage, V_{G}, -dependent conductance, G, and thermocurrent, $\tilde{I}_{\mathrm{th}}$, of a single-molecule junction. The device consists of a gold-molecule-gold junction created by electromigration [14] of gold nano contacts (Chap. 2), where DC and AC currents can be applied and measured simultaneously (Fig. 5.1a). To detect the thermocurrent, micro-heaters are fabricated in direct thermal contact with the source and drain leads. This device scheme grants us not only the full mapping of the thermoelectric properties of a single-molecule quantum dot but also offers a new spectroscopic approach to investigate fundamental physical concepts such as entropy changes between two electronic states.

5.2. Complete mapping of the thermoelectric properties of a single molecule

In this section, we first show our device capability to simultaneously determine the electric and thermoelectric properties of a single-molecule junction. We use the $[Gd(tpy\text{-}SH)_2(NCS)_3]$ complex (hereafter Gd-tpy), synthesized by our collaborator J. Le Roy and L. Bogani. The theoretical modeling was performed by J. K. Sowa and E. M. Gauger. The details of the synthesis and theoretical calculation can be found in the supplementary information of the published Letter [1].

5.2.1. Results & Discussions

The thermoelectric single-molecule junction is achieved by using the Gd-tpy complex. The choice of molecule is because the Gd(III) metal affords a high-spin magnetic center (term symbol $^8S_{7/2}$, spin $\Sigma = 7/2$), where the spin degrees of freedom can be studied in conjunction with charge and vibrational ones. Gd-tpy molecules were deposited by immersing the sample in a solution after electromigration fol-

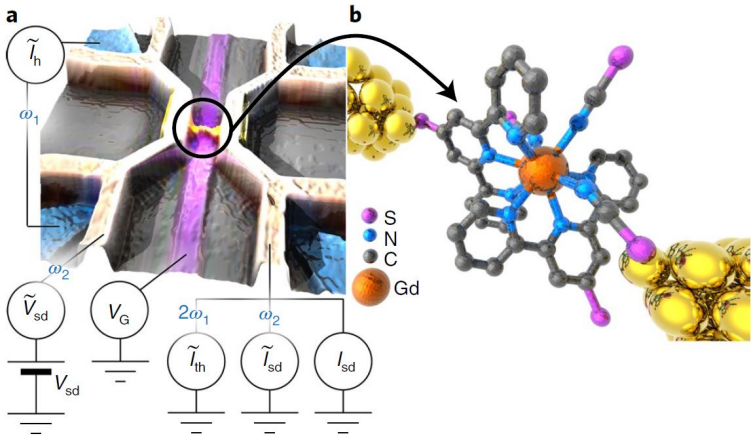

Figure 5.1: The experimental system. (a) False-colour scanning electron microscopy image of the typical experimental junctions. The schematic circuit diagram indicates which the terminals are used to apply a gate voltage V_G, a DC bias voltage V_{sd}, an AC bias voltage $\tilde{V}_{sd}(\omega_2)$ and an AC heater current $\tilde{I}_h(\omega_1)$, and which terminals are used to measure a DC current I_{sd}, an AC current $\tilde{I}_{sd}(\omega_2)$ and a thermocurrent $\tilde{I}_{th}(2\omega_1)$. (b) The structure of the Gd-tpy molecule bridging the electrodes, as obtained by X-Ray crystallography, depicted here as coupled asymmetrically to the two gold leads.

lowed by self-breaking (see Sec. 2.2 for details). A possible junction geometry with asymmetric coupling is depicted in Fig. 5.1b. The DC current I_{sd}, G and $\tilde{I}_{th}$ are measured simultaneously by using a lock-in double-modulation technique in which the response to $\Delta\tilde{T}$ can be decoupled from the response to the electrical biases, so that the pure $\tilde{I}_{th}$ is accessible for any V_{sd}, V_G (Fig. 5.1a and Chap. 2). These values together with the value of $\Delta\tilde{T}$ (obtained from calibration measurements and fitting [1]) are then used to extract the Seebeck coefficient $S = -\tilde{V}_{th}/\Delta\tilde{T} = -\tilde{I}_{th}/\Delta\tilde{T}/(\tilde{I}_{sd}/\tilde{V}_{sd})$ for any V_{sd} and V_G. The power factor $S^2G = (\tilde{I}_{th}/\Delta\tilde{T})^2/(\tilde{I}_{sd}/\tilde{V}_{sd})$ is a direct measure of the heat-to-energy conversion efficiency in single-molecule devices [15].

Figure 5.2 shows the maps of G, I_{sd} and $\tilde{I}_{th}$ as a function of V_{sd} and V_G at a cryostat temperature of $T_{base} = 2$ K. I_{sd} reveals two regions with suppressed current (due to Coulomb blockade) separated by an hourglass shaped region of sequential electron tunneling (Fig. 5.2a). This is a well-known and often-observed phenomenon in molecular junctions. In all of our junctions only one charge transition could be observed within the experimentally accessible V_G range. In the G map we can furthermore identify a line, starting from the left edge of the sequential tunneling region at an energy of ~ 2 meV, that runs parallel to the right edge and corresponds to an excited molecular state (Fig. 5.2b). A similar excitation has been found in three other junctions [1]. Furthermore, we observe that these excited state lines do not split, shift, or change in width when an 8 T magnetic field is applied, as it would be expected for a spin(-multiplet) excitation of the Gd(III) center or spin excitations of the ligand orbital. On the contrary, a handful of low-frequency intra-molecular vibrational modes match this energy scale [1], and we thus attribute the observed lines not to spin but to vibrational excitations.

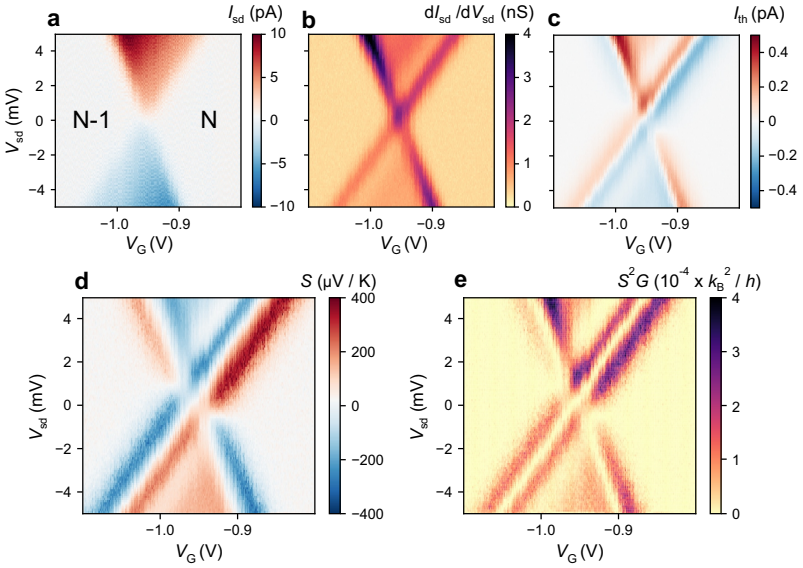

Figure 5.2: Maps of electronic and thermoelectric properties. (a) DC current, (b) differential conductance and (c) thermocurrent of a Gd-tpy junction measured simultaneously as a function of bias and back gate voltage. The data in (b) and (c) is used to calculate the (d) Seebeck coefficient and (e) power factor as a function of bias and back gate voltage. N and $\mathrm{N}-1$ denote the number of electrons on the molecule in the respective Coulomb blockade regions.

$\tilde{I}_{\mathrm{th}}$ displays nodes at the Coulomb diamond edges, when the chemical potential of the molecular level μ_{mol} is equal to that of the source or drain (μ_{L} and μ_{R}, with $V_{\mathrm{sd}} = (\mu_{\mathrm{R}} - \mu_{\mathrm{L}})/e$)) and reaches maximum values close to these energies (red/blue lines in Fig. 5.2c). The sign of the signal indicates whether the thermocurrent is carried by electrons ($I_{\mathrm{th}} > 0$) or holes ($I_{\mathrm{th}} < 0$). The ratio of the thermocurrent signals close to the Coulomb diamond edge with positive and negative slopes is used to estimate the temperatures of the contacts in direct vicinity of the single molecule.

To gain more insight into our data, a full rate equation theoretical modeling is performed. From a fit to our data ($\mathrm{RE}^{\mathrm{full}}$ approach, see SI. 2 [1]) $\Delta\tilde{T} = 0.8$ K with $T_{\mathrm{R}} = 2.7$ K, $T_{\mathrm{L}} = 3.5$ K are found, *i.e.*, T_{R} increases by 0.7 K. Inside the SET region we observe a non-zero value of thermocurrent (0.1 pA for $|V_{\mathrm{sd}}| > 2$ mV), which is solely carried by the excited state (the AC thermoelectric response is mostly sensitive to the part of the transmission function within about $k_{\mathrm{B}}T_{\mathrm{L}}$ around μ_{L}). This is fundamentally different from I_{sd}, where the total current includes contributions by the ground and the excited states. Importantly, we note a negative-positive asymmetry of I_{th} vs V_{G} at points where I_{th} changes sign. This asymmetry can be clearly observed in the zero-bias trace in Fig. 5.3c, where $|I_{\mathrm{th,min}}/I_{\mathrm{th,max}}| = 1.4 \pm 0.2$ is found. The origin of this asymmetry is a change in spin entropy of the molecule upon adding an extra electron to it, as will be discussed below and in the next

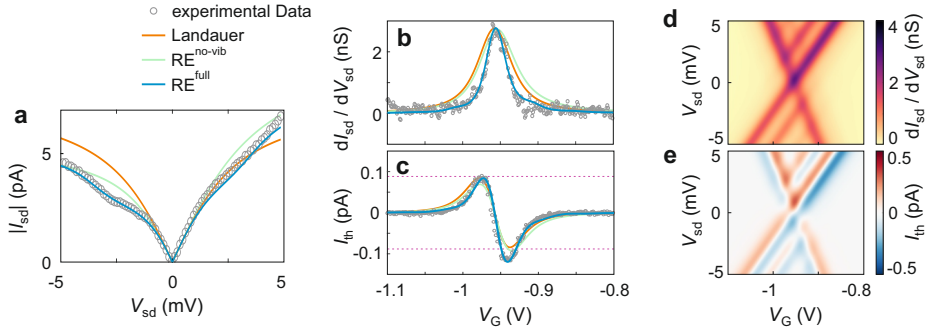

Figure 5.3: Comparison to theoretical model. (a) $I_{\mathrm{sd}} - V_{\mathrm{sd}}$ curve on resonance at $V_{\mathrm{G}} = -0.96$ V, (b) gate dependent zero-bias differential conductance and (c) thermocurrent extracted from Fig. 5.2. The grey circles show the experimental data, the solid lines show fits using a single-level Landauer approach (orange), a rate equation approach including spin entropy (green), and a rate equation approach including spin entropy and a vibrational mode (blue). The purple, dotted line indicates $I_{\mathrm{th,max}}$. (d) Calculated differential conductance and (e) thermocurrent as a function of bias and gate voltage using the rate equation approach including spin entropy and a vibrational mode, and the parameters extracted from the fit in (a).

section.

We can now extract the Seebeck coefficient S, *i.e.*, the magnitude of the induced thermoelectric voltage in response to the temperature difference $\Delta\tilde{T} = 0.8$ K across the single molecule, and the associated power factor S^2G (Fig. 5.2d,e). S changes sign when the conditions $\mu_{\mathrm{mol}} = \mu_{\mathrm{L}}$ or $\mu_{\mathrm{mol}} = \mu_{\mathrm{R}}$ are met, like $\tilde{I}_{\mathrm{th}}$, and reaches a maximum of $414\ \mu\mathrm{V/K}$ at $V_{\mathrm{sd}} = 3.4$ mV and $V_{\mathrm{G}} = -0.86$ V. An overall maximum of $S^2G = 3.6 \times 10^{-4} k_{\mathrm{B}}^2/h$ is found, where the maximum thermal response coefficient $L = \tilde{I}_{\mathrm{th}}/\Delta\tilde{T} = 0.6$ pA/K is also recorded, at $V_{\mathrm{sd}} = 4.9$ mV and $V_{\mathrm{G}} = -0.99$ V. At zero bias voltage, S^2G reaches a maximum $1.0 \times 10^{-4} k_{\mathrm{B}}^2/h$.

These data offer valuable insight into the processes at play within the molecular junction. Having access to the full V_{G} and V_{sd} dependent maps of I_{sd}, G and $\tilde{I}_{\mathrm{th}}$ of the single molecule, universal models ($\mathrm{RE}^{\mathrm{full}}$[16], $\mathrm{RE}^{\mathrm{no-vib}}$, Landauer, see below and SI. 2 [1]) are applied to reproduce $I_{\mathrm{sd}}(V_{\mathrm{sd}})$, $G(V_{\mathrm{G}})$ and $\tilde{I}_{\mathrm{th}}(V_{\mathrm{G}})$ simultaneously. To this end, the I_{sd}-V_{sd} characteristics at resonance ($V_{\mathrm{G}} = -0.96$ V) in Fig. 5.3a and the gate-dependent differential conductance and thermocurrent data ($V_{\mathrm{sd}} = 0$) show excellent agreement only with a rate-equation approach ($\mathrm{RE}^{\mathrm{full}}$), where the observed excited state is assumed of vibrational character (as suggested by the lack of any magnetic field response) and the electronic degeneracies of the states are included. Conversely, neither the Landauer nor a rate-equation approach that ignores the vibrational excitation ($\mathrm{RE}^{\mathrm{no-vib}}$) are able to reproduce the data. Here, the most important discrepancy between theory and experiment is the lack of negative-positive asymmetry in the Landauer model as observed in the experimental thermocurrent (Fig. 5.3c). The Landauer approach fails to explain this asymmetry, relying exclusively on ground-state transitions, and neglecting degeneracies and electron-electron interactions. It is found that asymmetric molecule-lead coupling (as is found in all measured samples) is by itself insufficient to reproduce the asym-

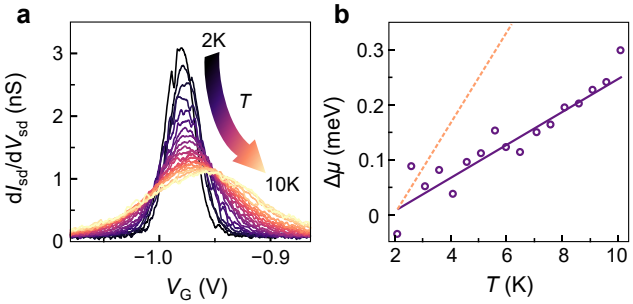

Figure 5.4: Temperature dependence of the differential conductance. (a) $\mathrm{d}I_{\mathrm{sd}}/\mathrm{d}V_{\mathrm{sd}}$ as a function of V_{G} for different temperatures. (b) Conductance peak position as a function of temperature extracted from (a). The purple line shows a fit to the data assuming a change of entropy of $\Delta\mathcal{S}_{N-1\to N} = k_{\mathrm{B}}\ln(2)$. The sign of $\Delta\mathcal{S}_{N-1\to N}$ is such that for more negative gate voltages (to the left of the Coulomb peak) an empty orbital, and for less negative gate voltages (to the right of the Coulomb peak) a single occupied orbital is available for transport. The orange dotted line shows a fit assuming a change of entropy of $\Delta\mathcal{S}_{N-1\to N} = k_{\mathrm{B}}\ln(14) - k_{\mathrm{B}}\ln(2)$.

5

metry in the thermocurrent. Rather, the key ingredient required to model this asymmetry is the degeneracy, *i.e.* the spin entropies, of the charge states involved in the sequential tunneling process (SI. 13 [1]) as well as the electron-electron interactions. For I_{th}, the current-limiting step is the electron transfer to and from the 'hot' contact. Depending on the value of V_{G}, the electron transfer at the 'hot' interface corresponds either to a $N-1 \to N$ or to a $N \to N-1$ transition. As demonstrated below, the $N-1$ state is two-fold degenerate, the latter transition is therefore more likely than the former. This leads to the observed asymmetry of I_{th} which can thus also be present in the case of symmetric molecule-lead coupling.

The rate-equation model $\mathrm{RE}^{\mathrm{full}}$ further yields excellent agreement with the thermocurrent experimental data for $T_R = 2.7$ K and $T_L = 3.5$ K, and these temperatures allow reproducing the full conductance and thermocurrent maps (Fig. 5.3d,e). The maximum calculated power factors of $0.57 \times 10^{-4} k_{\mathrm{B}}^2/h$ at zero bias and $4.3 \times 10^{-4} k_{\mathrm{B}}^2/h$ for $V_{\mathrm{sd}} = 4.9$ mV and $V_{\mathrm{G}} = -0.84$ V, agree well with the $1.0 \times 10^{-4} k_{\mathrm{B}}^2/h$ and $3.6 \times 10^{-4} k_{\mathrm{B}}^2/h$ values found experimentally.

We infer that the origin of the asymmetry of I_{th} vs V_{G} (which is captured by the $\mathrm{RE}^{\mathrm{full}}$ model) stems from the difference in the degeneracies, d_N and d_{N-1}, of the N and $N-1$ states [12, 17]. This difference in degeneracy can only arise from spin entropy [18–20]. A singlet to doublet transition is necessary for the fitting, when going from $N-1$ ($d_{N-1} = 2$) to N ($d_N = 1$) electrons. The spin entropy is given by $\mathcal{S}_N = k_{\mathrm{B}}\ln(d_N)$, the resulting change is $\Delta\mathcal{S} = \mathcal{S}_{N-1} - \mathcal{S}_N = k_{\mathrm{B}}\ln(2)$. As $\mathcal{S}_N$ contributes to the total energy of the molecule, a shift of the effective electrochemical potential μ_{mol} should occur with T:[21, 22]

$$\frac{\partial\mu}{\partial T} = \frac{1}{2}\Delta\mathcal{S}_{N-1\to N}\,. \tag{5.1}$$

The conductance peak shifts with increasing T (Fig. 5.4a) by a quantity $\Delta V_{\mathrm{G_{peak}}}(T) =$

$\Delta\mu_{\mathrm{mol}}\alpha$, that is connected to the capacitive couplings to the leads (C_{L}, C_{R}) and to the gate (C_{G}) by a proportionality factor $\alpha = (C_L+C_R+C_G)/C_G$. μ_{mol}, extracted by fitting the conductance peaks to a single-level model [3], indeed shows a linear increase with T, with slope a of $\frac{1}{2}k_{\mathrm{B}}\ln 2$ (Fig. 5.4b). This observation agrees perfectly with what is predicted for a singlet-to-doublet transition.

These findings provide details about the charging process of Gd-tpy: the spin-ground state of the neutral molecule is governed by the f-orbitals of the Gd(III) center, with ${}^8\mathrm{S}_{7/2}$ and spin $\Sigma = 7/2$. If the addition or removal of the charge involved an f-orbital electron of the Gd center, an entropy change of $\Delta\mathcal{S}_{N-1\to N} = k_{\mathrm{B}}\ln(14) - k_{\mathrm{B}}\ln(2)$ (or $\Delta\mathcal{S}_{N\to N+1} = k_{\mathrm{B}}\ln(2) - k_{\mathrm{B}}\ln(14)$) would be expected, i.e, 3 times higher than the observed value (Fig. 5.4b). This indicates that the transport electron is localised on the ligands more than on the metal center and that 4f electrons play a minor role (see SI. 9.1 and 14 [1]). Furthermore, if the exchange coupling between the ligand electron and Gd was higher than higher than $k_{\mathrm{B}}T$, a reduction in entropy change to $\Delta\mathcal{S}_{N\to N+1} = 0$ would be expected, contrary to the experimental findings.

These results demonstrate how spin entropy determines the single-molecule thermoelectric properties. Furthermore, the Seebeck coefficient obtained here, $414\ \mu\mathrm{V/K}$, is more than ten times higher than typical values found for conductive single molecule devices[4, 13, 23] and close to the value found for insulating devices[24]. This illustrates that high values of S can be achieved by creating sharp features in the transmission spectrum of the junction (which in our case is achieved by weak tunnel coupling to the leads) and by bringing the Fermi energy of the leads into the vicinity of these sharp features by electrostatic gating or doping of the molecule. We nonetheless note here that weak molecule-lead coupling results in low electric conductance and thus reduced power factors S^2G. This leaves ample room for further improvement: the power factors found in this study are four orders of magnitude smaller than the theoretical maximum of $\approx 0.46 \times k_{\mathrm{B}}^2/h$ (for a single non-interacting level)[9]. Much higher values are expected by achieving symmetric coupling and by improving the coupling strengths, so that $\Gamma \sim k_{\mathrm{B}}T$ and S^2G is not limited by low conductance values. Furthermore, our work indicates that molecular magnets with high changes of orbital or spin entropy upon charging can boost the efficiency of thermoelectric junctions: highly degenerate states offer multiple channels for charge transport which boosts G without altering S. In addition, spin-entropy effects will shift the maximum conductance (Fig. 5.4a) which leads to an increased overlap between the maxima in $S(V_{\mathrm{G}})$ and $G(V_{\mathrm{G}})$ and thus an enhancement of S^2G.

Nevertheless, we can use the experimental S^2G to estimate the thermoelectric figure of merit $ZT = S^2GT/(\kappa_{\mathrm{el}} + \kappa_{\mathrm{ph}})$. Our molecular junction operates in a regime where $k_BT < \hbar\omega$ with ω being the lowest frequency vibrational mode (see SI. 9.2 [1]). Therefore – and unlike for room temperature devices[25] – we disregard κ_{ph}, the phononic contribution to the thermal conductance. κ_{el} is then estimated by a rate equation approach that includes both spin-degeneracy and vibrational coupling (SI. 10 and 11 [1]) and we find a $ZT \approx 0.7$ at zero bias. Our experiments further demonstrate a significantly more efficient thermoelectric heat-

to-energy conversion at $T = 2$ K than at higher T, and highlight the need for a better theoretical understanding of the processes in play at cryogenic conditions.

5.2.2. Conclusion

This work reveals that full thermocurrent spectroscopy is possible and can be used to directly extract important thermoelectric properties and probe single-molecule ground and excited states. It further suggests methods to maximise thermoelectric efficiency by molecular design, in ways that are not immediately available in inorganic quantum-dots, *e.g.* by employing the symmetry-produced degeneracies of fullerenes [26, 27]. The possibility of extracting the spin entropy of a molecular junction opens the path to a plethora of effects, including magneto-cooling effects of Gd-based molecular compounds [28], spin-crossover complexes [29] or ground-state spin-blockade systems such as polyoxometalates [30].

The broad application of the thermocurrent spectroscopy is highlighted in later sections of this dissertation. In Sec. 5.3, we will further discuss a new approach to extract the entropy changes directly from the thermocurrent asymmetry. Furthermore, our measurement protocol would allow us to study how thermoelectric properties are influenced by Kondo correlations in single-molecule junctions [31], which will be discussed in Chap. 6.

5.3. Controlling the entropy of a single-molecule junction

The thermodynamic concept of entropy is key to the understanding of many chemical processes, including electron transfer reactions [32]. Spontaneous change only occurs when entropy increases and the universe becomes more disordered. While the statistical interpretation of entropy first given by Boltzmann connects entropy as a thermodynamic state function to the number of microstates available to the system, this connection is generally not quantifiable – macroscopic systems, containing Avogadro's numbers ($\sim 10^{23}$) of molecules, simply have too many configurations for the individual to be tractable. At the single-molecule level, however, electron transfer reactions lead to significant changes in configurational entropy related to the electronic structure that can be quantified due to the relatively small number of states of the system [33]. The ability to directly measure entropy of individual molecules – without the need of a priori knowledge of its electronic structure – can thus provide insights into their non-trivial quantum states, such as (high-)spin ground states [30, 34], Kondo states [35–37], Majorana modes [38], and non-abelian anyons [39, 40], and shed light on the discriminating role of entropy in driving electron transfer rates.

Recent experiments have demonstrated the potential for direct entropy measurements in mesoscopic quantum systems [1, 18, 22, 41]. These studies connect macroscopic observable quantities, including electrical current and charge, to microscopic configuration entropy in the form of spin-degeneracy. Here, we scale this approach down to the single-molecule level and determine the redox-dependent entropy of an individual nitronyl nitroxide radical (shown in Fig. 5.5a) directly from its thermoelectric conductance. The entropy measurements indicate that the neutral molecule holds an unpaired electron and is therefore in a doublet ground state, while the ground state of the reduced molecule is a singlet with all electrons paired. However, by applying a magnetic field to the reduced molecule, a low-lying triplet excitation state is revealed which was not observed in conventional charge transport measurements.

5.3.1. Results & Discussions

To measure the entropy difference ΔS between the neutral (with N electrons) and the reduced (with $N+1$ electrons) free radical molecule directly from its thermoelectric response, a necessary theoretical framework first needs to be developed. To this end, our collaborators, E. Pyurbeeva and J. Mol, derived an expression for the conductance $G = \partial I/\partial V_{sd}$ (where V_{sd} is the bias voltage across the molecule) from rate equations (see SI. 1 [2]) that is consistent with that derived for sequential electron tunneling through a quantum dot [21]. Moreover, an expression for the thermoelectric conductance $L = \partial I/\partial \Delta T$ is derived (where ΔT is the temperature difference across the molecule) which takes a similar form:

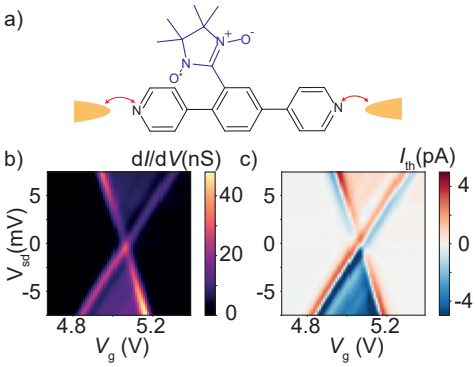

Figure 5.5: (a) Sketch of the molecule (a free radical, green, located at the a nitronyl nitroxide side group, blue, which is connected to a backbone, black) connected to the source and drain lead. The red arrows indicate electron tunneling on and off the molecule. (b) Bias and gate voltage dependent differential conductance and (c) thermocurrent of a single NNR molecule junction.

$$G \propto \frac{1}{T}\left[1 - f(\varepsilon)\right] f(\varepsilon - T\Delta S), \tag{5.2}$$

$$L \propto \frac{\varepsilon}{T^2}\left[1 - f(\varepsilon)\right] f(\varepsilon - T\Delta S), \tag{5.3}$$

where f is the Fermi-Dirac distribution, ε the single-electron energy level with respect to the electrochemical potential of the electrodes, and T the equilibrium temperature of the system. Here, the free energy of formation $\Delta F = \varepsilon - T\Delta S$ can be associated with the isothermal electrode reaction as the driving force for electron transfer [42]. It is observed that, as a result, the conductance is maximum when $\varepsilon = T\Delta S/2$, as was experimentally demonstrated previously [1, 12]. More importantly, the thermoelectric response is asymmetric around $\varepsilon = 0$ and the degree of asymmetry scales directly with ΔS. In the remainder of this section, it is therefore appropriate to exploit this asymmetry as a direct measure for the entropy difference.

The conductance and thermoelectric response of the free radical are measured simultaneously by contacting it in an electromigrated break junction with integrated micro-heaters and gate electrodes using a double lock-in technique[1, 43], same as the method described in Chap. 2 and Sec. 5.2. Here, we use an organic radical molecule (nitronyl nitroxide radical), synthesized by D. Vogel and M. Mayor. It consists of a 1,4-bis(4-pyridyl)benzene backbone and a nitronyl nitroxide side group where an unpaired electron resides as shown in Fig. 5.5a. This makes it a single-spin system in its neutral state. Single-molecule junctions are formed by opening a nm-sized gap in a thin gold bridge using electromigration followed by self-breaking [43] and depositing of single molecules from solution after nano-gap formation. Figure 5.5b and c show the conductance and thermocurrent $L\Delta T$ (with $\Delta T = 600$ mK in all experiments) as a function of the applied bias (V_{sd}) and gate (V_{g})

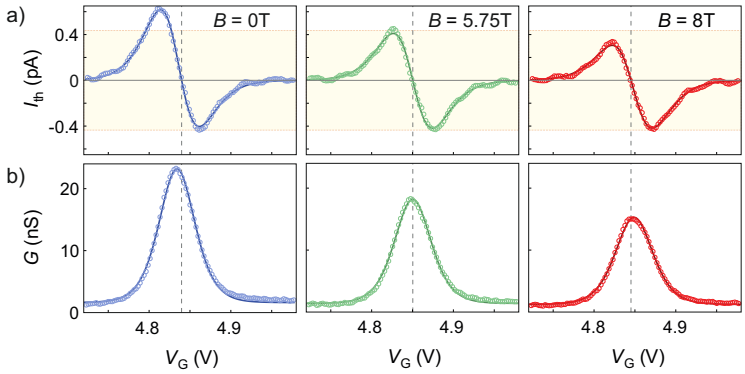

Figure 5.6: (a) Thermocurrent and (b) conductance at three different magnetic fields (Experimental data: open circles; theoretical fits using equations 1 and 2 (in the small temperature difference assumption): solid lines). The yellow shaded areas indicate the minimum thermocurrent $I_{\mathrm{th,min}}$. The vertical dotted lines indicate $I_{\mathrm{th}} = 0$.

voltage. We observed regions of low conductance (Coulomb-blocked, black in Fig. 5.5b), corresponding to the N and $N+1$ redox states of the free radical, separated by a region of sequential electron tunneling. Furthermore, lines inside the sequential tunneling regime running in parallel to the edges of the Coulomb diamond can be observed, which we attribute to vibrational excitations of the molecule [1, 9, 44–46]. The thermocurrent (Fig. 5.5c) is zero at the Coulomb diamond edges and reaches minimum/maximum values close to these edges (blue and red lines), similar to our previous findings on Gd-tpy complexes [1].

In the following, we will focus on the gate-dependent conductance and thermocurrent traces at zero bias ($V_{\mathrm{sd}} = 0$), as shown in Fig. 5.6. We find a peak in conductance around a gate value of 4.8 - 4.9 V, where an extra charge is continuously added and removed to/from the molecule leading to electron transfer from one side of the molecule to the other. For gate voltages $\gg 4.9$ V, $N+1$ charges reside on the molecule and it is in its reduced state. The gate-dependent thermocurrent changes sign around the position of the conductance peak and possesses a pronounced asymmetry between its maximum and minimum. As explained above, this asymmetry is a direct measure of the entropy difference between the redox states of the free radical. We further observe that the degree of asymmetry of the thermocurrent, as well as the shift of the conductance peak, vary when a magnetic field is applied (see Fig. 5.6). This is a clear indication that the entropy of the system can be controlled by a magnetic field. To quantify this entropy change ΔS as a function of magnetic field the zero-bias conductance and thermocurrent traces shown in Fig. 5.6 are fitted to Eqs 5.2 and 5.3 (see solid lines in Fig. 5.6) using $\varepsilon = \varepsilon_0 - \alpha V_{\mathrm{g}}$, where α is the lever-arm given by the capacitance between the free radical and the electrodes [3, 21, 47]. While the combination α/T can be treated as a single fitting parameter corresponding to the width of the conductance peak, by finding the lever-arm separately, the temperature is extracted from the fits as equal to 3.6 K, which agrees with experimental thermometry.

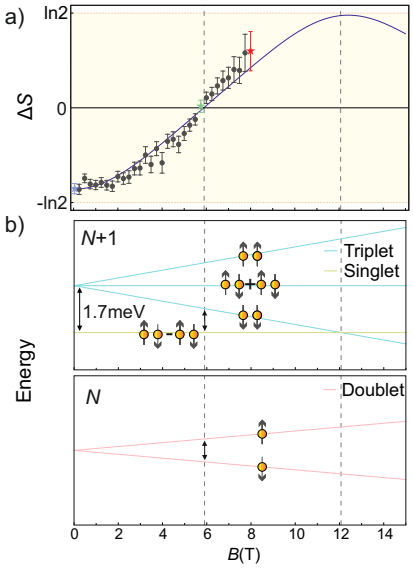

Figure 5.7: (a) Entropy change of the molecule obtained from fitting equation 1 and 2 to the experimental data (in the small temperature difference assumption) as a function of magnetic field (points). Solid line represents the best fit of the entropy change values to the difference in Gibbs entropy between the charge states in the doublet → singlet+triplet model. (b) Energy level structure for the molecule in its neutral state (N electrons) and reduced state (N+1 electrons) as a function of magnetic field, for the values of Δ_{ST} and g-factor from fit in (a). It can be seen that the point of zero entropy change (dashed line at approximately 6T) approximately corresponds to the same energy splitting between the two doublet states and the two lower-lying states of the $N + 1$ charge states, meaning that the transition effectively occurs between two identical doublet states (vertical arrows). The yellow spheres (and corresponding arrows) illustrate the spin states of the free radical (on the nitronyl nitroxide unit) and the extra added electron on the backbone (in the reduced case, N+1).

Figure 5.7a shows the resulting entropy difference between the N and $N + 1$ redox states as a function of magnetic field determined by fitting to Eqn. 5.3. At zero magnetic field ΔS approaches a value of $-k_B \ln 2$, where k_B is the Boltzmann constant. Because the Gibbs entropy is equal to $-k_B \sum p \ln p$, where p is the occupation probability of each microstate of the system, it can be concluded that the N charge state has 2 accessible microstates with equal occupation probabilities, while the $N + 1$ charge state has one. This agrees with the free radical ground state having an unpaired electron in its ground state, and thus being a spin-doublet, and the reduced state having all electrons paired, being a singlet.

When the magnetic field is increased, an increase of ΔS is observed, which reaches a value of zero and changes sign at $B \sim 6$ T. With the application of the magnetic field, the degeneracy of the doublet (N electrons) ground state is lifted. As the field – and with it the Zeeman splitting – is increased, the probability of occupation of the bottom energy level of the doublet begins to dominate. This can explain the increase of ΔS at low magnetic fields, however this is not consistent with the subsequent change of sign of ΔS at approximately 6 T. The magnetic-field-

dependent entropy therefore points to a low-lying triplet state of the reduced free radical where the entropy associated to the partial population in the $N+1$ singlet and triplet states can exceed the entropy of the N doublet population. These results are confirmed by comparing them to previously employed methods [1, 48] based on the analysis of the difference in the energy levels corresponding to zero thermocurrent point and the conductance peak, where a similar entropy difference dependence was obtained, to the thermocurrent asymmetry analysis (see SI. 2 [2]).

To determine the singlet-triplet splitting Δ_{ST} in the $N+1$ redox state, the expected entropy difference for the doublet → singlet+triplet transition is determined, assuming a Gibbs distribution at the temperature found from the fits in each of the charge states, as a function of magnetic field, singlet-triplet splitting Δ_{ST} and the g-factor. It is used to fit the experimentally obtained ΔS dependence on magnetic field with Δ_{ST} and the g-factor as fitting parameters (the fitting result is shown in Fig. 5.7). This approach yields a g-factor of 2.7, deviating from the value of 2 for a free electron. Such deviations have been found before in nano-scale junctions and have been attributed to orbital contributions [49, 50]. Furthermore, a singlet-triplet splitting $\Delta_{ST} = 1.7 \pm 0.1$ meV is extracted. This low energy can be explained by assuming that the extra electron (when reducing the molecule) is added to the molecular back-bone rather than to the nitronyl nitroxide side group of the molecule. Δ_{ST} would then correspond to the exchange interaction between the two free electrons (on the side group and the backbone), similar to the value of 4.65 meV found experimentally in similar free radical all-organic systems [51].

The small singlet-triplet splitting, and the resulting entropy contribution of the non-zero $N+1$ triplet population, is the reason for the deviation of ΔS from $-k_B \ln 2$ at zero magnetic field. Moreover, at $B \sim 6$ T the splitting between the $|T_+\rangle$ triplet state and the singlet is equal to the splitting between the doublet states (see Fig. 5.7b), and the Gibbs entropy of the two redox states are approximately equal, $-k_B \left[p_\uparrow \ln p_\uparrow + p_\downarrow \ln p_\downarrow\right] \approx -k_B \left[p_S \ln p_S + p_{T_+} \ln p_{T_+}\right]$, (where ps are the occupation probablities of ↑ – the spin up doublet state, ↓ – spin down doublet state, S – the singlet state and T_+ – the lowest-lying triplet state), as the population in $|T_0\rangle$ and $|T_-\rangle$ are negligible, where T_0 and T_- are the middle- and high-energy triplet states respectively. When $\Delta S = 0$, an anti-symmetric thermoelectric response ($I_{\mathrm{th}}(\varepsilon) = -I_{\mathrm{th}}(-\varepsilon)$) is observed, as there is no difference in free energy between the two redox states. ΔS is expected to reach its positive maximum at $B \sim 12$ T, outside of our experimental range, when the $|T_+\rangle$ and $|S\rangle$ states cross and the $N+1$ entropy is maximum $S_{N+1} \approx k_B \ln 2$ while S_N tends to zero. As the magnetic field increases further, only the lowest-lying levels of both charge states will be occupied and the entropy difference will approach zero in the infinite field limit.

5.3.2. Conclusion

This analysis demonstrates that thermocurrent spectroscopy is a sensitive tool to access the fundamental thermodynamic properties of nanoscale devices. It has several advantages over previously employed methods, because, unlike *e.g.* the approach taken in Ref. [22, 41] our method does not rely on charge state measurements and therefore does not require the fabrication of complicated charge

sensors and is applicable to any devices on which thermoelectric measurements can be performed. Furthermore, it does not require measurements of the device at multiple temperatures to find the entropy, as was the case with one of the previous approaches [1]. We applied the method to a single-molecule device and found that the direct measurement of the entropy difference with the change of the redox state reveals the presence of a low-lying triplet state in the molecule and allows us to quantify the exchange coupling between the free radical and the extra added electron. This serves as further evidence for the potential of practical applications of entropy measurement methods.

References

(1) Gehring, P.; Sowa, J. K.; Hsu, C.; de Bruijckere, J.; van der Star, M.; Le Roy, J. J.; Bogani, L.; Gauger, E. M.; van der Zant, H. S. J. *Nature Nanotechnology* **2021**, *16*, 426–430.

(2) Pyurbeeva, E.; Hsu, C.; Vogel, D.; Wegeberg, C.; Mayor, M.; van der Zant, H. S. J.; Mol, J. A.; Gehring, P. *Nano Letters* **2021**, *21*, 9715–9719.

(3) Gehring, P.; Thijssen, J. M.; van der Zant, H. S. J. *Nat. Rev. Phys.* **2019**, *1*, 381–396.

(4) Park, S.; Kang, H.; Yoon, H. J. *J. Mater. Chem. A* **2019**, *7*, 14419–14446.

(5) Koch, J.; von Oppen, F.; Oreg, Y.; Sela, E. *Phys. Rev. B* **2004**, *70*, 195107.

(6) Lambert, C. J.; Sadeghi, H.; Al-Galiby, Q. H. *C. R. Phys.* **2016**, *17*, 1084–1095.

(7) Murphy, P.; Mukerjee, S.; Moore, J. *Phys. Rev. B* **2008**, *78*, 161406.

(8) Kim, Y.; Jeong, W.; Kim, K.; Lee, W.; Reddy, P. *Nat. Nanotechnol.* **2014**, *9*, 881–885.

(9) Gehring, P.; Harzheim, A.; Spièce, J.; Sheng, Y.; Rogers, G.; Evangeli, C.; Mishra, A.; Robinson, B. J.; Porfyrakis, K.; Warner, J. H.; Kolosov, O. V.; Briggs, G. A. D.; Mol, J. A. *Nano Lett.* **2017**, *17*, 7055–7061.

(10) Widawsky, J. R.; Darancet, P.; Neaton, J. B.; Venkataraman, L. *Nano Lett.* **2012**, *12*, 354–358.

(11) Park, S.; Kang, S.; Yoon, H. J. *ACS Cent. Sci.* **2019**, *5*, 1975–1982.

(12) Harzheim, A.; Sowa, J. K.; Swett, J. L.; Briggs, G. A. D.; Mol, J. A.; Gehring, P. *Phys. Rev. Research* **2020**, *2*, 013140.

(13) Rincón-García, L.; Evangeli, C.; Rubio-Bollinger, G.; Agraït, N. *Chem. Soc. Rev.* **2016**, *45*, 4285–4306.

(14) O'Neill, K.; Osorio, E. A.; van der Zant, H. S. J. *Applied Physics Letters* **2007**, *90*, 2005–2008.

(15) Behnia, K., *Fundamentals of thermoelectricity*; Oxford University Press: 2019.

(16) Sowa, J. K.; Mol, J. A.; Briggs, G. A. D.; Gauger, E. M. *J. Chem. Phys.* **2018**, *149*, 154112.

(17) Josefsson, M.; Svilans, A.; Burke, A. M.; Hoffmann, E. A.; Fahlvik, S.; Thelander, C.; Leijnse, M.; Linke, H. *Nat. Nanotechnol.* **2018**, *13*, 920–924.

(18) Kleeorin, Y.; Thierschmann, H.; Buhmann, H.; Georges, A.; Molenkamp, L. W.; Meir, Y. *Nat. Commun.* **2019**, *10*, 5801.

(19) Viola, G.; Das, S.; Grosfeld, E.; Stern, A. *Phys. Rev. Lett.* **2012**, *109*, 146801.

(20) Mazal, Y.; Meir, Y.; Dubi, Y. *Phys. Rev. B* **2019**, *99*, 075433.

(21) Beenakker, C. *Phys. Rev. B* **1991**, *44*, 1646.

(22) Hartman, N.; Olsen, C.; Lüscher, S.; Samani, M.; Fallahi, S.; Gardner, G. C.; Manfra, M.; Folk, J. *Nat. Phys.* **2018**, *14*, 1083–1086.

(23) Cui, L.; Miao, R.; Jiang, C.; Meyhofer, E.; Reddy, P. *J. Chem. Phys.* **2017**, *146*, 092201.

(24) Garner, M. H.; Li, H.; Chen, Y.; Su, T. A.; Shangguan, Z.; Paley, D. W.; Liu, T.; Ng, F.; Li, H.; Xiao, S.; Nuckolls, C.; Venkataraman, L.; Solomon, G. C. *Nature* **2018**, *558*, 416–419.

(25) Cui, L.; Hur, S.; Akbar, Z. A.; Klöckner, J. C.; Jeong, W.; Pauly, F.; Jang, S.-Y.; Reddy, P.; Meyhofer, E. *Nature* **2019**, *572*, 628–633.

(26) Ke, S.-H.; Baranger, H. U.; Yang, W. *Phys. Rev. Lett.* **2003**, *91*, 116803.

(27) Sowa, J. K.; Mol, J. A.; Gauger, E. M. *J. Phys. Chem. C* **2019**, *123*, 4103–4108.

(28) Evangelisti, M.; Roubeau, O.; Palacios, E.; Camón, A.; Hooper, T. N.; Brechin, E. K.; Alonso, J. J. *Angew. Chem. Int. Ed.* **2011**, *50*, 6606–6609.

(29) Dugay, J.; Aarts, M.; Giménez-Marqués, M.; Kozlova, T.; Zandbergen, H. W.; Coronado, E.; van der Zant, H. S. J. *Nano Lett.* **2017**, *17*, 186–193.

(30) De Bruijckere, J.; Gehring, P.; Palacios-Corella, M.; Clemente-León, M.; Coronado, E.; Paaske, J.; Hedegård, P.; van der Zant, H. S. J. *Phys. Rev. Lett.* **2019**, *122*, 197701.

(31) Costi, T. A. *Phys. Rev. B* **2019**, *100*, 161106.

(32) Nitzan, A., *Chemical dynamics in condensed phases : relaxation, transfer and reactions in condensed molecular systems*; Oxford University Press: 2013, pp 21–35.

(33) Seifert, U. *Reports Prog. Phys.* **2012**, *75*, 126001.

(34) Coronado, E. *Nature Reviews Materials* **2020**, *5*, 87–104.

(35) Andrei, N.; Destri, C. *Phys. Rev. Lett.* **1984**, *52*, 364–367.

(36) Hiraoka, R.; Minamitani, E.; Arafune, R.; Tsukahara, N.; Watanabe, S.; Kawai, M.; Takagi, N. *Nature Communications* **2017**, *8*, 16012.

(37) Guo, X.; Zhu, Q.; Zhou, L.; Yu, W.; Lu, W.; Liang, W. *Nature Communications* **2021**, *12*, 1566.

(38) Smirnov, S. *Phys. Rev. B* **2015**, *92*, 195312.

(39) Ben-Shach, G.; Laumann, C. R.; Neder, I.; Yacoby, A.; Halperin, B. I. *Phys. Rev. Lett.* **2013**, *110*, 106805.

(40) Nakamura, J.; Liang, S.; Gardner, G. C.; Manfra, M. J. *Nat. Phys.* **2020**, *16*, 931–936.

(41) Sela, E.; Oreg, Y.; Plugge, S.; Hartman, N.; Lüscher, S.; Folk, J. *Phys. Rev. Lett.* **2019**, *123*, 147702.

(42) Marcus, R. A. *The Journal of Chemical Physics* **1965**, *43*, 679–701.

(43) Gehring, P.; van der Star, M.; Evangeli, C.; Le Roy, J. J.; Bogani, L.; Kolosov, O. V.; van der Zant, H. S. J. *Appl. Phys. Lett.* **2019**, *115*, 073103.

(44) Park, H.; Park, J.; Lim, A. K. L.; Anderson, E. H.; Alivisatos, A. P.; McEuen, P. L. *Nature* **2000**, *407*, 57–60.

(45) Leturcq, R.; Stampfer, C.; Inderbitzin, K.; Durrer, L.; Hierold, C.; Mariani, E.; Schultz, M. G.; von Oppen, F.; Ensslin, K. *Nature Physics* **2009**, *5*, 327–331.

(46) Gehring, P.; Sowa, J. K.; Cremers, J.; Wu, Q.; Sadeghi, H.; Sheng, Y.; Warner, J. H.; Lambert, C. J.; Briggs, G. A. D.; Mol, J. A. *ACS Nano* **2017**, *11*, PMID: 28423272, 5325–5331.

(47) Zimbovskaya, N. a., *Transport Properties of Molecular Junctions*; Springer Tracts in Modern Physics, Vol. 254; Springer New York: New York, NY, 2013, pp 1–275.

(48) Pyurbeeva, E.; Mol, J. A. *Entropy* **2021**, *23*, 640.

(49) Liu, L.; Yang, K.; Jiang, Y.; Song, B.; Xiao, W.; Song, S.; Du, S.; Ouyang, M.; Hofer, W. A.; Castro Neto, A. H.; Gao, H.-J. *Phys. Rev. Lett.* **2015**, *114*, 126601.

(50) Winkler, G. W.; Varjas, D.; Skolasinski, R.; Soluyanov, A. A.; Troyer, M.; Wimmer, M. *Phys. Rev. Lett.* **2017**, *119*, 037701.

(51) Gaudenzi, R.; de Bruijckere, J.; Reta, D.; Moreira, I. d. P. R.; Rovira, C.; Veciana, J.; van der Zant, H. S. J.; Burzurí, E. *ACS Nano* **2017**, *11*, 5879–5883.

6

Single-molecule thermoelectricity: Magnetic-field universality of the Kondo effect

Probing the universal low-temperature magnetic-field scaling of Kondo--correlated quantum dots via electrical conductance has been proved to be experimentally challenging. Here, we show how to probe this in nonlinear thermocurrent spectroscopy applied to a molecular quantum dot in the Kondo regime. Our results demonstrate that the bias-dependent thermocurrent is a sensitive probe of universal Kondo physics, directly measures the splitting of the Kondo resonance in a magnetic field, and opens up possibilities for investigating nanosystems far from thermal and electrical equilibrium.

Parts of this chapter have been published in *Physical Review Letters*, **2022**, *128*, 147701 [1]. The theoretical modeling was carried out by T. A. Costi and the synthesis was performed by D. Vogel. The details of the calculation and synthesis can be found in the supplementary information of the publication.

6.1. Introduction

The Kondo effect, originally describing the anomalous increase with decreasing temperature in the resistivity of nonmagnetic metals containing a small concentration of magnetic impurities [2–4], is now a ubiquitous phenomenon in physics, forming the starting point for understanding the Mott transition [5], heavy fermions [6], and transport through correlated nanostructures, such as quantum dots [7, 8], molecules [9] and adatoms on surfaces [10]. In the so-called "QCD Kondo effect" [11], it also constitutes one of the first known examples of asymptotic freedom [12, 13], a property of the strong interaction in particle physics.

A key feature of the Kondo effect is its universality [14–16]. For example, the temperature dependence of the linear conductance $G(T)$ of a spin-$1/2$ quantum dot is described by a unique universal scaling function $G(T)/G(0) = g(T/T_K)$ of T/T_K, where T is the temperature and T_K is the Kondo scale, and is used as a hallmark for establishing a spin-$1/2$ Kondo effect in quantum dot systems [17]. The same holds for exotic realizations of the Kondo effect [18–21], with each having its own characteristic set of universal scaling functions. Thus, universality in Kondo systems provides hallmarks for identifying the particular Kondo effect in a given experiment [19, 20, 22].

In this Letter, we address another aspect of universality of Kondo-correlated quantum dots, namely the universal magnetic-field scaling in the low-temperature ($T \ll T_K$) Fermi-liquid regime of quantum dots. While our interest is in the thermocurrent, we first specify what we mean by low-temperature magnetic-field scaling in the context of the more familiar differential conductance $G(T, V_{sd}) = dI/dV_{sd}$ (derivative of the electrical current with respect to source-drain voltage). Specifically, for the asymmetrically coupled quantum dot device investigated in this Letter [Fig. 6.1(b)], described within the Anderson impurity model [Fig. 6.1(c)], $G(T \ll T_K, V_{sd} \ll T_K)$ is given, for *arbitrary* magnetic fields B, within higher-order Fermi liquid theory [23–25] as,

$$\frac{dI}{dV_{sd}} \propto a_0 - c_T \left(\frac{\pi T}{T_K}\right)^2 - c\frac{V_{sd}}{T_K} - c_V \left(\frac{V_{sd}}{T_K}\right)^2, \tag{6.1}$$

with field-dependent coefficients a_0, c_T, c and c_V [1]. The low-temperature magnetic-field scaling that we refer to is reflected in the universal dependence of the curvature coefficients $c_V(B) \propto -\partial^2 G/\partial V_{sd}^2$ and $c_T(B) \propto -\partial^2 G/\partial T^2$ on B/T_K in the Kondo regime [23–25] [2]. Surprisingly, the exact dependence of c_V and c_T on magnetic field has only recently been calculated *via* a generalization of Nozières Fermi-liquid theory [26] to nonequilibrium and particle-hole asymmetric situations [23–25]. The results show that c_V and c_T are universal functions of magnetic field which change

[1] See Supplemental Material at [https://journals.aps.org/prl/abstract/10.1103/PhysRevLett.128.147701] for derivation of Eqs. (6.1) and (6.2), expressions for $a_0(B), c_T(B), c(B), c_V(B)$ and $s_0(B), S_1(B)$, evaluations, further experimental details, fitting procedures, synthesis and characterization, results at finite temperature and thermal bias.

[2] $a_0(B)$ and $c(B)$ in (6.1) depend strongly on particle-hole and/or lead coupling asymmetry and are nonuniversal functions of B/T_K.

sign at a universal crossover field $B = B_c$ describing the onset of the splitting of the Kondo resonance in dI/dV_{sd}, in agreement with predictions for B_c for the Kondo model [27]. Nevertheless, establishing this universality and the splitting of the Kondo resonance in dI/dV_{sd} is intrinsically difficult [28–31]. Yet, both serve as useful experimental hallmarks of the Kondo effect in quantum dots.

Here, we propose a different approach to address magnetic-field scaling in the strong-coupling Kondo regime of quantum dots by employing the recently developed thermocurrent spectroscopy [32]. We experimentally show that the thermocurrent, I_{th}, of a molecular quantum dot in the Kondo regime exhibits a clear feature as a function of magnetic field, in the form of a zero-bias ($V_{sd} = 0$) kink appearing for fields B larger than a certain value, which we denote by B_{th}. This behavior is explained within higher-order Fermi-liquid theory [23, 25] for $V_{sd} \ll T_K$, and an approximate nonequilibrium Green function approach [33] for $V_{sd} \gtrsim T_K$. Within the former, to leading order in V_{sd}, T and ΔT, where ΔT is the applied thermal-bias, it is found in the low-temperature strong-coupling regime $\Delta T \ll T \ll T_K$,

$$I_{th}(T, V_{sd}) = \gamma \frac{\pi^2 k_B^2}{3} T \Delta T [s_0(B) + s_1(B) V_{sd}], \tag{6.2}$$

with constant γ and coefficients $s_0(B)$ and $s_1(B)$ [1]. Remarkably, it is shown that, (i), $s_1(B)/s_1(0)$ and $c_V(B)/c_V(0)$ are described by essentially the same universal scaling function in the Kondo regime, showing that $\frac{dI_{th}}{dV_{sd}}\big|_{V_{sd}=0}$ [$\propto s_1(B)$] probes magnetic-field universality, and, (ii), B_{th} coincides with B_c, thus demonstrating that thermocurrent spectroscopy provides a new route to directly probe the splitting of the Kondo resonance [27] and extract the universal field $B_c = B_{th}$. Our findings are concisely summarized in the sketch in Fig. 6.1(a). We note, that in contrast to the zero-bias thermocurrent slope, the zero-bias thermocurrent, $I_{th}(T, V_{sd} = 0)$ [$\propto s_0(B)$], measured in Ref. [34] as a function of gate-voltage (V_g) and magnetic field and found to change sign at a certain field B_0, is nonuniversal [Fig. 6.4(a), Ref. [35] and SM.3.5.5 [1]]. Thus $I_{th}(T, V_{sd} = 0)$ does not provide a hallmark for the splitting of the Kondo resonance and cannot be used to extract B_c, in contrast to the thermocurrent spectroscopy proposed in this Letter.

6.2. Result & Discussion

The experiment is carried out on a molecular quantum dot consisting of an organic radical molecule (nitronyl nitroxide radical, NNR) made up of a backbone and a nitronyl-nitroxide side group where an unpaired electron resides as shown in Fig. 6.1(b). Such free radical molecules are model systems to study the spin-1/2 Kondo effect [Fig. 6.1(c)] [38–40]. Furthermore, their asymmetric structure and the pyridine anchoring sites allow us to achieve asymmetric and strong coupling between the source and drain leads and the molecule (quantified by couplings Γ_s and Γ_d, Fig 6.1(b)). We form a NNR-molecule quantum dot in the thermoelectric device shown in Fig. 6.1(d) by immersing electromigrated nanogaps in the molecular solution [41]. The thermoelectric device incorporates a local backgate and two micro-heaters in direct thermal contact with the source/drain leads [see Fig. 6.1(d)].

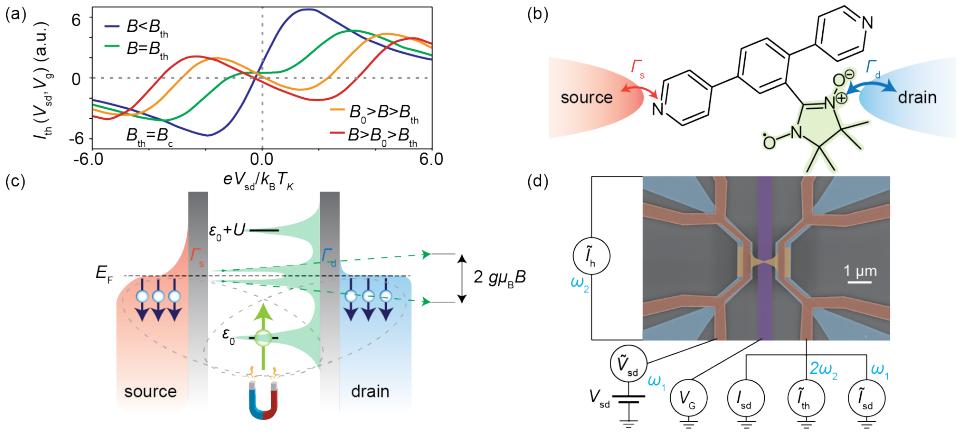

Figure 6.1: (a) Sketch of $I_{\rm th}$ vs $V_{\rm sd}$ in the Kondo regime for several B. $(\partial I_{\rm th}/\partial V_{\rm sd})|_{V_{\rm sd}=0}$ is a universal function of $B/T_{\rm K}$ and changes sign (kink) at a universal field $B = B_{\rm th} = B_{\rm c}$ [Fig. 6.4(a)], while $I_{\rm th}(V_{\rm sd} = 0)$ [34] changes sign at $B = B_0 > B_{\rm c}$ and is nonuniversal [Fig. 6.4(a), Ref. [35] and SM.3.5.5 [1]]. (b) Molecular junction of a NNR molecule anchored to source and drain leads. (c) Anderson model of (b) in a magnetic field B. A singly occupied level ε_0 with Coulomb repulsion U and gate voltage $V_{\rm g} = (\varepsilon_0+U/2)/\Gamma$ coupled to hot and cold source and drain leads with strength $\Gamma = \Gamma_{\rm s} + \Gamma_{\rm d}$ gives rise to a spin-1/2 Kondo effect for $V_{\rm g} \approx 0$ resulting in a Kondo resonance at the Fermi energy, $E_{\rm F}$. The field B splits the up and down levels at ε_0 by $g\mu_{\rm B}B$ and the Kondo resonance in ${\rm d}I/{\rm d}V_{\rm sd}$ by $2g\mu_{\rm B}B$ [36, 37] (for $g\mu_{\rm B}B \gg k_{\rm B}T_{\rm K}$). A thermal bias $\Delta T > 0$ causes a thermocurrent $I_{\rm th}$ to flow between source and drain, measured as described in (d). (d) False-coloured scanning electron microscopy image of the thermoelectric device. Bias and thermal voltages are generated by a DC+AC bias voltage source, $V_{\rm sd}+\tilde{V}_{\rm sd}(\omega_1)$, and a AC heater current source, $\tilde{I}_{\rm h}(\omega_2)$, on the hot left lead. The resulting DC, AC electrical currents and AC thermocurrent, $I_{\rm sd}$, $\tilde{I}_{\rm sd}(\omega_1)$ and $\tilde{I}_{\rm th}(2\omega_2)$, are measured simultaneously on the cold right lead.

Evidence for a Kondo effect is shown by the strong suppression of the zero-bias peak in the measured ${\rm d}I/{\rm d}V_{\rm sd}$, both as a function of increasing T [Figs. 6.2(a)-6.2(b)] and B [Figs. 6.2(c)-6.2(d)]. The T-dependence of the zero-bias peak height [Fig. 6.2(b)] is well described by the numerical renormalization group (NRG) conductance of a spin-1/2 Kondo model and yields $T_{\rm K} = 12.8$ K (SM.1.3 [1]). Based on the structure of the molecule, an asymmetric coupling is expected. Assuming, $\Gamma_{\rm d} \gg \Gamma_{\rm s}$, we find $\Gamma_{\rm s}/\Gamma_{\rm d} \approx 0.017$. An underscreened Kondo effect [19, 20], requiring a larger molecular spin ($S > 1/2$), is excluded, since such an effect results in a split Kondo resonance in ${\rm d}I/{\rm d}V_{\rm sd}$ starting already at zero field, which is not observed in Figs. 6.2(c)-6.2(d). Thus, a single-level Anderson model describing a $S = 1/2$ Kondo effect [Fig. 6.1(c)] is justified by the data. In the remainder of this Letter, the base temperature is kept at $T \approx 2$ K $\ll T_{\rm K}$ while the thermocurrent is measured for a small thermal bias $\Delta T \approx 0.6$ K $\ll T \ll T_{\rm K}$ so that we probe the strongly-coupled Kondo regime.

A closer look at the field dependence of ${\rm d}I/{\rm d}V_{\rm sd}$ in Figs. 6.2(c)-6.2(d), indicates that the expected splitting of the Kondo peak at $B_{\rm c} \approx 7.15$ T is not observed [3]. This is in part due to a large non-Kondo (field and temperature independent) contribution

[3] Estimated using $B_{\rm c} \approx 0.5 k_{\rm B}T_{\rm K}^{\rm HWHM}/g\mu_{\rm B} = 0.75 k_{\rm B}T_{\rm K}/g\mu_{\rm B}$ [23, 25, 27], with $T_{\rm K}^{\rm HWHM} \approx 1.5\ T_{\rm K}$ from SM.3.2 [1], and using $T_{\rm K}$ in Fig. 6.2(b).

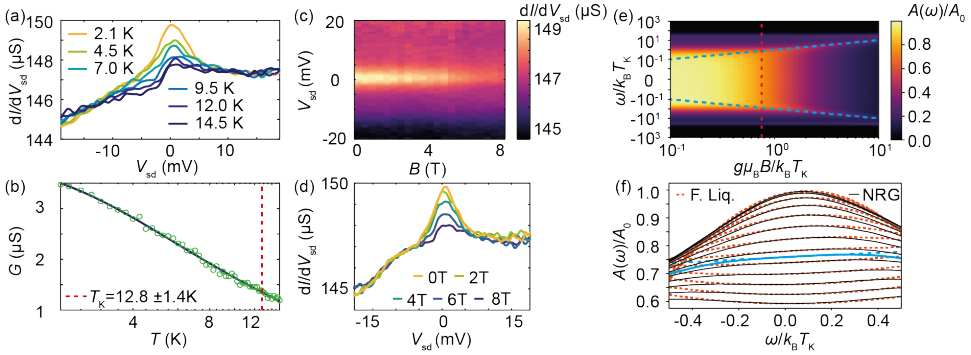

Figure 6.2: (a) $\mathrm{d}I/\mathrm{d}V_{\mathrm{sd}}$, of the molecular quantum dot vs V_{sd} at different temperatures. (b) Peak conductance of Kondo resonance vs temperature and fit to a spin-$1/2$ Kondo model yielding $T_{\mathrm{K}} \approx 12.8$ K, see SM.1.3 and SM.2.3 [1]. (c)-(d) $\mathrm{d}I/\mathrm{d}V_{\mathrm{sd}}$ vs V_{sd} at different magnetic fields. (e) NRG Spectral function $A(\omega)/A_0$ with $A_0 = 1/2\pi\Gamma$ of the Anderson model vs energy (ω) and magnetic field for $V_{\mathrm{g}} = (\varepsilon_0 + U/2)/\Gamma = -1$ and $U/\Gamma = 8$. Vertical dashed line: splitting field $B_{\mathrm{c}} = 0.75 k_{\mathrm{B}} T_{\mathrm{K}}/g\mu_{\mathrm{B}}$. Blue dashed lines: positions $[\omega(B) = \pm g\mu_{\mathrm{B}} B]$ of the split Kondo peaks in $A(\omega)$ for $B \gg B_{\mathrm{c}}$ [36, 37]. (f) $A(\omega)/A_0$ from line cuts in (e) at $g\mu_{\mathrm{B}}B/k_{\mathrm{B}}T_{\mathrm{K}} = 0, 0.1, \ldots, 0.7, 0.75, 0.8, \ldots, 1.2$ (solid lines), compared to $A(\omega)/A_0$ from Fermi-liquid theory (dashed lines). Blue lines: $B = B_{\mathrm{c}}$. A g factor of $g = 2$ is used, as measured by electron paramagnetic resonance (SM.4.2 [1]).

in Figs. 6.2(a) and 6.2(d) which may mask the appearance of a splitting at zero bias. In addition, the largest field used, $B = 8$ T, was only marginally larger than B_{c}. For a device where higher fields relative to B_{c} could be applied, such a splitting is observed (SM.2.1 [1]). Despite these complications in extracting B_{c} from $\mathrm{d}I/\mathrm{d}V_{\mathrm{sd}}$ for the device studied, there is also a general problem in doing so, which can be appreciated by attempting this from exact theoretical results. This is illustrated in Figs. 6.2(e)-6.2(f) which show the spectral function $A(\omega = eV_{\mathrm{sd}}) \sim \mathrm{d}I/\mathrm{d}V_{\mathrm{sd}}$ within the NRG method and within Fermi-liquid theory. While the precise value of B_{c} is impossible to determine visually in Fig. 6.2(e) (vertical dashed line), it can be deduced from the line cuts in Fig. 6.2(f) as the field where the curvature of $A(\omega)$ vanishes. However, such accuracy in second derivatives of $A(\omega = eV_{\mathrm{sd}}) \sim \mathrm{d}I/\mathrm{d}V_{\mathrm{sd}}$ is difficult to attain from experimental data with finite error bars.

Thermocurrent spectroscopy resolves the above difficulty. Figures. 6.3(a)-6.3(b) show the measured thermocurrent versus bias voltage and magnetic field, while Figs. 6.3(c)-6.3(d) show analogous theory results within an approximate nonequilibrium Green function approach (SM.3.6 [1]). First, notice that the large non-Kondo contribution to the differential conductance [Figs. 6.2(a) and 6.2(d)], is absent in the thermocurrent Fig. 6.3(b), with the latter being largely symmetric in magnitude around zero bias, in agreement with theory [Fig. 6.3(d)]. This is because the thermocurrent effectively measures a difference of electrical currents (in the presence or absence of thermal bias), and thus filters out the non-Kondo contributions. By the same token the thermocurrent therefore probes universal aspects of Kondo physics more precisely than the differential conductance. Secondly, we now see a clear feature, in the form of a zero-bias kink with a negative slope of the thermocurrent, appearing in I_{th} at a field $B = B_{\mathrm{th}}$. This is qualitatively captured, together with

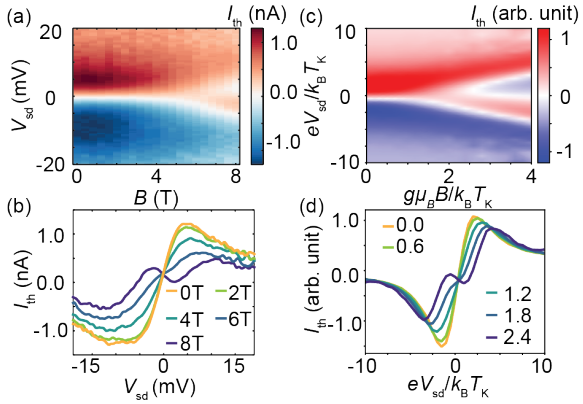

Figure 6.3: (a)-(b) Measured I_{th}, vs V_{sd} at different magnetic fields. (c)-(d) Calculated I_{th} vs V_{sd} at different magnetic fields $g\mu_{\mathrm{B}}B/k_{\mathrm{B}}T_{\mathrm{K}}$ for the Anderson model in Fig. 6.1(c) with $V_{\mathrm{g}} = -2.5$, $U/\Gamma = 8$, $\Delta T/T_{\mathrm{K}} = 0.2$ and $T/T_{\mathrm{K}} = 0.5$.

the behavior at $V_{\mathrm{sd}} \gtrsim T_{\mathrm{K}}$, by the approximate approach [Figs. 6.3(c) and 6.3(d)]. However, the precise field at which this feature occurs and its connection to B_{c} requires a more exact theory, which is provided by the higher-order Fermi-liquid theory [Eq. (6.2) and SM.3.5 [1]]. Preempting the result of this theory, we note that analyzing the experimental data in Figs. 6.3(a) and 6.3(b) for the slope of the thermocurrent $\mathrm{d}I_{\mathrm{th}}/\mathrm{d}V_{\mathrm{sd}}(V_{\mathrm{sd}} = 0)$ at zero-bias voltage as a function of magnetic field, we find that this slope vanishes (*i.e.*, the kink appears) at $B_{\mathrm{th}} \approx 6.6$ T. This value is within 10% of the expected $B_{\mathrm{c}} \approx 7.15$ T and already suggests that $B_{\mathrm{th}} = B_{\mathrm{c}}$, and, hence, that the splitting of the Kondo resonance can be directly measured in the bias voltage dependence of $I_{\mathrm{th}}(V_{\mathrm{sd}})$.

Equation (6.2), with $s_i(B), i = 0, 1$ evaluated exactly for all B within the NRG (SM.3.5 [1]), allows us to address the experimentally observed sign change of $(\partial I_{\mathrm{th}}(V)/\partial V_{\mathrm{sd}})_{V=0} \propto s_1(B)$ upon increasing B above B_{th} (the "kink") and to extract B_{th}. Figure 6.4(a) shows the normalized zero-bias thermocurrent slope $\propto s_1(B)/s_1(0)$, the normalized zero-bias thermocurrent $\propto s_0(B)/s_0(0)$ and the normalized curvature coefficient $\propto c_V(B)/c_V(0)$ as a function of B and for a range of V_{g} in the Kondo regime. First, notice that both $c_V(B)/c_V(0)$ and $s_1(B)/s_1(0)$ [in contrast to $s_0(B)/s_0(0)$] are universal scaling functions of $g\mu_{\mathrm{B}}B/k_{\mathrm{B}}T_{\mathrm{K}}$ with only a weak dependence on V_{g} [inset Fig. 6.4(a)], and while distinct, they lie within about 1% of each other [inset Fig. 6.4(a) and Fig. S13 [1]]. Thus, measuring the field dependence of $s_1(B)$ *via* thermocurrent spectroscopy, requiring only a first derivative with respect to bias voltage, equivalently probes the magnetic-field universality from an electrical conductance measurement, which, however, requires a second derivative with respect to bias voltage and is consequently less accurate. Furthermore, since both $s_1(B)$ and $c_V(B)$ change sign at the same magnetic field, *i.e.*, $B_{\mathrm{th}} = B_c \approx 0.75 k_{\mathrm{B}}T_{\mathrm{K}}/\mu_{\mathrm{B}}$, thermocurrent measurements of Kondo correlated quantum dots at finite bias voltage provide a new way to determine the splitting of the Kondo resonance *via* a sign change in the slope of the thermocurrent with respect

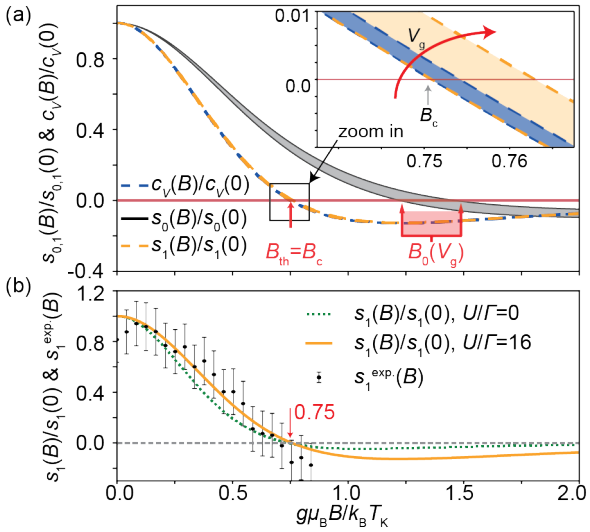

Figure 6.4: (a) Normalized zero-bias thermocurrent slope $s_1(B)/s_1(0)$ and curvature coefficient $c_V(B)/c_V(0)$ vs $g\mu_B B/kT_K$, for gate voltages $1 \leq V_g = (\varepsilon_0 + U/2)/\Gamma \leq 5$ in the Kondo regime exhibiting scaling collapse [Anderson model in Fig. 6.1(c) with $U/\Gamma = 16$]. Also shown is the nonuniversal normalized zero-bias thermocurrent $s_0(B)/s_0(0)$ with a sign change at a strongly V_g-dependent B_0. Inset: $c_V(B)/c_V(0)$ and $s_1(B)/s_1(0)$ in the region around $B = B_{th} = B_c \approx 0.75 k_B T_K/g\mu_B$, and their V_g-dependence. (b) Least-squares fit of the experimental zero-bias thermocurrent slope $s_1^{exp.}(B)$ to the universal curve for $s_1(B)/s_1(0)$. Error bars denote 1σ confidence intervals. A fit to the noninteracting case with $U = 0$ and $\varepsilon_0 = -0.1\Gamma$ (green dotted line) yielded an RMS deviation that was 194% larger than for the Kondo scaling curve. The estimated experimental $B_{th} \approx 0.69 k_B T_K/g\mu_B$ is close to theory $(0.75 k_B T_K/g\mu_B)$.

to bias voltage.

In Fig. 6.4(b) we show a direct comparison between theory and experiment for the slope of the zero-bias thermocurrent as a function of magnetic field. The experimental data follows well the universal curve for $s_1(B)/s_1(0)$, and the aforementioned value extracted from this data for $B_{th} \approx 6.6$ T $(g\mu_B B_{th}/k_B T_K = 0.69)$, is consistent with the expected splitting field of $B_{th} \approx 7.15$ T $(g\mu_B B_{th}/k_B T_K \approx 0.75)$. The largest available field, 8 T, did not allow accessing the minimum of the $s_1(B)$ vs B curve or the slow increase of $s_1(B)$ to zero at $B \gg T_K$. The agreement between theory and experiment at the largest fields measured $B > B_{th}$ is reduced, but still within the error bounds of the experimental data. The extracted $B_c = B_{th}$ from the thermocurrent validates the theoretical prediction with higher accuracy than what has so far been reported. The large energy level separation in a molecular quantum dot grants the observed good agreement between the theory and experiment, even under a simple single-level assumption in the transport window [Fig. 6.1(c)].

6.3. Conclusion

In summary, we have studied the effect of a magnetic field on a Kondo-correlated molecular quantum dot *via* nonlinear thermocurrent spectroscopy. We demon-

strated theoretically and confirmed experimentally, that the nonequilibrium thermocurrent, *via* its zero-bias slope $s_1(B)$, exhibits universal Fermi-liquid magnetic-field scaling, and that the vanishing of $s_1(B)$ at $B = B_{\mathrm{th}}$ with $B_{\mathrm{th}} = B_{\mathrm{c}}$, directly probes the splitting of the Kondo resonance. Since the thermocurrent is largely robust against parasistic conductive phenomena, it provides a more clearcut signature of this hallmark than is available from conductance measurements only. The ability to tune thermal and voltage bias, as well as temperature and magnetic field, opens up possibilities for using thermocurrent spectroscopy to yield insights into Kondo physics of nanoscale systems and may prompt theoretical investigations to address the largely unexplored area of nanosystems far from thermal and electrical equilibrium.

References

(1) Hsu, C.; Costi, T. A.; Vogel, D.; Wegeberg, C.; Mayor, M.; van der Zant, H. S. J.; Gehring, P. *Physical Review Letters* **2022**, *128*, 147701.

(2) de Haas, W. J.; de Boer, J.; van dën Berg, G. J. *Physica* **1934**, *1*, 1115–1124.

(3) Kondo, J. *Prog. Theor. Phys.* **1964**, *32*, 37–49.

(4) Hewson, A. C., *The Kondo Problem to Heavy Fermions*; Cambridge University Press, Cambridge: 1997.

(5) Georges, A.; Kotliar, G.; Krauth, W.; Rozenberg, M. J. *Rev. Mod. Phys.* **1996**, *68*, 13–125.

(6) Löhneysen, H. v.; Rosch, A.; Vojta, M.; Wölfle, P. *Rev. Mod. Phys.* **2007**, *79*, 1015–1075.

(7) Goldhaber-Gordon, D.; Shtrikman, H.; Mahalu, D.; Abusch-Magder, D.; Meirav, U.; Kastner, M. A. *Nature* **1998**, *391*, 156–159.

(8) Cronenwett, S. M.; Oosterkamp, T. H.; Kouwenhoven, L. P. *Science* **1998**, *281*, 540–544.

(9) Park, J.; Pasupathy, A. N.; Goldsmith, J. I.; Chang, C.; Yaish, Y.; Petta, J. R.; Rinkoski, M.; Sethna, J. P.; Abruña, H. D.; McEuen, P. L.; Ralph, D. C. *Nature* **2002**, *417*, 722–725.

(10) Madhavan, V.; Chen, W.; Jamneala, T.; Crommie, M.; Wingreen, N. *Science* **1998**, *280*, 567–569.

(11) Ozaki, S.; Itakura, K.; Kuramoto, Y. *Phys. Rev. D* **2016**, *94*, 074013.

(12) Gross, D. J.; Wilczek, F. *Phys. Rev. D* **1973**, *8*, 3633–3652.

(13) David Politzer, H. *Physics Reports* **1974**, *14*, 129–180.

(14) Anderson, P. W. *Journal of Physics C: Solid State Physics* **1970**, *3*, 2436.

(15) Wilson, K. G. *Rev. Mod. Phys.* **1975**, *47*, 773–840.

(16) Andrei, N.; Furuya, K.; Lowenstein, J. H. *Rev. Mod. Phys.* **1983**, *55*, 331–402.

(17) Goldhaber-Gordon, D.; Göres, J.; Kastner, M. A.; Shtrikman, H.; Mahalu, D.; Meirav, U. *Phys. Rev. Lett.* **1998**, *81*, 5225–5228.

(18) Gonzalez-Buxton, C.; Ingersent, K. *Phys. Rev. B* **1998**, *57*, 14254–14293.

(19) Roch, N.; Florens, S.; Costi, T. A.; Wernsdorfer, W.; Balestro, F. *Phys. Rev. Lett.* **2009**, *103*, 197202.

(20) Parks, J. J.; Champagne, A. R.; Costi, T. A.; Shum, W. W.; Pasupathy, A. N.; Neuscamman, E.; Flores-Torres, S.; Cornaglia, P. S.; Aligia, A. A.; Balseiro, C. A.; Chan, G. K.-L.; Abruña, H. D.; Ralph, D. C. *Science* **2010**, *328*, 1370–1373.

(21) Iftikhar, Z.; Anthore, A.; Mitchell, A. K.; Parmentier, F. D.; Gennser, U.; Ouerghi, A.; Cavanna, A.; Mora, C.; Simon, P.; Pierre, F. *Science* **2018**, *360*, 1315–1320.

(22) Costi, T. A.; Bergqvist, L.; Weichselbaum, A.; von Delft, J.; Micklitz, T.; Rosch, A.; Mavropoulos, P.; Dederichs, P. H.; Mallet, F.; Saminadayar, L.; Bäuerle, C. *Phys. Rev. Lett.* **2009**, *102*, 056802.

(23) Oguri, A.; Hewson, A. C. *Phys. Rev. Lett.* **2018**, *120*, 126802.

(24) Oguri, A.; Hewson, A. C. *Phys. Rev. B* **2018**, *97*, 035435.

(25) Filippone, M.; Moca, C. P.; Weichselbaum, A.; von Delft, J.; Mora, C. *Phys. Rev. B* **2018**, *98*, 075404.

(26) Nozières, P. *Journal of Low Temperature Physics* **1974**, *17*, 31–42.

(27) Costi, T. A. *Phys. Rev. Lett.* **2000**, *85*, 1504–1507.

(28) Kogan, A.; Amasha, S.; Goldhaber-Gordon, D.; Granger, G.; Kastner, M. A.; Shtrikman, H. *Phys. Rev. Lett.* **2004**, *93*, 166602.

(29) Quay, C. H. L.; Cumings, J.; Gamble, S. J.; Picciotto, R. d.; Kataura, H.; Goldhaber-Gordon, D. *Phys. Rev. B* **2007**, *76*, 245311.

(30) Kretinin, A. V.; Shtrikman, H.; Goldhaber-Gordon, D.; Hanl, M.; Weichselbaum, A.; von Delft, J.; Costi, T.; Mahalu, D. *Phys. Rev. B* **2011**, *84*, 245316.

(31) Hata, T.; Teratani, Y.; Arakawa, T.; Lee, S.; Ferrier, M.; Deblock, R.; Sakano, R.; Oguri, A.; Kobayashi, K. *Nature Communications* **2021**, *12* 3233, 3233.

(32) Gehring, P.; Sowa, J. K.; Hsu, C.; de Bruijckere, J.; van der Star, M.; Le Roy, J. J.; Bogani, L.; Gauger, E. M.; van der Zant, H. S. J. *Nature Nanotechnology* **2021**, *16*, 426–430.

(33) Van Roermund, R.; Shiau, S.-y.; Lavagna, M. *Physical Review B* **2010**, *81*, 165115.

(34) Svilans, A.; Josefsson, M.; Burke, A. M.; Fahlvik, S.; Thelander, C.; Linke, H.; Leijnse, M. *Phys. Rev. Lett.* **2018**, *121*, 206801.

(35) Costi, T. A. *Phys. Rev. B* **2019**, *100*, 161106.

(36) Wingreen, N. S.; Meir, Y. *Phys. Rev. B* **1994**, *49*, 11040–11052.

(37) Moore, J. E.; Wen, X.-G. *Phys. Rev. Lett.* **2000**, *85*, 1722–1725.

(38) Zhang, Y. H.; Kahle, S.; Herden, T.; Stroh, C.; Mayor, M.; Schlickum, U.; Ternes, M.; Wahl, P.; Kern, K. *Nature Communications* **2013**, *4*, 1–6.

(39) Frisenda, R.; Gaudenzi, R.; Franco, C.; Mas-Torrent, M.; Rovira, C.; Veciana, J.; Alcon, I.; Bromley, S. T.; Burzurí, E.; van der Zant, H. S. J. *Nano Letters* **2015**, *15*, 3109–3114.

(40) Gaudenzi, R.; de Bruijckere, J.; Reta, D.; Moreira, I. d. P. R.; Rovira, C.; Veciana, J.; van der Zant, H. S. J.; Burzurí, E. *ACS Nano* **2017**, *11*, 5879–5883.

(41) De Bruijckere, J.; Gehring, P.; Palacios-Corella, M.; Clemente-León, M.; Coronado, E.; Paaske, J.; Hedegård, P.; van der Zant, H. S. J. *Phys. Rev. Lett.* **2019**, *122*, 197701.

7

Chirality-induced spin selectivity

Chirality is a mirror symmetry property which is prevalent in nature, ranging from biological systems like DNA and proteins to solid state materials like carbon nanotubes and chiral crystals. Numerous reports exist showing that chiral molecules can induce spin-polarized currents with spin polarization determined by the chirality of the molecules. This potential for non-magnetic spin current generators has attracted much attention to these systems. So far, the so-called chirality-induced spin selectivity (CISS) has only been studied in large assemblies of molecules and there is a large discrepancy between the experimental results and theoretical modelings. In this chapter, we explore novel single-molecule junction devices for the CISS effect characterization, where spin-polarized currents can be generated and detected at the single-molecule level.

This chapter contains on-going unpublished experimental works on the CISS effect.

7.1. Introduction

With the discovery of giant magnetoresistance (GMR)[1], *spintronics* has become the next-generation low-power, ultrafast, large-capacity and non-volatile electronics. The key concept of spintronics is the ability to utilize the spin degrees of freedom in a material [1–3]. Particularly, the generation, manipulation and detection of spin currents are critical for the fundamental understanding of interactions between spins and environments, and the realization of spintronic applications [4, 5]. Typically, the generation and detection are dual to each other, manifested in the same physical systems. For example, spin current detection and generation can both be achieved in magnetic spin valves, strong spin-orbit coupled materials (spin-Hall metals, topological insulators) or *via* electromagnetic wave application (spin pumping), etc. [2].

Conventionally, spin current generation and detection are only possible in metallic systems or crystalline structures where the breaking of time-reversal symmetry occurs explicitly either externally, *e.g. via* an external magnetic field, or intrinsically, *e.g. via* spin-orbit coupling. However, in a recent photoemission experiment on a layer of double-stranded DNA (ds-DNA) assembled on an Au substrate by R. Naaman and coworkers, it was reported that electrons ejected from the Au substrate were spin-polarized when they propagated through the organic ds-DNA layer [6]. The connection between the right-handed chirality of ds-DNA and spin-polarized current was surprising as it suggested that spin-polarized current may be generated by organic molecules with different chiralities. Such a phenomenon, where spin polarization is induced by the chirality of molecules, is the so-called chirality-induced spin selectivity (CISS) effect. This observation has opened a new path for spin current generation and detection, based on systems of organic chiral molecules [7]. Soon after the first photoemission experiment, many follow-up experimental works were performed to study the CISS effect, typically in the forms of atomic force microscopy (AFM) [8–12], electrochemistry [13] and photoemission [11, 14]. In these experiments, assemblies of molecules were used and the magnitude of spin polarization was claimed to be as large as tens of percent.

Nonetheless, there is a controversy concerning the origin of the large spin polarization in these organic layers. Most of the theoretical work obtained that spin polarization in a molecular system with realistic spin-orbit couplings typically lies below one percent [15–19], thus there is a large discrepancy between the experimental observations and theoretical understanding. Two important reasons for the discrepancy are: First, most theoretical studies were performed at the single-molecule level while the experiments were realized with large assemblies of molecules. Second, the observed quantities in these experiments, such as magnetoresistance (MR), are not proper quantities to be compared with spin polarization. Therefore, to bridge the gap between the experiment and theory and for the practical purpose of molecular spintronics, it is essential to develop a proper experimental scheme where we can characterize the CISS effect in spin and charge transport at the single-molecule

[1] The Nobel Prize in Physics 2007 was awarded jointly to Albert Fert and Peter Grünberg "for the discovery of Giant Magnetoresistance." https://www.nobelprize.org/prizes/physics/2007/summary/.

level.

Recent theoretical models explicitly consider the time-reversal symmetry of metal-molecule-metal junctions [20–22]. The Onsager–Casimir reciprocity states that two-terminal MRs are zero in the linear response regime and finite in the non-linear regime. The Büttiker's reciprocity suggests that a two-terminal non-interacting system, which respects time reversal symmetry, yields a MR of zero in the linear and non-linear regimes. These findings mean that conventional two-terminal techniques, *e.g.* magnetic junctions that is commonly used in MR measurements, are not suitable devices to quantify the CISS effect in the linear regime. Therefore, we aim to circumvent these limits by developing a device, which can directly detect the spin polarization of the electron transmission by chiral molecules at the single-molecule level.

In this chapter, we discuss several approaches to characterize the CISS effect. In Sec. 7.2, we show the basic two-terminal mechanically controlled break junction (MCBJ) characterizations of the chiral molecules candidates for the CISS experiments. In Sec. 7.3 we discuss new device designs which take the above considerations into account for a proper characterization of the CISS effect. These devices incorporate non-local spintronic measurement geometries at the single-molecule level, which are consistent with the current single-molecule theoretical work. Finally, in Sec. 7.4, we discuss the measurement protocols and results for the CISS effect with our device designs.

7.2. MCBJ characterizations of chiral molecules

In this section, we show the mechanically controlled break junction (MCBJ) characterizations of Helicene molecules (Fig. 7.1) synthesized by N. Salinas in B. W. Laursen's group from 2018 to 2019, and of PDI (Fig. 7.2) and BINAP (Fig. 7.6) molecules synthesized by A. Philip in F. Grozema's group from 2019 to 2021.

7.2.1. Helicene molecules

Helicenes are aromatic molecules which resemble the shape of a helix. Due to their helical topology, they are good candidate molecules to study in the context of the CISS effect. In fact, Helicenes were studied in the early report of the CISS effect in self-assembled monolayers with atomic force microscopy (AFM) [9], and they were shown to create chirality-dependent magnetoresistance. Therefore, we had also characterized Helicene molecules with a MCBJ technique in the previous study [23]. However, because of the short Helicene length, long anchoring groups and the non-optimal anchoring positions in the previous study, the molecules were not ideal for studying the CISS effect. Thus, new molecular designs of Helicenes were explored and the chemical structures are shown in Figs. 7.1a-b. In both molecules, the anchoring groups of SAc and SMe are located at the two ends of the Helicene molecules, making the end-to-end paths helical, with an approximately complete wind.

Here, we perform single-molecule measurements on these two molecules with SAc and SMe anchoring groups *via* the MCBJ technique as described in Chap. 2,

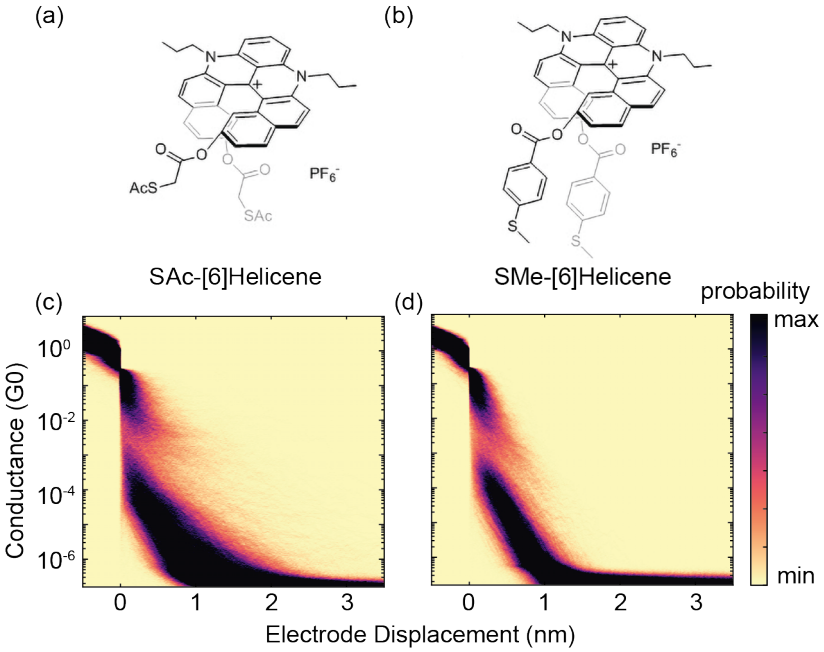

Figure 7.1: (a)-(b) Chemical structures of [6]Helicene molecules with anchoring groups of thiol acetate (SAc) and methyl sulphide (SMe). (c) 2D conductance histogram of SAc-[6]Helicene with 5969 consecutive traces at a bias voltage of 100 mV. (d) 2D conductance histogram of SMe-[6]Helicene with 10000 consecutive traces at a bias voltage of 100 mV.

and the results are shown in Figs. 7.1c-d. In both cases, no clear molecular conductance plateaus are observed. This is different from the previous report where slanted conductance plateaus were observed at around a few times of $10^{-6}\ G_0$. This suggests that SAc-[6]Helicene and SMe-[6]Helicene have either a poor anchoring onto the gold electrodes, or low conductance values, below the detection limit. Although we cannot safely identify the reason for this absence of molecular plateaus, we still conclude that these two molecules are also not ideal for the CISS effect study, as no clear fully-stretched molecular features are observed with detectable conductance values.

7.2.2. Twisted PDI-based molecules

Perylenediimide (PDI)-based molecules are a family of organic molecules which are commonly used as organic semiconductors and dyes. Their basic structure is shown in Fig. 7.2a and the precursor molecule Perylenetetracarboxylic dianhydride (PTCDA) is shown in Fig. 7.2b. The derivative molecules shown in Figs. 7.2c-g are measured with the MCBJ technique.

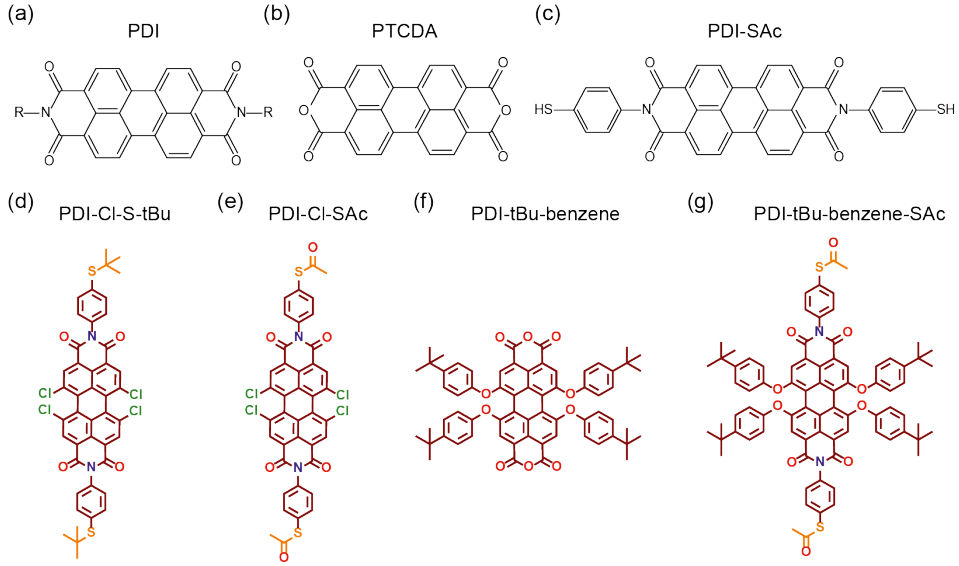

Figure 7.2: PDI-based molecules. (a) Basic structure of a PDI-based molecule. (b) PTCDA precursor. (c) PDI-SAc backbone achiral molecule. (d)-(e) Twisted PDI-based molecule with chlorine side group with anchoring groups of thiol tert-Butyl (S-tBu) and thiol acetate (SAc) respectively. (f)-(g) Twisted non-anchored and SAc-anchored PDI-based molecules with bulky side groups respectively.

Achiral PDI molecules

First, the achiral PTCDA and PDI-SAc backbone molecules (Fig. 7.2b and c) are characterized with the fast-breaking technique in a MCBJ setup. The 2D conductance histograms of PTCDA and PDI-SAc are shown in Figs. 7.3a-b. While both measurements show no clear conductance plateau, PDI-SAc shows some molecular features in addition to the gold-to-gold direct tunneling traces. Fig. 7.3c shows the result of the clustering algorithm with 4 classes on PDI-SAc [24], which gives a most probable conductance value around $G = 2.5 \times 10^{-5} G_0$. This conductance is close to the conductance value ($G = 1.2 \times 10^{-5} G_0$) determined in a scanning tunneling microscopy (STM) break junction experiment [25]; however, the short length of the molecular traces both in the MCBJ measurement and in the previous STM report suggests that the molecule is not fully stretched during the breaking event. The poor ability to measure the full end-to-end PDI-SAc molecule is consistent with the strong surface absorption of PTCDA-like molecules on Au and other metallic surfaces [26].

Chiral PDI molecules

To introduce chirality into the above-mentioned achiral reference molecules, side groups of Cl and tBu-benzene are added to create a torsion in the plane of the PDI molecules, as shown in Figs. 7.2d-g. Additionally, the torsion in the molecules and side group may prevent the strong absorption of the PDI molecules onto the Au electrodes. Figure 7.4 shows the fast-breaking results of the two PDI molecules with

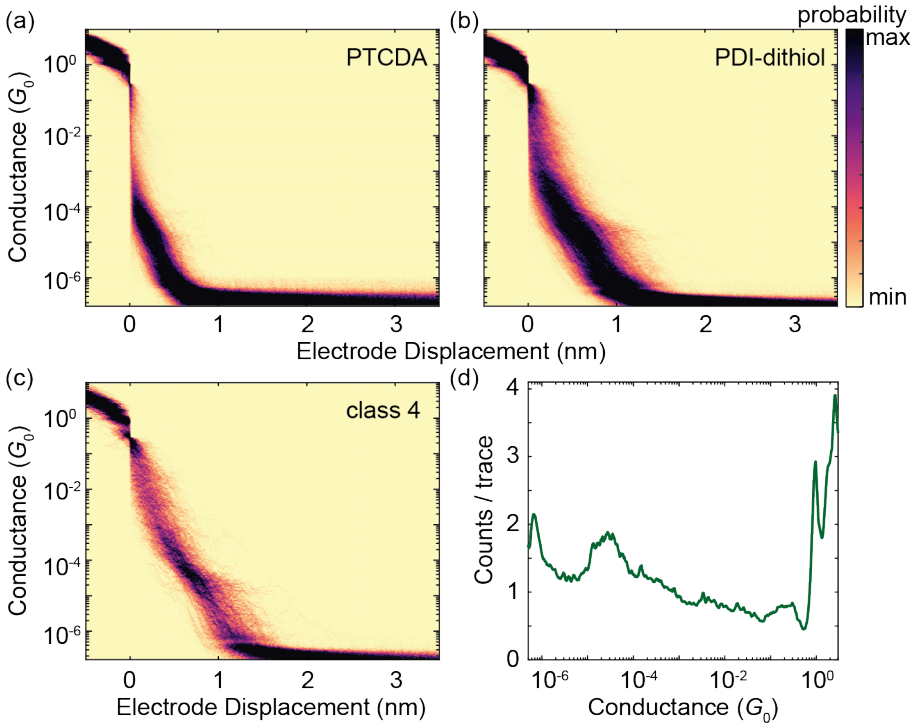

Figure 7.3: Fast-breaking measurement of PTCDA and PDI-SAc. (a)-(b) 2D conductance histograms of PTCDA and PDI-SAc at 100 mV with 2729 and 3500 traces respectively. (c) Clustered 2D conductance histogram of PDI-SAc. (d) 1D conductance histogram of clustered traces in (c).

Cl side groups. Figures 7.4a-b show the 2D conductance histograms of the PDI-Cl-S-tBu (Fig. 7.2d) at two different bias voltages; however, no clear conductance plateau is observed. The 2D conductance histograms of the PDI-Cl-SAc (Fig. 7.2e) are shown in Figs. 7.4c-d. For a bias voltage of 100 mV, no clear molecular conductance plateau is observed. For a bias voltage of 250 mV, the most probable conductance value of $G = 1.2 \times 10^{-5} G_0$ is obtained with the clustering algorithm, as shown in Fig. 7.4e. This conductance value is consistent with the reference PDI-SAc molecule shown above and the STM measurement in a previous report [25]. Similar to the measurement of the reference molecule, the plateau length of 0.7 nm is shorter than the expected fully stretched length of the PDI molecule, suggesting that the end-to-end configuration is not accessible in the MCBJ measurement.

Figure 7.5 shows the 2D conductance histograms of bulky PDI-tBu-benzene and PDI-tBu-benezene-SAc molecules. In the measurements of PDI-tBu-benzene in Figs. 7.5a-b, no conductance plateau is observed for both bias voltages of 100 mV and 250 mV. The absence of a clear plateau is consistent with the absence of an anchoring group. In the case of PDI-tBu-benezene-SAc, the 2D conductance histogram is widely spread in conductance in Figs. 7.5c-d. Particularly, in the case

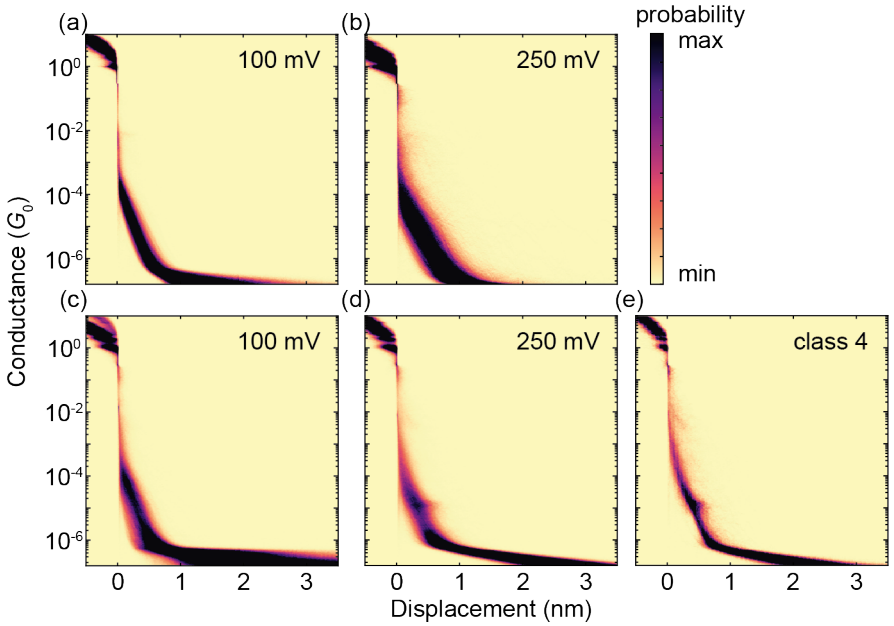

Figure 7.4: Fast-breaking measurement of S-tBu- and SAc- anchored PDI molecules with Cl side groups. (a)-(b) 2D conductance histograms of PDI-Cl-S-tBu at 100 mV and 250 mV with 10000 traces. (c)-(d) 2D conductance histograms of PDI-Cl-SAc at 100 mV and 250 mV with 10000 and 8381 traces, respectively. (e) Clustered 2D conductance histogram of traces in (d).

of 100 mV, there are a few molecular traces with lengths up to 2 nm, indicating the possible transport with end-to-end connections. However, the yield of these traces is below 1% and not reproduced in the case of 250 mV.

The PDI-based molecules studied in this section mostly show no or short plateaus, which suggests that the fully stretched configuration is not accessible statistically *via* the MCBJ technique. To properly characterize the CISS effect, a high yield in the end-to-end conformations is essential as the geometrical path for charge transport plays an important role in spin polarization. We thus explore another possible molecule candidate, BINAP-dithiol molecules, in the next section.

7.2.3. BINAP dithiol molecules

The 2,2′-bis(diphenylphosphino)-1,1′-binaphthyl (BINAP) -based molecules are constructed with 2 naphthyl groups next to each other, which create an axial chirality due to the restricted rotation. The chemical structures of the long BINAP-based and short BINAP-based molecules (hereafter long-BINAP and short-BINAP) are shown in Figs. 7.6a-b. The BINAP-based molecules are expected to show good electronic transparency for their π-conjugation, which is beneficial for single-molecule measurements.

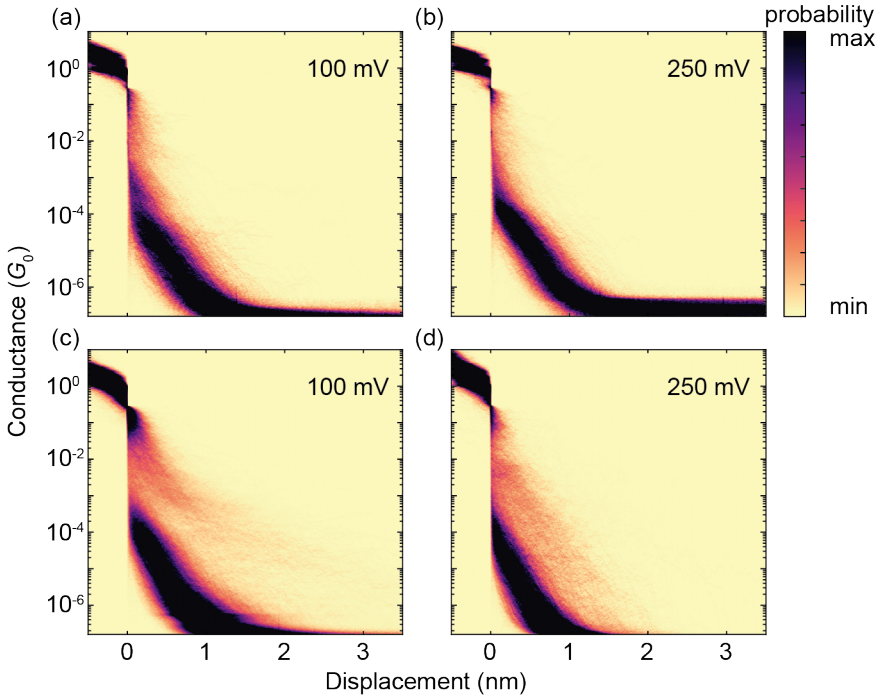

Figure 7.5: Fast-breaking measurement of bulky non-anchored and SAc-anchored PDI-based molecules. (a)-(b) 2D conductance histograms of PDI-tBu-benzene, without anchoring groups, at 100 mV and 250 mV with 10000 and 5038 traces, respectively. (c)-(d) 2D conductance histograms of PDI-tBu-benzene-SAc at 100 mV and 250 mV with 3500 traces.

Long-BINAP

Figure 7.7a shows the raw 2D conductance histogram of a fast-breaking measurement of long-BINAP at a bias voltage of 100 mV with 6258 consecutive traces. Figures 7.7b-e are the clustered 2D conductance histograms of the raw data. Class 1, displayed in Fig. 7.7b, shows a plateau at $G = 4 \times 10^{-3}\ G_0$ with a length of about 1 nm, followed by two short plateaus at around $G = 10^{-4}\ G_0$ and $G = 10^{-6}\ G_0$. Classes 2 and 3 in Figs. 7.7c-d both show plateaus with a length of 2 nm at $G = 3 \times 10^{-6}\ G_0$ and $G = 1.5 \times 10^{-6}\ G_0$, respectively. Class 4 in Fig. 7.7e shows a direct tunneling feature with no conductance plateau.

Conductance plateaus in classes 2 and 3 possibly belong to the same molecular feature as they show the same length and the conductance values are within the error margin. This length is consistent with the expected molecular length of the molecule which is around 1.85 nm, suggesting it to be the end-to-end connected molecular configuration in the junction. The high-conductance plateau manifested in class 1 is explained by a molecular configuration where the molecule is not connected from sulfur to sulfur, as is suggested by its much short molecular length. Nevertheless, when the junction is further stretched, a low-conductance plateau in class 1 appears at a conductance value of $G = 10^{-6}\ G_0$ with a length of about 2 nm,

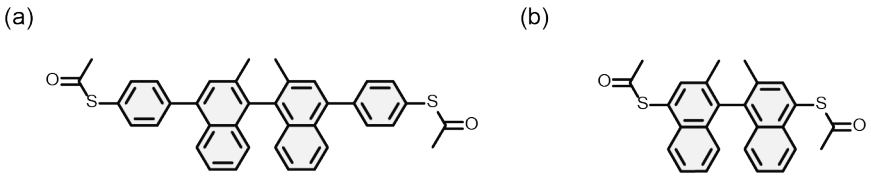

Figure 7.6: (a)-(b) Chemical structures of long and short BINAP-based molecules, which are referred to as long-BINAP and short-BINAP hereafter respectively.

consistent with the fully stretched molecular feature observed in class 2 and 3.

The fast-breaking measurement shows that long-BINAP is suitable for single-molecule measurements, as it can form fully stretched molecular junctions, which is an important factor to characterize the CISS effect. Yet, the conductance of the molecule is only slightly above $G = 10^{-6}\ G_0$. This low transmission is not favorable for the CISS measurement, as the spin current signal can be much smaller than the charge current signal observed in MCBJ measurements.

Short-BINAP

To improve the electronic transmission in the BINAP molecule, a short version of the molecule, *short-BINAP*, is synthesized as shown in Fig. 7.6b. A fast-breaking measurement of short-BINAP is shown in Fig. 7.8a, consisting of 10000 consecutive traces without data selection. To investigate the molecular features, the traces are clustered in 4 classes and the results are shown in Figs. 7.8b-e. Here, only class 1 shows a molecular feature that is not tunneling-like. The molecular feature of class 1 starts with a short conductance plateau at $2 \times 10^{-4}\ G_0$, with a length of 0.8 nm. This plateau decays to a conductance value of about $G = 2 \times 10^{-5} G_0$ at a displacement of about 1.1 nm. The length of the low-conductance plateau is consistent with the expected molecular length (1.05 nm). This suggests that, similar to the long-BINAP, the short-BINAP molecules in a junction can first form a non sulfur-to-sulfur connection and later reach the fully stretched configuration as the junction opens up.

The fast-breaking measurement shows that short-BINAP molelecules forms fully-stretched single-molecule junctions, similar to long-BINAP. Remarkably, the conductance of short-BINAP is approximately one order of magnitude higher than that of long-BINAP, when they are fully stretched. This grants a more promising molecular structure for CISS effect studies with its much higher electronic transmission.

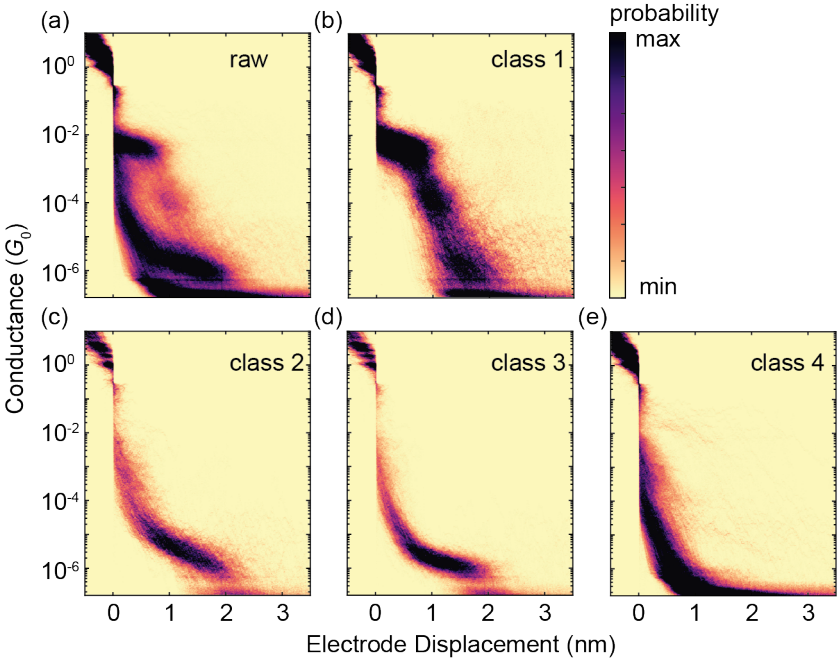

Figure 7.7: Fast-breaking measurement of long-BINAP. (a) Raw 2D conductance histogram consisting of 6258 consecutive traces, without data selection. (b)-(e) Clustered 2D conductance histograms with 4 classes.

7

In summary, with the MCBJ technique, we have characterized three classes of candidate chiral molecules, Helicene, PDI-based and BINAP-based molecules. The Helicene molecules show no clear conductance plateau in the fast-breaking measurements, suggesting the difficulty to contact them in single-molecule junctions with decent conductance levels. PDI-based molecules show short molecular features, which suggests the inaccessibility to an end-to-end connected junction configuration. On the other hand, the BINAP-based molecules show fully stretched molecular plateaus. Particularly, short-BINAP demonstrates a better electronic transparency than long-BINAP at a conductance value of $G = 2 \times 10^{-5}\ G_0$. With this promising candidate molecule for single-molecule junctions, we can study its potential device integration for the CISS characterization. In the following section, we will discuss new device designs, where we can possibly detect spin currents at the single-molecule level.

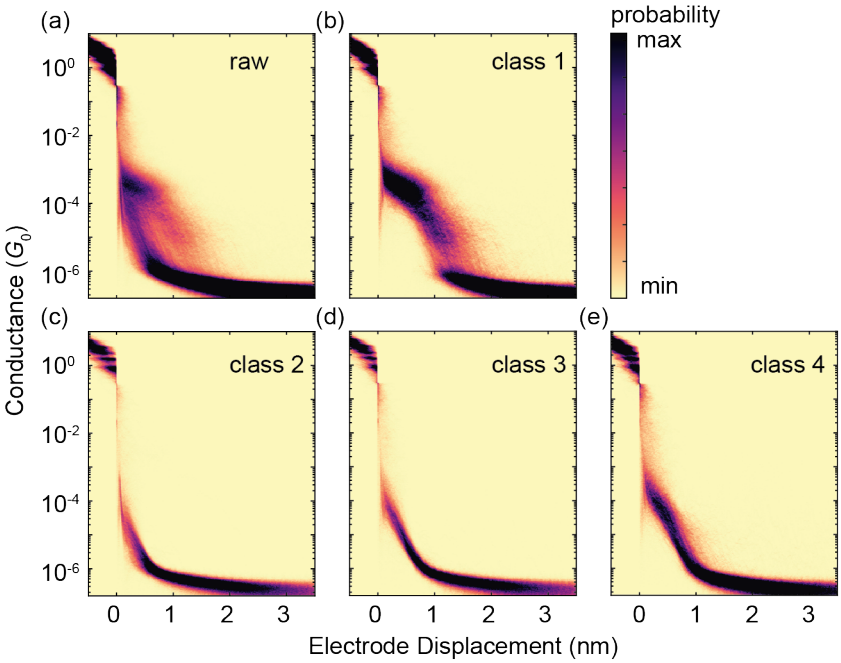

Figure 7.8: Fast-breaking measurement of short-BINAP. (a) Raw 2D conductance histogram consisting of 10000 consecutive traces, without data selection. (b)-(e) Clustered 2D conductance histograms with 4 classes.

7.3. Device designs

To properly study spin-polarized currents in a single-molecule junction, we need to establish appropriate device architectures for spin injection and detection. Initially, we aimed to create two-terminal single-molecule junctions to characterize the spin detection and generation of chiral molecules by MR measurements. However, as already discussed in Sec. 7.1, recent studies suggest that it is symmetry-forbidden to detect finite MR in chiral molecules in such a two-terminal geometry in the linear response regime. This leads to the exploration of alternative "four-terminal" spintronic device geometries for spin detection using non-magnetic materials. In particular, two potential device designs are investigated in this section, both utilizing the spin Hall effect for spin detection in molecular junctions.

7.3.1. Spin Hall effect

The spin Hall effect (SHE) is a phenomenon where spin-polarized charge carriers accumulate at the two transverse edges of a conductor, when a charge current propagates in the longitudinal direction [5, 27]. This charge-to-spin conversion is illustrated in Fig. 7.9. This effect was first theoretically predicted by Dyakonov and Perel in 1971 [28]. It was later referred to as the "spin Hall effect" and proposed to be experimentally detectable by Hirsch [29]. It is only experimentally demonstrated

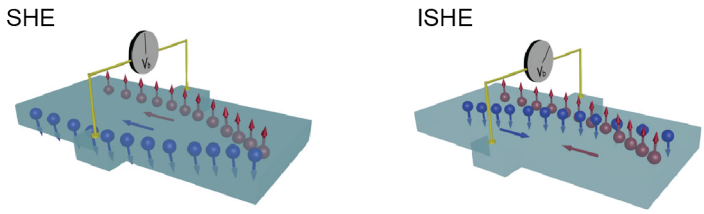

Figure 7.9: Illustration of the SHE (left) and the inverse SHE (ISHE). In SHE, electrons with different spin orientations accumulate at the two different edges of a conductor; yet, because the chemical potentials of the two spin species are the same, no electrical signal is detected. In the case of ISHE, spin currents are converted to charge currents, which can be detected by as a potential difference. The diagram is adapted from Ref. [5].

more than 30 years after the first prediction [30–32]. Importantly, the SHE occurs without the presence of a magnetic field and does not generate a voltage difference at edges of the material, unlike the conventional Hall effect. In addition to the spin current generation from the SHE, the dual of the SHE, the inverse SHE (ISHE) provides a means to convert a pure spin current to a charge current, which can be detected electrically (right panel of Fig. 7.9). The discovery of SHE grants the possibility to generate and detect spin-polarized electrons purely electrically, without using a magnetic material.

There are a few different processes contributing to the manifestation of the SHE, which can generally be classified into two categories: intrinsic and extrinsic, according to the origins of the processes. Generally, a material with a strong spin-orbit coupling can result in a strong SHE, for example, platinum and tungsten. As it is not the scope of this thesis, we do not study the microscopic processes of the SHE. Instead, we employ this well-studied effect for the detection of spin current generated in a molecular junction.

In Secs. 7.3.2 and 7.3.3 below, we describe two SHE-based EMBJ device designs with Pt, a strong spin-orbit coupled non-magnetic noble metal. We note that since there have been no studies regarding the generation or detection of spin currents in EMBJs; therefore, we first investigate the possibility to generate and detect spin currents in these devices without the presence of molecules. We emphasize that it is an important milestone to accomplish as it serves as the foundation for all single-molecule spintronic studies in the future with a similar device design. In the H-shape platinum junction of Sec. 7.3.2, we attempt to achieve this by using Pt as both a spin generator and detector. This device geometry is later shown to be non-ideal due to the weak signal of SHE/ISHE in comparison to other parallel transport mechanisms, such as diffusion. In the reversible spin Hall junction of Sec. 7.3.3, we utilize a magnetic spin generator, Permalloy (Py), and Pt as a spin detector to unequivocally show the possibility to generate and detect spin currents in EMBJs.

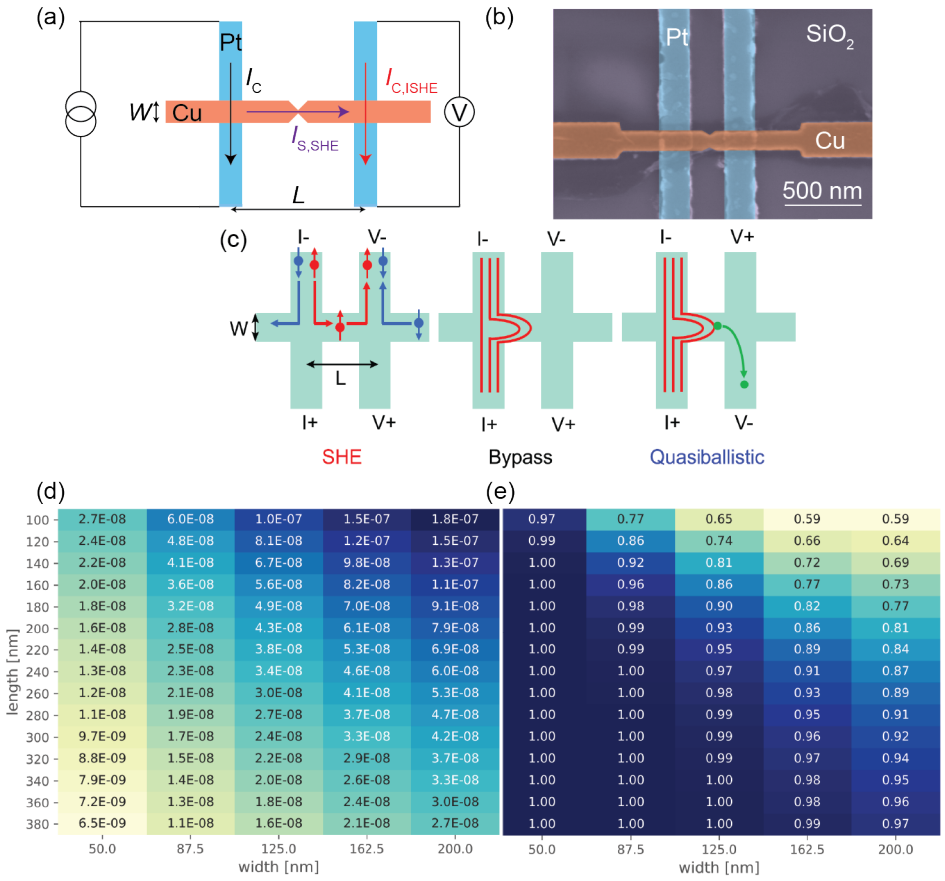

Figure 7.10: (a) Schematic of the H-bar-Pt device. (b) False-colored SEM image of the H-bar-Pt device. (c) Different processes contributing to the voltage signal at the right arm of the H-bar device. The image is adapted from Ref. [33]. (d) Simulated total voltage signal (in the unit of V) detected on the right Pt arm, with different values of width (W) and length (L). The source current used here is 0.5 mA. (e) SHE contribution to the simulated signal on the right Pt arm. The contribution is taken by the ratio between the SHE signal and the total signal, Ratio= $V_{\mathrm{SHE}}/V_{\mathrm{total}}$, where $V_{\mathrm{total}} = V_{\mathrm{SHE}} + V_{\mathrm{by}}$, with the voltage contribution from SHE and bypass mechanisms. Both (d) and (e) are adapted from Ref. [34].

7.3.2. H-shape platinum junction

The first device design for the spin detection in single-molecule junctions is a H-shape platinum junction (hereafter H-bar-Pt), as shown in Fig. 7.10a. To simultaneously generate and detect spin currents in this device without molecules, we place two Pt strips on the two sides of the EMBJ. In this case, the spin current, $I_{\mathrm{S,SHE}}$, is generated *via* the SHE with a source charge current, I_{C}. This spin current then propagates across the EMBJ of Cu and reaches the other Pt arm on the right-hand side, which converts the spin current back to a charge current, $I_{\mathrm{C,ISHE}}$, *via* the ISHE. The generated $I_{\mathrm{C,ISHE}}$ then creates a non-local potential difference that can be detected electrically. The width (W) and lengths (L) of the H-bar-Pt in Fig. 7.10a, are

chosen in the range of few tens to few hundreds of nm for optimal spin signals, which is discussed in detail later in this section. The H-bar-Pt devices are fabricated with standard electron-beam lithography and electron-beam evaporation (details shown in appendix. 7.6.1). Figure 7.10b shows a SEM image of a H-bar-Pt device with $W \approx 100$ nm and $L \approx 300$ nm.

To optimize the device geometry of H-bar-Pt, we look into other similar device designs in the literature for metallic spintronic studies. Similar device geometries with a single material have been investigated theoretically [35] and in experiments [33, 36]. These reports suggest that the detected signals on the right-hand side can also be contributed by other non-spin-polarized processes such as "bypass" and "quasiballistic" transport mechanisms, as depicted in Fig. 7.10c. These two mechanisms are relevant in this device geometry since we are working within the same length scale of the electron mean free path. Essentially, the bypass mechanism is caused by diffusive electrons in the junction and the quasiballistic mechanism is caused by ballistic transport of electrons. The three contributions from SHE, bypass and quasibasllistic mechanisms: $R_{\mathrm{nl}}^{\mathrm{SHE}}$, $R_{\mathrm{nl}}^{\mathrm{by}}$ and $R_{\mathrm{nl}}^{\mathrm{qb}}$ take the forms of [33]:

$$R_{\mathrm{nl}}^{\mathrm{SHE}} = \frac{1}{2} R_{\mathrm{sq}} \Theta_{\mathrm{H}}^2 \frac{W}{\lambda_s} e^{-L/\lambda_s}, \tag{7.1}$$

$$R_{\mathrm{nl}}^{\mathrm{by}} = R_{\mathrm{sq}} e^{-\pi L/W}, \tag{7.2}$$

$$R_{\mathrm{nl}}^{\mathrm{qb}} = -b \times R_{\mathrm{sq}} e^{-\pi L/W + W/\lambda_{rt}}, \tag{7.3}$$

where R_{sq} is the square resistance, Θ is the spin Hall angle, λ_s is the spin diffusion length, and λ_{rt} is the electronic mean free path.

There are a few key parameters in these contributions for a favorable SHE to total signal ratio. First, the spin Hall angle (SHA), Θ_H, needs to be large for a good SHE signal. Pt has a large SHA in comparison to other non-magnetic materials, ranging from $\Theta_H = 0.0037$ to $\Theta_H = 0.12$ under different conditions [5]. Another important parameter is the spin diffusion length, λ_s, of the spin mediator. In our design, we use a heterojunction of Pt and Cu, where Cu is used for spin mediation, unlike the single-metal junction in the literature [33]. This choice is essential for two reasons: First, the spin diffusion length of Cu is large, $\lambda_s = 500$ nm at room temperature [5]. Second, the spin polarization induced by the SHE is out-of-plane (non "collinear" to the spin current) in a single-metal junction. This is not ideal for characterizing the CISS effect, which filters the spin in the direction of the chiral axis in a chiral molecule. This is resolved in our design of a heterojunction of Cu and Pt [37], where the generated spin currents are aligned in plane (more details in Sec. 7.3.3). In addition to these material considerations, we also note that the quasiballistic contribution has a different sign to the other two contributions, which can result in a negative sign in the detected signal [33, 36].

To estimate the signal that can be generated with this device geometry, a master student in the project, Coen de Jong, performed COMSOL simulations [34]. In this case, we also consider the constriction in the center of the H-bar-Pt junctions in

the simulation, distinct from the previous single-metal junction studies. Two main results of the simulations are shown in Figs. 7.10d-e. From Fig. 7.10d, it is observed that the total signal increases as we increase the width and reduce the length of the junction. It is also shown that the total signal is typically in the order of tens of nV, which is difficult to detect even by a lock-in amplifier [38]. In the real experiment, the H-bar-Pt device was measured in a vacuum probe station at room temperature with a lock-in amplifier. However, the noise of the electrical circuit was around a few hundred nV, which is larger than the highest expected non-local signal in the device in Fig. 7.10b. Another insight obtained from the simulation is the ratio between the SHE generated signals and the total signals generated by the bypass and SHE mechanisms described above, shown in Fig. 7.10e. Here, it is observed, that this ratio decreases quickly as we increase the width and reduce the length of the junction. This suggests that there is a trade off between increasing the total signal and maintaining a good SHE to total signal ratio.

In conclusion, the simulations show that the spin signal generated and detected by SHE and ISHE in H-bar-Pt junctions is extremely small, which is in the range of nV. This leads to the unsuccessful detection of spin signals experimentally at room temperature. For improvement of the device, a few modifications can be made: First, an *in-situ* argon ion milling step can be introduced before the deposition of Cu, to decrease the spin relaxation at the interface of Cu and Pt. Second, materials with higher SHA might be used for better SHE, for example, tungsten or Bi-doped copper. However, it is hard to benchmark these materials as they are difficult to evaporate and do not possess the stable nature of Pt.

Although it is in principle possible to improve the device performance of H-bar-Pt junctions, the simulation indicates that our device geometry is already close to the optimal case. We thus explored an alternative option by incorporating a magnetic material, Py, for spin generation in a junction without molecules in the next section.

7.3.3. Reversible spin Hall junction

As the H-bar-Pt failed to provide a measurable spin signal, we took a different approach by including a ferromagnetic spin generator. This design is based on the example of a reversible spin Hall device created by Kimura *et. al.* [37]. The original design of Kimura *et. al.* is shown in Fig. 7.11a (i). Here, Py, an alloy of Ni and Fe, is magnetized by an external magnetic field in plane. This creates a spin-polarized current when a charge current is sourced across the Py and Cu junction following the arrow. The spin current then diffuses to position 3 in the junction which is converted back to a charge current in Pt. Figure 7.11a (ii) shows the detailed spin-to-charge conversion happening in the Pt strip. The spin current enters the Pt strip and is converted back to a charge current *via* the ISHE, which creates a detectable voltage across the Pt strip. The reversed process, which uses Pt for spin generation and Py for spin detection, can also be achieved as shown in Fig. 7.11a (iii) *via* the SHE, thus "reversible". This device geometry has been proved to show a detectable signal from $T = 77$ K to room temperature (Fig. 7.11b shows the case of $T = 77$ K) [37]. We note two important aspects here: First, the spin orientation

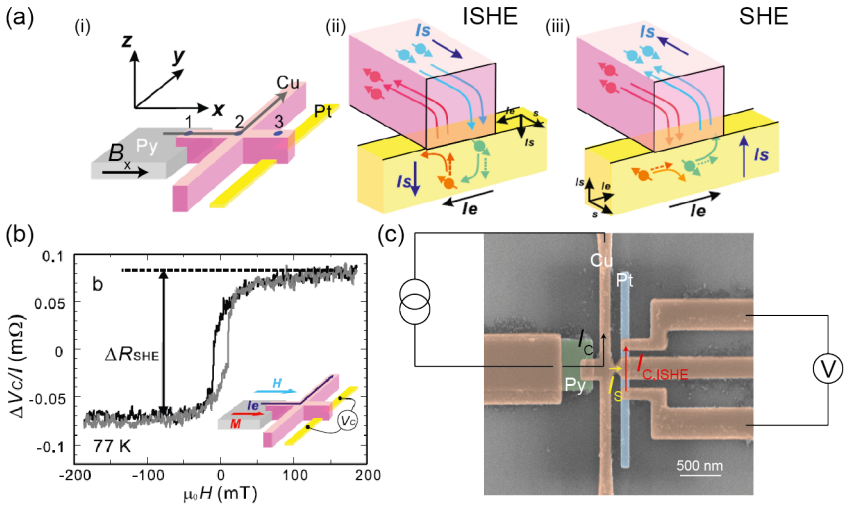

Figure 7.11: (a) Working principle of the reversible spin Hall junction, adapted from Ref. [37]. (i) shows the junction geometry, where Py is used as a spin generator, Cu as a spin mediator and Pt as a spin detector. (ii) and (iii) show the orientation of spin and the propagation direction of the spin current (I_e) and charge current (I_s), in the cases of ISHE and SHE. (b) Non-local resistance measurement performed in the junction in (a), with a source current of 300 μA. The plot is adapted from Ref [37]. (c) False-colored SEM image of the RSHJ device, showing the same measurement schematic in our case with a constriction in the middle.

is "collinear" to the spin current, which is a critical point for measuring the CISS effect as previously mentioned. Second, because we control the magnetization of Py, we can exclude the bypass and quasiballistic effects seen in H-bar-Pt by simply subtracting the non-local resistances at negative B field from the one at positive B field.

Figure 7.11c shows the device for single-molecule CISS measurement (hereafter, we refer to it as reversible spin Hall junction (RSHJ)). The measurement scheme is also shown here, identical to the original design by Kimura *et. al.* A major difference is the incorporation of EMBJ. The location of the EMBJ constriction corresponds to the point between position 2 and 3 in the original design shown in Fig. 7.11a (i).

To realize the RSHJ, the fabrication processes have been substantially modified for optimization. Samuel Golightly, a master student in the project, has performed an extensive optimization study for the device fabrication, and the details can be found Ref. [39]. The complete fabrication steps are listed in App. 7.6.1. There are a few important changes worth noting in this recipe. First, due to the inclusion of Py, an additional lithographic step is performed. As the surface of Py is easily oxidized when it is in contact with air, it is essential to introduce a process to remove the oxide layer. To resolve this, an *in-situ* Ar ion milling step is performed right before the evaporation of Cu onto Py in an electron-beam evaporator. The optimization of the milling process can be found in App. 7.6.2. Another important change is the addition of embedded Au contact pads. This modification facilitates the wire

bonding onto the devices while keeping a clean interface between Cu and Au. The resulting fabricated RSHJ device is shown in the SEM image in Fig. 7.11c.

Besides the fabrication optimization, another important step for the integration of single molecules in RSHJ is the successful electromigration in the device. Traditional EMBJ devices are made out of the gold bridges for the good oxidation resistance and fast self-breaking process of Au [40]. However, in our case of RSHJ, the EMBJ is made out of Cu, which is a difficult material to be controllably electromigrated [41]. For this reason, we have also performed a series of experiments for finding an experimental protocol to create consistently formed nanogaps with size below 1 nm, which is described in detail in App. 7.6.3. In short, there are three key points for a successful electromigration of Cu EMBJ: First, the aspect ratio between the Cu constriction and the bridge needs to be large for easy electromigration. Second, the process needs to be performed under vacuum to prevent the oxidation process during the electromigration. Finally, it is important to increase the electromigration voltage quickly to $V \lessapprox 1\,\mathrm{V}$ at a rate of around $300\,\mathrm{mV/min}$. The voltage is set to rest slightly below 1 V, and is regulated for a gradual EM by the feedback control to prevent an abrupt increase of the junction resistance. The quick ramping is to prevent overheating of the Cu junction, which can result in a melted junction; the voltage below 1 V is to avoid thermionic emission of the Cu bridge, which can create an oversized gap. With the electromigration protocol for Cu EMBJ, we can take another step towards integrating single chiral molecules for the CISS studies.

In addition to the RSHJ described here in this section, we have also explored another device geometry, with a very similar design, shown in the App. 7.6.5. This device, which we refer to as lateral spin valve based RSHJ (LSV-RSHJ), is expected to generate a larger signal for the smaller distance between the Py spin generator and Pt spin detector. The difference is between RSHJ and LSV-RSHJ is the Py spin generator, which is located parallel to the Pt arm in LSV-RSHJ (see Fig. 7.17). Both devices are suitable for two-terminal and "four-terminal non-local" characterizations of single molecules, and we will discuss the measurement protocols in the next sections.

7.4. Measurement protocols

The RSHJ device is a promising candidate for spin generation and detection at the single-molecule level. Since there has only been experimental studies with two-terminal devices for the CISS effect in large assemblies of molecules, we have investigated the possible experiments for the CISS effect in the RSHJ devices at the single-molecule level. Here, we propose a few measurement protocols for the CISS effect characterizations, including both a common two-terminal MR measurement and "four-terminal" spintronic non-local measurement geometries.

7.4.1. Two-terminal measurement

The simplest measurement scheme for characterizing the CISS effect is a two-terminal (2T) measurement geometry, where a spin current generator is connected in series to a chiral molecule. However, as a few theoretical reports have suggested,

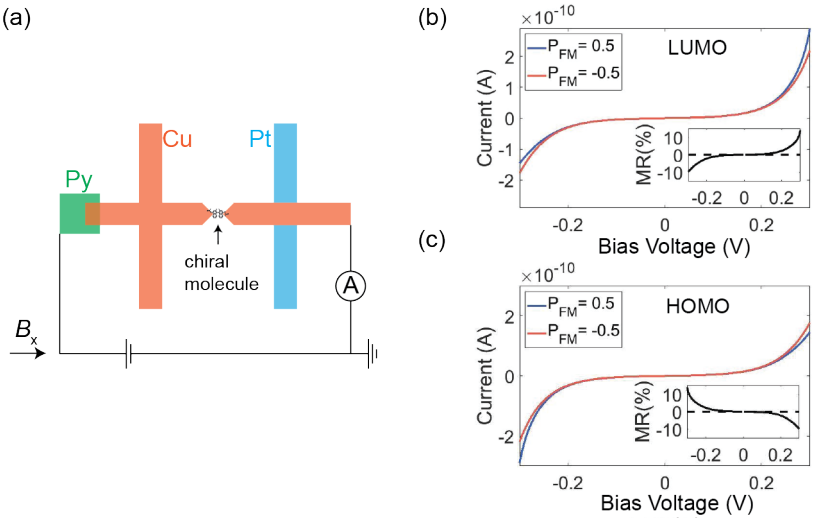

Figure 7.12: (a) Schematic of two-terminal measurement of the CISS effect. (b)-(c) Theoretically predicted nonlinear MR for LUMO- and HOMO- dominated transport in a single-molecule junction, adapted from the work of X. Yang *et. al.* [21]. The sign of P_{FM} represents if a the CISS-origin spin filtering is in the same direction of the magnetization of the ferromagnet.

it is symmetry-forbidden to detect any magnetoresistance, which is chirality dependent, particularly in the linear regime [20–22]. Yet, there is still the possibility to measure chirality-dependent MR in the nonlinear regime, provided that the chiral molecule possesses a spin filtering property.

The RSHJ device design described in the previous section provides a possibility to perform a 2T CISS characterization at the single-molecule level. Nonlinear MR measurements can be achieved in the proposed 2T measurement in Fig. 7.12a. First, a single-molecule junction is formed with a chiral molecule of interest (in our case, short-BINAP molecule), *via* the EMBJ technique. The device is then quickly cooled down to cryogenic temperature to reduce temperature broadening of the Fermi-Dirac distribution and to ensure a good single-molecule junction stability. Afterwards, current-voltage (*IV*) characteristics can be measured beyond the linear regime, together with an in-plane magnetic field.

Figures 7.12b-c are the theoretical predictions by X. Yang *et. al.* [21], for MR measurements in a single-molecule junction. These predictions demonstrate a few important features of the MR curve in a single-molecule junction. First, the most important observation is the aforementioned non-zero MR which only exists in the high-bias, nonlinear regime. Another important observation is the asymmetry between the negative-bias and positive-bias *IV*s and MRs. This is best illustrated when we take Fig. 7.12b for example. Here, the absolute value of current is higher for $P_{FM} = +0.5$ than that for $P_{FM} = -0.5$, at positive bias voltage; but it is the opposite for the case of negative bias voltage. This asymmetry in current also gives an asymmetric MR indicated in the inset. Last, it is also observed that this asymmetry

in *IV*s and MRs can change their signs when different molecular levels (highest occupied molecular orbital and lowest unoccupied molecular orbital) are in the vicinity of the Fermi energy, as shown in 7.12b and c.

Therefore, in an ideal 2T single-molecule measurement three conditions should be satisfied: zero MR in the linear regime, asymmetric MR in the nonlinear regime and a change of sign in MR for different molecular levels. The first two conditions can in principle be tested in the RSHJ device without further modifications, and the third condition may be achieved by including a local back gate to change the molecular levels. These criteria grant the possibility to provide strong evidence for the existence of the CISS effect if they are satisfied.

7.4.2. Four-terminal non-local measurement

A great advantage of a four-terminal (4T) non-local device geometry is the possibility to study spin transport without the limitation of the Onsager reciprocity rule, as it does not apply to a non-equilibrium system [20, 21]. Another benefit of a 4T non-local device is the possibility to separate the charge current from the spin current in a non-local measurement geometry. This removes the non-spin signals of the charge current and provides an unequivocal direct measurement for the spin polarization of electron transmission. Here, we describe a few possible 4T measurement schemes for the CISS effect in RSHJ and LSV-RSHJ devices. The schematics are summarized in Fig. 7.13, and in Fig. 7.18 for only LSV-RHSJ. For clarity, we discuss these measurement schemes with the assumption that the chiral molecule acts as a spin filter, as a result of the CISS effect, which favors a spin current with spin polarization in the same direction as its momentum.

Figure 7.13a shows the most basic 4T non-local measurement for the CISS effect. This geometry is also used in recent reports in the studies of the CISS effect in chiral inorganic crystals [42, 43]. Here, the Pt strip is sourced with a charge current, I_C, which creates a spin-polarized current in the horizontal direction *via* the SHE. The spin current will then pass through the chiral molecule and reach the other electrode. Due to the spin filtering, the spin current with a left-pointing polarization is more favorable than that with a right-pointing polarization. This means that the voltages detected across the molecule are different between two spin currents with different spin polarizations. Therefore, two different non-local resistances are expected to be measured when we change the direction of I_C, as it also changes the spin polarization for the left-going spin current.

Figure 7.13b shows a CISS measurement scheme by using the ISHE. In this case, we directly source the chiral molecule across the Cu junction. Due to the spin filtering of the chiral molecule, there is a higher population of spin current with right-pointing polarization across the Cu bridge. When the two species of spin currents pass through the Pt strip, a portion of them will diffuse into the Pt strip. Due to the ISHE, the spin currents are converted back to a charge current. In this case, because there is an imbalance between the two spin currents, a voltage difference is expected to be detected. Similarly, this measurement scheme was also used to demonstrate the CISS effect in inorganic chiral crystals [42, 43].

Figure 7.13c is a non-local measurement scheme which is very similar to the

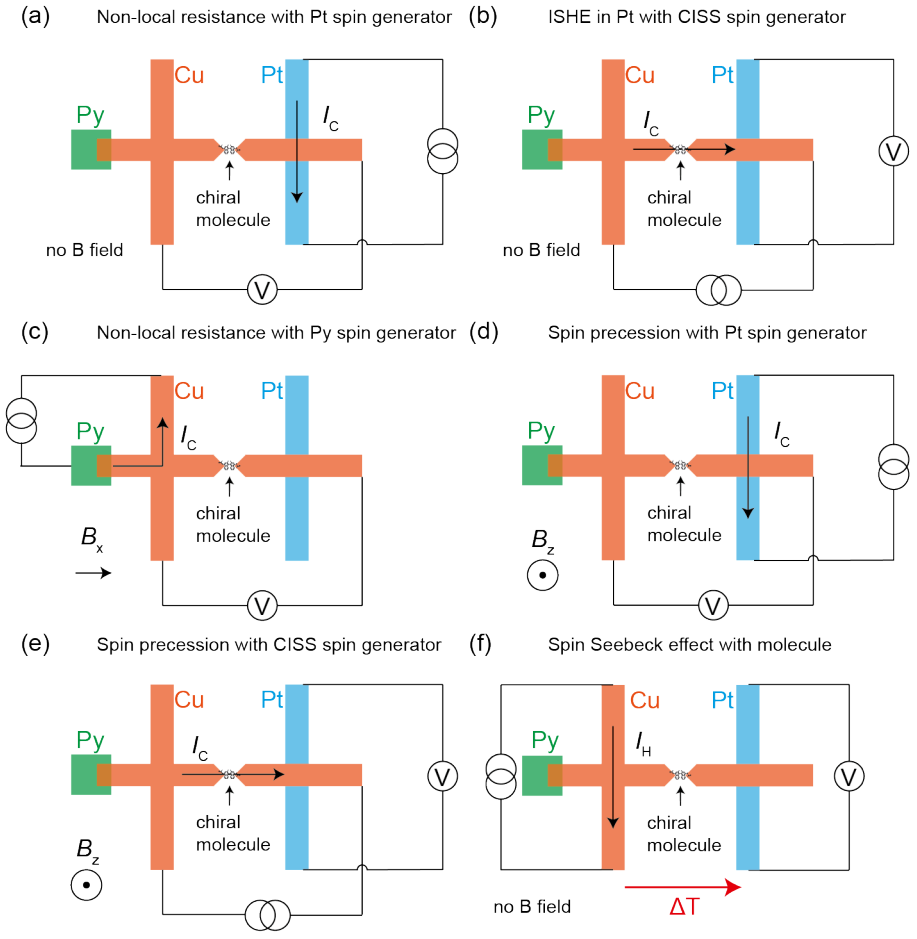

Figure 7.13: Four-terminal nonlocal measurement schemes for the CISS effect. (a) Non-local resistance measurement with a Pt spin generator and CISS spin detector. (b) Non-local resistance measurement with a CISS spin generator and Pt spin detector. (c) Non-local resistance measurementwith a Py spin generator and CISS spin detector. (d) Spin precession measurement with a Pt spin generator and CISS detector. (e) Spin precession measurement with a CISS spin generator and Pt spin detector. (f) Spin Seebeck effect on the CISS molecule with a Pt spin detector.

case of Fig. 7.13a. In this case, we use the Py pad as the spin generator. The spin current diffuses across the chiral molecule and gets filtered depending on its polarization. This again gives different voltages between the two spin species, when the magnetization of Py is switched by the in-plane field B_x.

Figures 7.13d and e are measurement schemes very similar to the cases of Fig. 7.13a and b, respectively, but with the application of an external perpendicular magnetic field, B_z. This magnetic field allows us to probe the spin precession,

which occurs due to the presence of a perpendicular magnetic field to the spin polarization [4]. In both cases, we expect oscillations in the detected voltage as a function of external magnetic field, indicating the presence of spin precession [44].

Another measurement scheme incorporates the thermoelectric studies of molecules shown in Chap. 5 and 6 is shown in Fig. 7.13f. In this case, we apply a large heater current to the Cu strip to generate a temperature gradient across the chiral molecule. This leads to the generation of a thermocurrent across the single molecule. With the spin-filtering property of the chiral molecule, a higher population of right-pointing thermo-spin-current enters the Pt strip. *Via* the ISHE, this creates a charge current, thus a voltage difference, on the Pt strip.

Approximation of non-local resistances

To gain more insight into the expected experimental non-local resistance in the aforementioned 4T measurement schemes, we take a crude expression for a reversible spin hall junction [45], for the configurations of Figs. 7.13a-b:

$$R_{\mathrm{SH}} \approx \frac{1}{2}\alpha_{\mathrm{SH}} P_{\mathrm{S}} R_s^{\mathrm{NM}} e^{-x_{\mathrm{SH}}/\lambda_s^{\mathrm{NM}}}, \tag{7.4}$$

where α_{SH} is the spin Hall angle, P_{S} is the polarization of the spin current injected by a ferromagnet, λ_s^{NM} is the spin diffusion length, x_{SH} is the distance between spin injector and detector, $R_s^{\mathrm{NM}} = \lambda_s^{\mathrm{NM}}/\sigma_{\mathrm{NM}} A_{\mathrm{NM}}$ is the spin resistance of the normal metal, A_{NM} is the cross-sectional area of the normal metal. This equation is most applicable to device geometry shown in Fig. 7.11a without the presence of a molecule.

For the approximation of the non-local CISS signal, we substitute the spin polarization by a ferromagnet, P_{S}, with the spin polarization caused by the CISS effect and keep the remaining variables unchanged. Here, we take $\alpha_{\mathrm{SH}} = 0.1$ of an average platinum spin Hall angle [5]; $P_{\mathrm{S}} = 0.1$ for a spin polarization of 10% caused by CISS, as most experimental reports have claimed that polarization to be tens of percent; $x_{\mathrm{SH}} = 100\ \mathrm{nm}$ for the distance between the molecule and Pt arm; $\lambda_s^{\mathrm{NM}} = 500\ \mathrm{nm}$ for the spin diffusion length of Cu [5]; $A_{\mathrm{NM}} = 4.5 \times 10^{-15}\ \mathrm{m}^2$ for a junction with a width of 100 nm and a thickness of 45 nm. This gives us a non-local resistance of:

$$R_{\mathrm{SH}} = 7.6\ \mathrm{m\Omega}. \tag{7.5}$$

In the case of Fig. 7.13a, if we source a charge current of $I = 10\ \mathrm{mA}$ across the Pt arm, with the Ohm's law $V = IR$, we expect a non-local voltage of $V = 76\ \mu\mathrm{V}$. This signal level is sufficient to be detected with the DC reversal current mode [38] or a lock-in amplifier. We note that this is under the assumption of a transparent interface between the molecule and Cu bridge, which allows the spin current to pass through with little resistance. For a better approximation of the spin signal in a molecular junction, it will require a sophisticated theoretical model. In the case of Fig. 7.13b, we can source a charge current across the molecule, which is in the range of a few nA for a bias voltage of 1 V. For example, the current in a short-BINAP junction, whose off-resonance resistance is around $G = 10^{-5} G_0$, at 1 V can

be estimated as: $I = 1 \times 10^{-5} \times G_0 \approx 0.75$ nA. This gives a non-local voltage of $R_{\mathrm{SH}} \approx 6 \times 10^{-12}$ V, which is much below the electrical detection limit.

For the case of Fig. 7.13c, we can also write equation similar to Eq. 7.4 [45]:

$$R_{\mathrm{nl}} = \pm\frac{1}{2} P_{\mathrm{D}} P_{\mathrm{S}} R_s^{\mathrm{NM}} e^{-x_{\mathrm{D}}/\lambda_s^{\mathrm{NM}}}, \tag{7.6}$$

where P_{D} is the spin polarization of the ferromagentic spin detector, (+) and (-) signs correspond to parallel and antiparallel configurations of the electrode magnetization to the spin filtering direction of the chiral molecule; x_{D} is the distance between the Py spin injector and the molecule. Taking a $P_{\mathrm{D}} = 0.5$ for the Py spin injector, $x_{\mathrm{D}} = 200$ nm, with other parameters used in the previous example, we obtain a non-local resistance of: $R = 31$ mΩ. With a source current of $I = 10$ mA, this gives us: $R_{\mathrm{nl}} = 0.31$ mV. Similarly, this value is ample for the electrical detection, provided that the interface between the molecule and Cu is transparent and allows for high spin current.

For Figs. 7.13d and e, we cannot draw a simple estimate for the precession signals, but the zero-field non-local resistance should be the same as in the case of 7.13a and b. For the case of Fig. 7.13f, the size of the Seebeck effect will depend large on the derivative of the transmission function of the molecular junction, as discussed in Sec.2.3.3. Therefore, the size of the CISS signal will also largely depend on the transmission of the molecular junction.

In summary, configurations in Figs. 7.13a and c are plausible geometries for the CISS measurements. However, as mentioned above, the approximation made here is overly simplified, as no consideration of the molecule-electrode interface or junction geometry has been included. Therefore, the approximation made here is only for comparing different configurations, and there can be major differences between the values determined above and the real experimental results. To experimentally improve the non-local signals in the molecular junction, it is helpful to gate the molecular level closer to the Fermi energy. In the ideal scenario, this will bring the conductance of the molecular junction closer to G_0, as a perfectly transmitting channel. This, for example, can increase the signal in configuration b by a few orders of magnitude.

7.5. Conclusion

The CISS effect in organic molecules is a puzzling problem in the field of molecular electronics and spintronics. The large discrepancy between experiment and theory may be a result of improper techniques in the experiments and missing ingredients in the theoretical work of the CISS effect. Therefore, we have explored the possibility to experimentally study the CISS effect at the single-molecule level.

In chapter, we have characterized three different classes of chiral molecules for the CISS effect studies with the MCBJ technique: Helicene, PDI and BINAP. We found that BINAP-based molecules show good conductance levels and clear molecular plateaus, which are important factors for the single-molecule CISS studies. To properly investigate the CISS effect, we have proposed a few device designs which support multi-terminal non-local measurements for the CISS effect. The RSHJ and

LSV-RSHJ are promising candidates and we have reported the full fabrication details of these novel devices for single-molecule studies. At the time of writing, we are still working the optimization of the Ar milling recipe of RSHJ for a detectable spin signal. Regarding future single-molecule measurements of the CISS effect, we have discussed the possibility to use a 2T measurement scheme for the CISS characterization, and we have also proposed a few new 4T non-local measurement schemes for the single-molecule CISS effect.

For future work, it is crucial to perform single-molecule measurements with a chiral molecule inside the RSHJ and LSV-RSHJ devices. While it is not clear if the signals in these devices will be strong enough to be measured, it is still an important step towards understanding the CISS effect. An added value of these device geometries is the possibility to study the inorganic, crystalline version of the CISS effect demonstrated in the recent reports [42, 43, 46, 47]. Although the connection of it to the organic-molecule CISS effect we aim to study is not clear, it certainly will enrich our understanding of how the breaking of mirror symmetry changes the microscopic charge and spin transport in a system. Perhaps, with the knowledge of the interplay between chirality and spin, novel materials can be designed for future applications, and a better understanding of the naturally occurring chirality in living organisms can be achieved.

7.6. Appendix

7.6.1. Fabrication steps

H-bar Platinum junction

The fabrication of H-bar-Pt devices follows standard electron-beam lithography processes. Below, we describe the fabrication processes step by step.

1. Cleaning a SiO_2/Si substrate with hot acetone at 50°C for 10 min, and rinsing it with isopropanol alcohol (IPA) for 30s.
2. Oxygen plasma cleaning at 300 W for 3 min.

■ Alignment markers

3. Spin coating MMA 8.5 EL8 and PMMA 950 A2 both at 4000 rpm with a baking time of 3 min each at 190°C.
4. Electron-beam patterning for alignment markers with a dose of 1050 $\mu C/cm^2$ at an acceleration voltage of 100 keV.
5. Development in MIBK:IPA with 1:3 ratio for 90 s and stopping in IPA for 30 s.
6. electron-beam evaporation of Ti/Au with thicknesses of 5/60 nm, followed by lift-off in hot acetone at 50°C.

■ Pt strips

7. Oxygen plasma cleaning at 300 W for 3 min.
8. Spin coating PMMA 495 K A3 at 3000 rpm and PMMA 950 A2 at 1500 rpm, both with a baking time of 3 min at 190°C.
9. Electron-beam patterning for Pt strips with a dose of 1250 $\mu C/cm^2$ at an acceleration voltage of 100 keV.
10. Development in MIBK:IPA with 1:3 ratio for 90 s and stopping in IPA for 30 s.
11. electron-beam evaporation of Pt with a thickness of 15 nm, followed by lift-off in hot acetone at 50°C.

■ Cu structures and contact pads

12. Spin coating PMMA 495K A3 at 3000 rpm and PMMA 950K A2 at 1500 rpm, both with a baking time of 3 min at 190°C.
13. Electron-beam patterning for Cu structures with a dose of 1250 $\mu C/cm^2$ for small features and 1050 $\mu C/cm^2$ for large features, at an acceleration voltage of 100 keV.
14. Development in MIBK:IPA with 1:3 ratio for 90 s and stopping in IPA for 30 s.
15. Electron-beam evaporation of Cu with a thickness of 45 nm, followed by lift-off in hot acetone at 50°C.

Reversible spin Hall junction

The fabrication steps of RSHJ have been changed many times through the process of device optimization. Here, we show the latest fabrication steps of RSHJ.

1. Hot acetone cleaning for a SiO_2/Si (oxide thickness of 817 nm) at 50°C for 10 min, followed by rinsing in IPA for 2 min.

2. Oxygen plasma cleaning (TEPLA) at 600 W with a flow rate of 200 sccm for 5 min.

■ Alignment markers and contact pads

3. Spin coating PMMA 495K A6 at 3000 rpm with hot-plate baking at 190°C for 3 min. This gives a resist thickness of about 350 nm.

4. Spin coating PMMA 950K A8 at 3000 rpm with hot-plate baking at 190°C for 15 min. This gives a resist thickness of about 600 nm.

Note: The choice of the thick resist layer is for the reactive ion etching (RIE) step performed later.

5. Electron-beam patterning for markers and contact pads with a dose of 1200 $\mu C/cm^2$ at an acceleration voltage of 100 keV.

6. Development in MIBK:IPA with 1:3 ratio for 90 s and stopping in IPA for 30 s.

7. RIE etching (Sentech) for 5 min: RF power =50 W, P =100 μbar CHF_3=25 sccm, Ar 25 sccm. Typical bias voltage is around -200 V. This gives an etched depth of 42 nm.

8. Electron-beam evaporation of Ti/Au with thicknesses of 3/52 nm, followed by lift-off in hot acetone at 50°C.

Note: This gives a marker and contact height of around 13 nm above the SiO_2 surface, which is smaller than the later deposited Cu structures, so that the electrical contact between Cu and Au can be properly made. Importantly, this helps the wirebonding in the final stage of sample packaging, because Cu is proved to be hard to wirebond in ambient conditions [48]. It also helps to improve the interface between Cu and Au in comparison to depositing Au on top of Cu, because Au does not oxidize easily.

■ Pt strips

9. Oxygen plasma cleaning (TEPLA) at 600 W with a flow rate of 200 sccm for 5 min.

10. Spin coating AR-P 6200-09 (CSAR) at 2000 rpm, followed by hot-plate baking at 180°C for 3 min. This gives a resist thickness of about 280 nm.

11. Electron-beam patterning for Pt strips with a dose of 450 $\mu C/cm^2$ at an acceleration voltage of 100 keV.

12. Development in Pentyl acetate for 60 s, xylene for 5 s and stopping in IPA for 30 s.

13. Electron-beam evaporation of Pt with a thickness 15 nm, followed by lift-off in anisole at 80°C.

14. Post-lift-off cleaning with acetone at 50°C and IPA.

■ Py structures

Note: No plasma cleaning is used starting from this step to prevent any additional oxidation of the metals.

15. Spin coating AR-P 6200-09 (CSAR) at 2000 rpm, followed by hot-plate baking at 180°C for 3 min. This gives a resist thickness of about 280 nm.

16. Electron-beam patterning for Py structures with a dose of 450 $\mu C/cm^2$ at an acceleration voltage of 100 keV.

17. Development in Pentyl acetate for 60 s, xylene for 5 s and stopping in IPA for 30 s.

18. Electron-beam evaporation of Py with a thickness 30 nm, followed by lift-off in anisole at 80°C.

19. Post-lift-off cleaning with acetone at 50°C and IPA.

■ Cu structures

20. Spin coating PMMA 495K A6 at 4000 rpm and PMMA 950K A4 at 1500 rpm. Both are hot-plated baked at 190°C for 3 min. This gives thicknesses of 300 nm + 300 nm.

21. Electron-beam patterning for Cu structures with a dose of 1600 $\mu C/cm^2$ for the fine structures and 1200 $\mu C/cm^2$ for the large structures at an acceleration voltage of 100 keV.

22. Development in MIBK:IPA with 1:3 ratio for 90 s and stopping in IPA for 30 s.

23. Post-development baking on a hot plate at 190°C for 1 min to remove excess solvent.

24. Ar ion milling in the evaporator for 10 s. RF power=150 W, beam voltage =500 V, acceleration voltage =250 V, neutralizer current =100 mA, pressure $=7.5 \times 10^{-4}$ mbar. To get the optimal milling parameters a few factors need to be considered on-site, the details can be found in Sec. 7.6.2.

25. Electron-beam evaporation of Cu with a thickness 45 nm, followed by lift-off in acetone at 50°C.

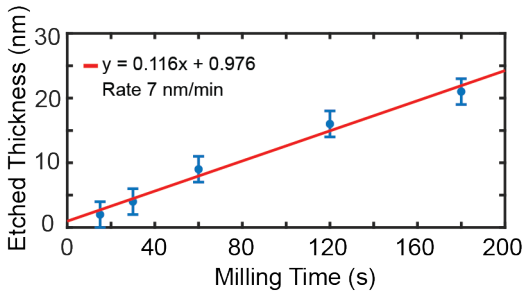

Figure 7.14: Ar milling rate obtained by AFM height measurements as a function of milling time.

7.6.2. Argon ion milling on Permalloy

To gain a transparent interface between Cu and Py, *in-situ* Ar ion milling is typically employed right before the deposition of Cu. The exact process condition is usually not documented in the literature as it may differ substantially between different milling machines. In a previous report also by Kimura *et. al.* [49], it has been shown that the spin signal can be greatly improved by optimizing the milling recipe. Here, we try to optimize the milling process by adjusting the milling time and keeping the same controlled process condition. We created a preliminary manual/recipe, which is described below and is specific to the AC-EVA 450 miller-evaporator used in the Kavli nanoscience cleanroom.

1. Loading the sample and start the vacuum. Rotate the sample to face up (sample surface parallel to the miller).
2. As vacuum reaches 5×10^{-6} mbar in the load-lock, start VG21 and VG11, by pressing '+' and 'start'.
3. Adjust the flow to VG21 =3 sccm and VG11 =6 sccm. VG21 is the Ar gas input for the plasma source and V21 is the Ar gas input for the neutralizer.
4. Wait until the pressure is stabilized, which is typically around $P = 7.5 \times 10^{-4}$ mbar.
5. Switch on the RF power and set to 150 W.
6. Switch off VG11 and wait until the pressure is stablized.
7. Switch on VG11 again.

Note: By switching VG11 off and back on, we create a burst of pressure, which is essential to ignite a plasma. The plasma should now be on, signified by the light blue glowing light in the load-lock chamber.

8. Wait 5 min for plasma stabilization.
9. Turn on controllers for beam current, neutralizer and accelerator in order.

10. Set the controllers to the desired values. In our recipes, two different configurations have been used:

    (a) Beam voltage =500 V (Beam current =38 mA), acceleration voltage =100 V (acceleration current =18 mA) and neutralizer current =124 mA.

    (b) Beam voltage =500 V (Beam current =30 mA), acceleration voltage =250 V (acceleration current =8 mA) and neutralizer current =100 mA.

    Both recipes have shown to work in doses test up to 15 s. However, in the real devices, there has been a lift-off problem after employing recipe (a). This is understood as a problem with the directionality of Ar ion in the milling process. Therefore, a higher acceleration voltage is chosen in (b) to achieve better directionality.

11. Stop the 3 controllers and rotate the sample to face the miller.

12. Switch on the three controllers in the order of beam current, neutralizer and accelerator. Wait for the desired time. In the case of a real device, 10 s is typically used.

13. Switch off the three controllers and the RF power when the time is up.

14. Wait 2 min and switch off VG21 and VG11.

    The sample is then ready for Cu evaporation.

There are a few key parameters in the milling process: pressure, voltage and time, which we will discuss in the following paragraphs. A high process pressure typically means a higher milling rate, as more ions can bombard the sample surface. However, excess pressure can greatly reduce the ion directionality, which is bad for the lift-off after the evaporation. In the case of this system (EVA-450), the pressure cannot be reduced much lower than $P = 7.5 \times 10^{-4}$ mbar because the plasma can quench with a low process pressure.

As briefly mentioned in the recipe, the acceleration current (created by the combination of acceleration voltage and beam voltage) is an important indicator for the directionality of the milling process. An intuitive way see this is the following: A high acceleration current indicates that many accelerated ions hit the acceleration grid, instead of passing through it. To achieve low acceleration current, we can either increase the the acceleration voltage or reduce the pressure (as mentioned above). In fact, both have been attempted: First, in step 10, a higher acceleration voltage has been used in (b), which gives a much lower acceleration current. Second, when we attempted to gradually reduce the flow rate of VG11 until 5 sccm, this reduces the pressure to around 6×10^{-4} mbar and gives an acceleration current of 6 mA. However, the second method seems to be create a problem in the stability of the plasma, meaning that in some cases the plasma will quench due to the low process pressure.

The time dependence of the milling process is the main focus of this optimization study. In particular, we quantify the milling rate of the Ar ions on a specific surface.

With the settings of 10(a) we observed that the milling rate of PMMA 950K is about 12 nm/min and the resist layer started to crack due to overheating for milling time above 3 minutes. This suggests that, with the resist layer (300 nm) we use, the resist is sufficient for a milling process below 3 minutes. To quantify the Ar milling rate on the Py surface, we performed the milling processes over a few samples with pre-deposited Py layers, whose etched thicknesses were measured with AFM. This is summarized in Fig. 7.14, where a milling rate of around $7\ \mathrm{nm/min}$ is determined. This suggests that, for the removal of a native oxide thickness of 2 to 3 nm on Py [50], a Ar milling time of Py surface around 17 to 25 s is required. We note that this rate is an estimate as the milling rate of the oxide layer should not be identical to the that of pure Py; however, as no clear rate change (change of slope) is observed in Fig. 7.14, we assume the milling rate of the top oxide layer is approximately the same to that of Py metal beneath.

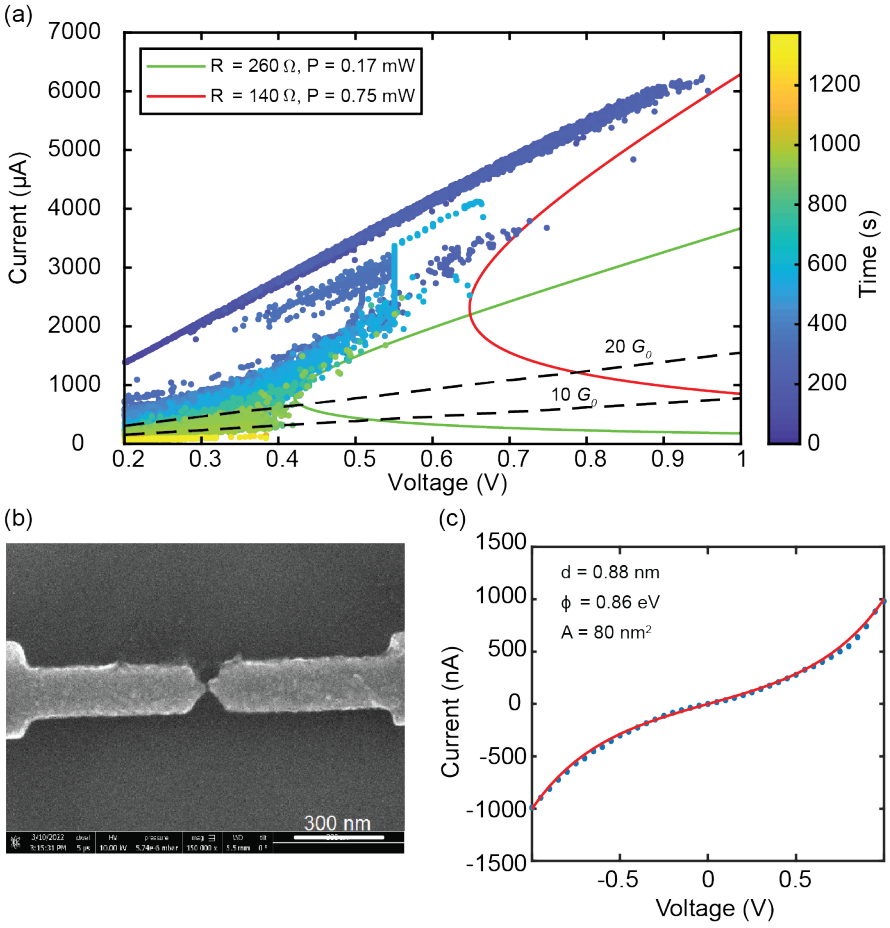

Figure 7.15: (a) Feedback controlled electromigration curve. The *IV* of the junction follows a concave shape of a constant power at 0.75 mW in the beginning of the EM and later at 0.17 mW. (b) SEM image of the EMBJ after electromigration. (c) *IV* characteristics of the EMBJ after electromigration. With the Simmons model, a nanogap with a size of 0.88 nm is determined. Figures are adapted from Ref. [39].

7.6.3. Electromigration of copper

An important element in the realization of the aforementioned single-molecule junctions for spin generation and detection is the electromigration of the Cu EMBJ bridge. Importantly, it is essential to create a reproducible and stable nanogap after electromigration, which is particularly difficult in the case of Cu metals [41]. Therefore, we have performed a series of optimization experiments for in the electromigration process to obtain protocol for creating sub-nm gaps for contact single molecules.

The optimization and characterization are extensively discussed in the thesis of S. Golightly in Ref. [39]. Here, we provide an overview of a few main results in the

Cu electromigration experiments. In these EM experiments, we use a homemade graphic user interface (GUI) which controlled the ADwin processor/controller for the feedback controlled EM, as also discussed in Sec. 2.2. With the feedback control, we successfully electromigrated Cu EMBJ reproducibly with the protocol described below:

1. Load the EMBJ device and pump the vacuum chamber to a pressure below $P = 10^{-3}$ mbar.
2. For the initializing the EM process, ramp the bias voltage across the EMBJ up from 200 mV at a rate of 300 to 500 mV/min until an observation of change in resistance. Quickly reduce the voltage back to 200 mV when the instantaneous change of resistance, $(dR/dt)/R$, is above 1%. Here, dR/dt is the change of resistance between two consecutive resistance measurements. For a successful EM, it is important not to exceed a voltage above 1 V.
3. Increase the voltage from 200 mV again until an observation of resistance increase. This time, we adjust the cut-off criterion, $(dR/dt)/R$, to approximately 2%. Similarly, when this criterion is reached, quickly reduce the voltage back to 200 mV.
4. Repeat the previous step until reaching a resistance of a around 1 kΩ. Afterwards, continue the EM process but keep the bias voltage low (<500 mV) until the desired resistance value is reached (typically corresponds to a conductance value of a few G_0).
5. The EM GUI will stop automatically when the desired resistance reached and the EMBJ is read for use.

An example of EM process with the above-described protocol is shown in Fig. 7.15a. Here, we can see that the initial breaking of the junction follows a constant power curve of 0.75 mW and later changes to that of 0.17 mW as the total junction resistance increases. This type constant power curve is an indication of a good electromigration process[41] and a SEM image of a typical EMBJ after electromigration is shown in Fig. 7.15b. Here, due to the resolution limitation, the gap below a few nm cannot be resolved; therefore, a fitting to the Simmons's model [51] is used to extract the nanogap size. Fig. 7.15c shows an example of a tunneling *IV* of an electromigrated nanogap with a size of around 0.9 nm. This nanogap size is ideal for the Short-BINAP chiral molecule which we will used for the CISS characterization.

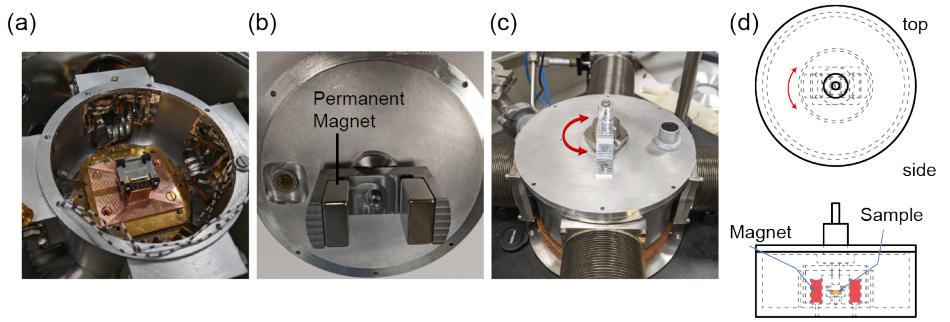

Figure 7.16: (a)-(c) Room temperature in-plane magnet setup. (a) Base of the vacuum probe station, which is now as a sample mount. (b) Permanent magnets, which are mounted on to a Fe-based magnet yoke, and attached to a vacuum rotary feedthrough. (c) Outside view of the set-up. The vacuum rotary feedthrough can freely rotate round the z-axis. (d) Schematic drawing of the setup, provided by Ronald Bode at TU Delft.

7.6.4. Room temperature in-plane magnet set-up

To achieve an in-plane magnetic field, we need a system where the sample or the magnet can rotate freely around the z-axis. There are a few options which are commercially available, including superconducting vector magnets, piezo-actuated rotating sample stages, electromagnets or Helmholtz coils. All these options are expensive and are not readily available in the laboratories. Therefore, we designed a simple setup where an in-plane rotating magnetic field is possible by using commercially available permanent magnets, together with Ronald Bode, a mechanical technician at TU Delft. Here, we use grade N52 Neodymium magnets (NdFeB) from K&J Magnetics to introduce external magnetic at room temperature. The magnets are mounted to a vacuum rotary feedthrough from BeamTec, which provides the possibility to rotate the magnets freely under a high vacuum. The actual set-up is shown in Fig. 7.16a-c. In simple terms, the sample can be mounted in the chip carrier holder shown in center of Fig. 7.16a. The sample can be magnetized by the NdFeB magnets shown in Fig. 7.16b, which can freely rotate around the z-axis as shown in Fig. 7.16c. A schematic drawing can also be found in Fig. 7.16d.

There are a few advantages of this setup: First, the total cost of the setup is only around 1000 euro, which is much cheaper in comparison to commercial electromagnets, which are in the range of a few tens of thousand euro. Second, with the large air gap (3 cm) for the sample space, we can achieve an estimated magnetic field of 3000 Gauss (sufficient to switch the magnetization), which is not possible in a commercially available Helmholtz coil. Third, the setup operates at room temperature without the need of cryogenic liquid, and also at low temperature if necessary. This is much more convenient than maintaining a liquid-helium cooled superconducting magnet.

The expected measurement outcome for spin generation and detection without molecules is similar to the plot of Fig. 7.11b, with the x-axis replaced by rotation angle.

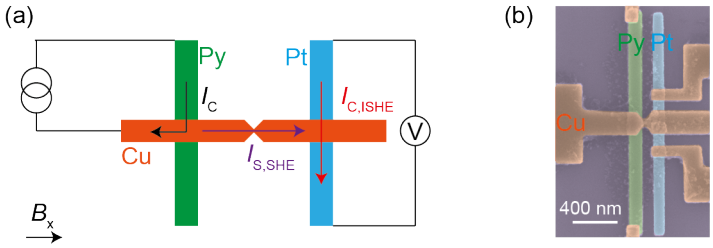

Figure 7.17: (a) Schematic drawing of LSV-RSHJ. (b) False-colored SEM image of a LSV-RSHJ device.

7.6.5. Lateral spin valve based RSHJ

In the original study of reversible spin hall device by Kimura *et. al.* [37], the non-local signal detected is around 100 μΩ. Also also shown in same study, the non-local signal increases as the junction length decreases, reaching a maximum of 150 μΩ at distance of 200 nm between the Py pad and Pt arm. This decay is readily explained by spin relaxation, when a spin current is propagating through the Cu junction. Therefore, it is intuitive to make the distance between Py and Pt as small as possible for an optimal non-local signal. A lateral spin valve based geometry was also studied by T. Kimura and coworkers [52], where the Py spin generator is placed parallel to the Pt spin detector. This geometry with a EMBJ constriction, which we refer as lateral spin valve based RSHJ (LSV-RSHJ), is shown in Fig. 7.17a. Similar to the design in Fig. 7.11c, the charge currents goes from Py to Cu to generate a spin current across the Cu bridge, which diffuses to the Pt strip. This in turn creates a charge current *via* the ISHE in Pt, which is detected as a voltage difference across the Pt arm.

A major difference between the RSHJ and LSV-RHSJ is that, in this fashion, the Py and Pt arms can be placed closer to each other. Indeed, a higher non-local resistance of around 300 μΩ was observed by T. Kimura and coworkers [52], as a result of a closer ($L \approx 100$ nm) distance between the spin generator and detector. Another benefit of this geometry is the potentially easier electromigration, comparing to the RSHJ. For good electromigration, it is important to avoid any interface between different materials, as interfaces are typically more resistive than a pure metallic structure. This can lead to electrical failure at the junction interface, instead of proper electromigration. Therefore in the case of RSHJ, we need to take and 'L-shape' Cu path for electromigration on the left-hand side for good electromigration. This is less desirable for the narrow Cu arm, when it is compared with the case of LSV-RSHJ with a large bridge-to-constriction ratio.

Nonetheless, there are a few drawbacks of the LSV-RSHJ. First, the magnetization field ruired is around 3000 Gauss, which is more than 10 times larger than the field in the case of RSHJ. This is due to the small dimension of the Py strip in the x-direction. As mentioned in Sec. 7.6.4, the estimated external magnetic field that can be generated in the set-up in Fig. 7.16 is approximately 0.3 T. This may not be sufficient to completely magnetize the Py strip in some cases, as some deviation

may exist in fabricated devices. Another challenge in this device geometry is the alignment of the EMBJ between Py and Pt. The precision of position in the electron-beam pattern generator (EBPG5000+) is typically around tens of nm. This means in some rare cases, the EMBJ might be outside of the region between the Py and Pt strips. For example, a small misalignment is observed in the case of Fig. 7.17b, where the constriction is located slightly closer to the Py arm. In this respect, the RSHJ is more robust to this misalignment as the EMBJ and Cu strip are patterned in the same electron-beam exposure.

Considering the pros and cons of the LSV-RSHJ, it is useful to simultaneously fabricate RSHJ and LSV-RSHJ on the same sample for maximal device yield. Therefore, we have incorporated both designs on the same substrate following the same lithographic steps.

Four-terminal measurement in LSV-RSHJ

In addition to the 4T measurement schemes discussed in Sec. 7.4.2, mostly for RSHJ, we can also perform the same measurements for the LSV-RSHJ. This is summarized in Fig. 7.18. There are a few differences between the measurement schemes of RSHJ and LSV-RSHJ, which need to be considered. First, in the cases of a, b and f, it is important avoid any unintentional magnetization in Py, because the unwanted magnetization of Py can contribute to the spin signals, which can affect the CISS measurement outcome. Another potential issue is present in the case of d and e. This is because by applying an external field for the spin precession measurement, there is also a possibility of magnetizing the Py strip out of plane, which will completely diminish the spin precession signal.

Figure 7.18f is potentially a better than the RSHJ geometry. This is because if we used the Cu strip in RSHJ as a heater, there is a electrical pathway connected to the molecule. In the case of a Py junction without a Ar milling step, the observed resistance between Py and Cu is beyond $R = 5\mathrm{G}\Omega$. This means that, we can use Py strip as a heater in this case without introducing electrical interference, and due to the thin oxide layer between Cu and Py, the heating efficiency is expected to be high.

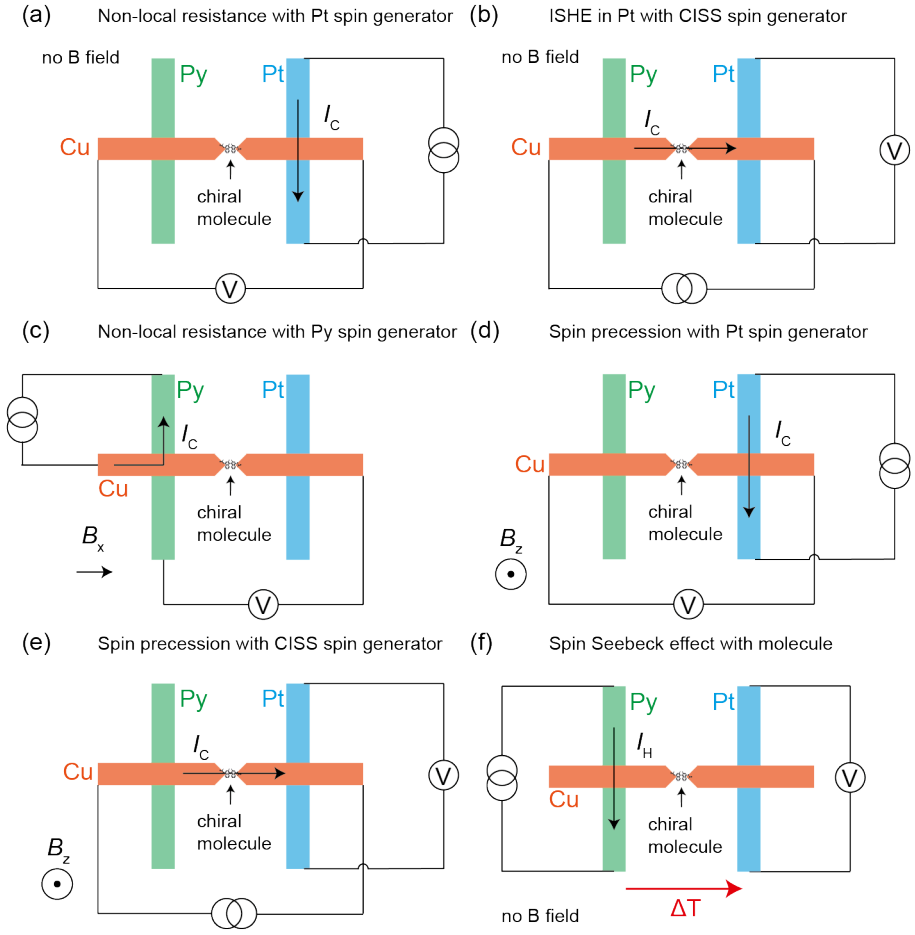

Figure 7.18: Four-terminal non-local measurement schemes for the CISS effect in LSV-RSHJ devices. (a)-(f) The same measurement working principles as in Fig. 7.13 in the main text.

References

(1) Wolf, S. A.; Awschalom, D. D.; Buhrman, R. A.; Daughton, J. M.; von Molnár, S.; Roukes, M. L.; Chtchelkanova, A. Y.; Treger, D. M. *Science* **2001**, *294*, 1488–1495.

(2) Hirohata, A.; Yamada, K.; Nakatani, Y.; Prejbeanu, I.-L.; Diény, B.; Pirro, P.; Hillebrands, B. *Journal of Magnetism and Magnetic Materials* **2020**, *509*, 166711.

(3) Rajput, P. J.; Bhandari, S. U.; Wadhwa, G. *Silicon* **2022**.

(4) Žutić, I.; Fabian, J.; Sarma, S. D. *Reviews of Modern Physics* **2004**, *76*, 323–410.

(5) Sinova, J.; Valenzuela, S. O.; Wunderlich, J.; Back, C. H.; Jungwirth, T. *Reviews of Modern Physics* **2015**, *87*, 1213–1260.

(6) Göhler, B.; Hamelbeck, V.; Markus, T. Z.; Kettner, M.; Hanne, G. F.; Vager, Z.; Naaman, R.; Zacharias, H. *Science* **2011**, *331*, 894–897.

(7) Naaman, R.; Waldeck, D. H. *The Journal of Physical Chemistry Letters* **2012**, *3*, 2178–2187.

(8) Xie, Z.; Markus, T. Z.; Cohen, S. R.; Vager, Z.; Gutierrez, R.; Naaman, R. *Nano Letters* **2011**, *11*, 4652–4655.

(9) Kiran, V.; Mathew, S. P.; Cohen, S. R.; Hernández Delgado, I.; Lacour, J.; Naaman, R. *Advanced Materials* **2016**, *28*, 1957–1962.

(10) Ben Dor, O.; Yochelis, S.; Radko, A.; Vankayala, K.; Capua, E.; Capua, A.; Yang, S.-H.; Baczewski, L. T.; Parkin, S. S. P.; Naaman, R.; Paltiel, Y. *Nature Communications* **2017**, *8*, 14567.

(11) Kettner, M.; Göhler, B.; Zacharias, H.; Mishra, D.; Kiran, V.; Naaman, R.; Fontanesi, C.; Waldeck, D. H.; Sęk, S.; Pawłowski, J.; Juhaniewicz, J. *The Journal of Physical Chemistry C* **2015**, *119*, 14542–14547.

(12) Aragonès, A. C.; Medina, E.; Ferrer-Huerta, M.; Gimeno, N.; Teixidó, M.; Palma, J. L.; Tao, N.; Ugalde, J. M.; Giralt, E.; Díez-Pérez, I.; Mujica, V. *Small* **2017**, *13*, 1602519.

(13) Mondal, P. C.; Fontanesi, C.; Waldeck, D. H.; Naaman, R. *Accounts of Chemical Research* **2016**, *49*, 2560–2568.

(14) *The Journal of Physical Chemistry Letters* **2018**, *9*, 2025–2030.

(15) Zöllner, M. S.; Varela, S.; Medina, E.; Mujica, V.; Herrmann, C. *Journal of Chemical Theory and Computation* **2020**, *16*, 2914–2929.

(16) Dalum, S.; Hedegård, P. *Nano Letters* **2019**, *19*, 5253–5259.

(17) Liu, Y.; Xiao, J.; Koo, J.; Yan, B. *Nature Materials* **2021**, *20*, 638–644.

(18) Gersten, J.; Kaasbjerg, K.; Nitzan, A. *The Journal of Chemical Physics* **2013**, *139*, 114111.

(19) Fransson, J. *The Journal of Physical Chemistry Letters* **2019**, *10*, 7126–7132.

(20) Yang, X.; van der Wal, C. H.; van Wees, B. J. *Physical Review B* **2019**, *99*, 024418.

(21) Yang, X.; van der Wal, C. H.; van Wees, B. J. *Nano Letters* **2020**, *20*, 6148–6154.

(22) Huisman, K. H.; Thijssen, J. M. *The Journal of Physical Chemistry C* **2021**, *125*, 23364–23369.

(23) Hsu, C. *Master thesis, TU Delft* **2018**.

(24) Cabosart, D.; El Abbassi, M.; Stefani, D.; Frisenda, R.; Calame, M.; van der Zant, H. S. J.; Perrin, M. L. *Applied Physics Letters* **2019**, *114*, 143102.

(25) Xu, B.; Xiao, X.; Yang, X.; Zang, L.; Tao, N. *Journal of the American Chemical Society* **2005**, *127*, 2386–2387.

(26) Henze, S.; Bauer, O.; Lee, T.-L.; Sokolowski, M.; Tautz, F. *Surface Science* **2007**, *601*, 1566–1573.

(27) Hoffmann, A. *IEEE Transactions on Magnetics* **2013**, *49*, 5172–5193.

(28) Dyakonov, M.; Perel, V. *Physics Letters A* **1971**, *35*, 459–460.

(29) Hirsch, J. E. *Physical Review Letters* **1999**, *83*, 1834–1837.

(30) Valenzuela, S. O.; Tinkham, M. *Nature* **2006**, *442*, 176–179.

(31) Wunderlich, J.; Kaestner, B.; Sinova, J.; Jungwirth, T. *Physical Review Letters* **2005**, *94*, 047204.

(32) Kato, Y. K.; Myers, R. C.; Gossard, A. C.; Awschalom, D. D. *Science* **2004**, *306*, 1910–1913.

(33) Chen, C.; Tian, D.; Zhou, H.; Hou, D.; Jin, X. *Physical Review Letters* **2019**, *122*, 016804.

(34) De Jong, C. G. H. *Master thesis, TU Delft* **2020**.

(35) Abanin, D. A.; Shytov, A. V.; Levitov, L. S.; Halperin, B. I. *Physical Review B* **2009**, *79*, 035304.

(36) Mihajlović, G.; Pearson, J. E.; Garcia, M. A.; Bader, S. D.; Hoffmann, A. *Physical Review Letters* **2009**, *103*, 166601.

(37) Kimura, T.; Otani, Y.; Sato, T.; Takahashi, S.; Maekawa, S. *Physical Review Letters* **2007**, *98*, 1–4.

(38) Daire, A.; Goeke, W.; Tupta, M. A. New Instruments Can Lock Out Lock-ins (Whitepaper), 2005.

(39) Golightly, S. *Master thesis, TU Delft* **2022**.

(40) O'Neill, K.; Osorio, E. A.; van der Zant, H. S. J. *Applied Physics Letters* **2007**, *90*, 2005–2008.

(41) Hoffmann-Vogel, R. *Applied Physics Reviews* **2017**, *4*, 031302.

(42) Shiota, K.; Inui, A.; Hosaka, Y.; Amano, R.; Ōnuki, Y.; Hedo, M.; Nakama, T.; Hirobe, D.; Ohe, J.-i.; Kishine, J.-i.; Yamamoto, H. M.; Shishido, H.; Togawa, Y. *Physical Review Letters* **2021**, *127*, 126602.

(43) Inui, A.; Aoki, R.; Nishiue, Y.; Shiota, K.; Kousaka, Y.; Shishido, H.; Hirobe, D.; Suda, M.; Ohe, J.-i.; Kishine, J.-i.; Yamamoto, H. M.; Togawa, Y. *Physical Review Letters* **2020**, *124*, 166602.

(44) Savero Torres, W.; Sierra, J. F.; Benítez, L. A.; Bonell, F.; Costache, M. V.; Valenzuela, S. O. *2D Materials* **2017**, *4*, 041008.

(45) VALENZUELA, S. O. *International Journal of Modern Physics B* **2009**, *23*, 2413–2438.

(46) Yoda, T.; Yokoyama, T.; Murakami, S. *Scientific Reports* **2015**, *5*, 12024.

(47) Calavalle, F.; Suárez-Rodríguez, M.; Martín-García, B.; Johansson, A.; Vaz, D. C.; Yang, H.; Maznichenko, I. V.; Ostanin, S.; Mateo-Alonso, A.; Chuvilin, A.; Mertig, I.; Gobbi, M.; Casanova, F.; Hueso, L. E. *Nature Materials* **2022**, *21*, 526–532.

(48) Chuang, C.-L.; Aoh, J.-N.; Din, R.-F. *Microelectronics Reliability* **2006**, *46*, 449–458.

(49) Yakata, S.; Ando, Y.; Kimura, T. In *TENCON 2010 - 2010 IEEE Region 10 Conference*, IEEE: 2010, pp 126–128.

(50) Fitzsimmons, M. R.; Silva, T. J.; Crawford, T. M. *Physical Review B* **2006**, *73*, 014420.

(51) Simmons, J. G. *Journal of Applied Physics* **1963**, *34*, 1793–1803.

(52) Vila, L.; Kimura, T.; Otani, Y. *Physical Review Letters* **2007**, *99*, 1–4.

8

Conclusion and Outlook

Conclusion

In this dissertation we have explored important aspects in single-molecule charge transport. In particular, we have considered the orbital and spin degrees of freedom in single-molecule junctions, and their influences in charge transport at the single-molecule level.

In the first part of this dissertation, we studied the conformational effects in single-molecule charge transport. We first discussed mechanically induced quantum interference (QI) features in mechanosensitive molecules, PCPs and PC1. In the case of PCPs, we demonstrated that *para*-connected PCP gives destructive QI (DQI), whereas *meta*-connected PCP gives constructive QI. This shows that the rules of quantum interference in PCPs, in terms of substitution patterns, are different from those in simple benzene rings. We have also studied the DQI features in PC1 molecules. In this case, we observed two DQI dips in the single-molecule junction transmission, as a function of distance. These two dips are a robust feature, as it spans across the full HOMO-LUMO gap, leading to the observation of higher-frequency conductance oscillations in a displacement modulation experiment. In Chapter 4, we studied the two-order-of-magnitude conductance increase during the stretching of PC2 single-molecule junctions. This feature is unique, as no report has so far described such a large conductance up-turn upon stretching in organic molecules. This feature is explained atomistically as a result of a fine balance between through-space and through-bond transport.

The second part of this dissertation concerns the thermoelectric effects in single-molecule junctions. In Chapter 5, we first introduced the simultaneous measurement technique of electrical current and thermocurrent. This has a great advantage, as it allows us to directly obtain thermoelectric parameters, such as the Seebeck coefficient and the power factor. We then applied this technique to study different charge states in a molecular quantum dot. We realized that the asymmetry in thermocurrent between two charge states is a direct measure of the entropy

change between the two states. This provides a means to map the spin transition between two charge states in a radical molecule. Furthermore, in Chapter 6, we utilized the thermocurrent spectroscopy to study the Kondo effect in a single-molecule junction. The Kondo effect is characterized by universal temperature and magnetic-field scaling in the zero-bias peak. However, with conventional electrical measurements, the experimental magnetic-field dependence is inconsistent with the theoretical prediction in most reports. *Via* the thermocurrent spectroscopy, we revealed a new hallmark of the Kondo effect, indicated by a change of slope in zero-bias thermocurrent at a critical field, $B_{\mathrm{th}} = B_{\mathrm{c}}$, same as the critical field in an ideal differential conductance measurement. These experimental findings in thermoelectric studies of single-molecule junctions suggest that there are potential molecule-based thermoelectric device applications; it has also shown that thermocurrent can be used to study fundamental physics problems.

The third part of this dissertation regards the chirality-induced spin selectivity (CISS) effect. The CISS effect is a phenomenon where the spins of electrons are polarized when passing through chiral molecules, as a result of mirror-symmetry breaking. While there are a few experimental observations of the effect, there is a big discrepancy between experiment and theory regarding the size of the effect. There are two main reasons for this discrepancy: First, so far the experiments have been performed on large assemblies of molecules, while the theories focused on single-molecule descriptions. Second, many experimental results are inconclusive and the methodologies used are not proper for spin current detection. To resolve these issues, we have explored single-molecule devices to properly characterize the CISS effect. We first characterized several chiral molecule candidates by the MCBJ technique. We then developed two classes of devices for spin generation and detection at the single-molecule level. Particularly, the reversible spin Hall junction (RSHJ) is a promising platform for performing experiments for the CISS effect. We described the device development and proposed a few measurement protocols for the CISS effect. Although we have not yet completed single-molecule experiments for the CISS effect, the expertise acquired during the development of single-molecule spintronic devices has opened new research directions for nanoscale spintronics.

Outlook

The interplay between charge transport, orbital and spin degrees of freedom has led to many interesting physical phenomena in single-molecule junctions, as we have presented in this dissertation. The research in these systems has deepened our understanding of electron-electron interactions and generated many potential nanoscale applications. These results will be the foundation for our future research in nanoscale and single-molecule systems.

In the first part, we have studied the influence of conformational change on charge transport in single molecules. From this study, we have learned that by fine tuning the molecular design, it is possible to engineer molecular junctions that can act like mechanical switches and sensors. There are a few insights from our studies that facilitate the realization of these applications. 1. The robust mechani-

cally induced DQI feature is an example for a single-molecule "potentiometer" and mechanoelectric sensor. It would be particularly interesting to create a single-molecule junction like the case in PC1, but with two DQI features running parallel to each other. This will give an one-to-one correspondence of the two measured conductance dips and the distance between the two DQI features; therefore, it can serve as a nanoscale ruler. 2. The DQI feature gives a sharp transmission as functions of both distance and energy. This is beneficial for generating high thermopower and potential nanoscale thermoelectric devices. Remarkably, the slope of the transmission function changes its size and sign as we mechanically stretch the molecule. This suggests an universal thermoelectric nanostructure that can be mechanically tuned, which also is a direction of research undertaken. 3. From the switching between through-space and through-bond transport in the case of PC2 molecule, we have recognized that by including a molecular unit such as acetylene in a molecular stack, we can create a mechanical switch for through-space to through-bond transport by mechanical bending. This is yet another demonstration of a mechanical switch molecular design.

In the second part of this dissertation, we have shown the possibility to conduct thermoelectric studies in single-molecule junctions. Particularly, we have demonstrated that we can obtain the complete thermoelectric properties of a nanostructure for applications; we have also observed that fundamental concepts in physics, such as entropy and universality, manifested in thermoelectric characterizations. From the technological point of view, this suggests that we can create thermoelectric devices with nanostructures, such as molecules and nano-particles, whose sizes are smaller than tens of nanometers. Moreover, these single-molecule thermoelectric devices have also shown high thermopower and figure of merit, suggesting possible device applications utilizing molecules. From the fundamental perspective, there are many interesting nanoscale systems which have not yet been studied with thermoelectrics, for example: 1. It is interesting to explore quantum systems with higher spin states *via* thermocurrent spectroscopy. For this, we are exploring new radical molecules with higher spin states in Th-EMBJ. 2. Introducing different physical phenomena, such as superconductivity and the Yu-Shiba-Rusinov state, is another direction of research undertaken. 3. It is also interesting to explore to the possibility of extracting the work out from single-molecule heat engines, which can be used to assess thermodynamic cycles in nanoscale systems.

Lastly, we have explored the possibility to study the CISS effect at the single-molecule level. From the development of single-molecule junctions for spin current detection and generation, we have learned that it is non-trivial to correctly perform a spintronic measurement, particularly in a non-crystalline structure. As the first outlook for this research area, it is most important to integrate the chiral molecules into the RSHJ devices and perform the CISS characterization. This may shed light on the origin of the CISS effect at the single-molecule level. Besides the CISS characterization, a few insights from the research have pointed out possible future directions for molecular spintronic studies. First, the success in electromigration of Cu EMBJ has provided the possibility to study the interaction of chiral, magnetic or nonmagnetic molecules with magnetically proximitized Cu electrodes. This is a

distinct approach from using ferromagnetic EMBJ, as magnetic domains in ferromagnetic nanoelectrodes typically lead to inconsistent results, even in the simple case of direct electron tunneling experiments. Second, the possibility to integrate non-local spintronic measurement geometry in EMBJ devices provides the opportunity to study the spintronic properties of nanostructures in the sizes of a few nanometers. This can lead to the discovery of new spintronic nanostructures, other than the presumed CISS spin filters.

In this dissertation we have explored single-molecule junctions beyond basic charge transport. We recognize that single-molecule junctions, despite the difficulty to realize, are an extraordinary platform for nanoscale physics, distinct from other solid state systems. To observe the exotic physical phenomena or to create innovative device applications, we have studied the single-molecule spin and orbital effects by means of mechanics, thermoelectrics and spintronics. For the future of molecular electronics, it is inevitable to explore these systems with new experimental techniques and molecular designs. The field of molecular electronics, while it may never replace solid state electronic devices, will complement our understanding of nanoscale physics.

Acknowledgements

My PhD study started in 2019 but the journey of becoming a physicist began long ago. So I would like to briefly describe how I have come to this point in my life. When I was a kid, I was always fascinated by science and technology and I had a dream of becoming a scientist. I was never sure if I would ever become one because no one I knew studied in science, but it was something always in the bottom of my heart. In the year of 2009, I moved to London, Ontario, Canada, where I studied for my high school. The relaxing and liberal education environment allowed me to explore my interests and built up my confidence in scientific studies. I then moved to Montreal, Quebec, Canada for my undergraduate study in physics at McGill university. There, I met many talented fellow students and inspiring professors who really brought me into the world of physics. In my third and fourth year of undergraduate, I met Prof. Guillaume Gervais and Prof. Thomas Szkopek, who gave me the privilege to work in their labs for researching on new two-dimensional (2D) materials. This is the moment when I decided that I wanted to further pursue in physics and make my next step in graduate school. In 2016, I arrived in Delft, the Netherlands, and started my master degree in Applied Physics at TU Delft. During my master, I had the chances to work on different projects including two small projects with Dr. Marko Burghard for topological insulators in Stuttgart, Germany, and with Dr. Andres Castellanos-Gomez and Dr. Riccardo Frisenda for 2D materials in Madrid, Spain. For my master thesis project, I worked under Prof. Herre van der Zant in single-molecule electronic transport. Upon my graduation of master degree, I made a decision for the four-year commitment in a PhD position with Herre at Delft, where I would be exploring the spin aspects of molecular electronics.

The four years of PhD at Delft have been the most intense and weirdest time in my and many others' lives because of the global pandemic, Covid-19. From 2020 to 2022, more than half of my PhD duration, we went through lock-down, social distance, work from home, inflation...etc. This drastic change of life truly altered my expectation of a PhD study and it is a pity that I was not able to enjoy the PhD program as much as I would like to. Nonetheless, thank to the people around me and the great effort in the public heath care, I was able to complete my PhD degree on time even during this tough time. I would like to acknowledge as much as I can here for all the help I have received.

The first person I would like to thank is my promoter, **Herre**. I am grateful for this PhD position you offered to me during my master thesis project. I am thankful that you always granted me a lot of freedom to explore in experiments and you always gave me fast feedback on my work. I really appreciate your presence in the lab, particularly during the time of Covid. It was a great honour for me to work in your lab and I truly learned the way of scientific thinking and how to become an independent researcher under your supervision. I wish you good health and

amazing time both inside and outside of research.

The second person I would like to acknowledge is my second promoter, **Jos**. Thank you for the helping me throughout my master and PhD studies at Delft. You are really an amazing educator who really cares about students and their future. It was a pleasure to be in the same research project with you and your theoretical insight really deepens my understanding of physics.

I would also like to thank the committee members of my PhD defence. **Marcel**, thank you for being part of my committee and all the discussions we had over the years of collaboration. It was amazing to work with your students and the molecules from Basel. **Fabian**, thank you for joining my PhD committee. I really appreciate the theoretical knowledge you have brought to us in understanding how electronic transport works at the single-molecule level. I enjoyed the meetings we had over the years, even though we had never met in person. **Ferdinand**, thank you for being in my PhD committee. It was nice work with you and to be in the same research project with you. **Nicolás**, thank you for being part of my committee. It was always nice to meet you at conferences and listen to your talks in STM break junction and thermopower. **Pascal**, thank you for being in my PhD committee. You are a great experimental scientist and it was really a pleasure to work with you in person and remotely after you left Delft. I learned a lot of experimental knowledge from you and I picked up a few interesting research directions from you. The crazy ideas and pragmatic skills you have always amazed me. I hope you continue to succeed in academia and I would always be curious about your research. **Yaroslav**, thank you for being the reserve member of my PhD committee. You are a great professor who really helps the students in classes and the QN department.

Next I would like to acknowledge a few members in the lab who helped me through out the years. **Luca**, I was lucky to start my PhD degree at almost the same time as you. It was pleasure to be your fellow PhD student, and I think without you being around, I might not have completed my degree. Thank you for all helps, tips and all the conversations we have over the years. You are the most reliable and trustworthy person and I really appreciate your company during my PhD. **Maria**, it was nice to know you and work with you during the first two years of my PhD. You are a kind-hearted and caring person for everyone around you. I really wish that you could have a better time at Delft, but bad things eventually pass and I hope you will enjoy more of you life. **Davide**, I was lucky to have you as my supervisor during my master thesis project. You encouraged me to become a researcher and really helped me in developing skills in scientific research. I enjoyed the old days when we discussed video games and all kinds of things outside of science. I wish you a great future. **Alfredo**, although we only had a few months of overlap at Delft before you moved away, it was nice to have you around with your bright and uplifting spirit. I wish you the best for your PhD and I really hope we will meet once again in the future. **Damian**, at first I didn't quite understand your way of working, but over the years you have shown that you are a careful and persistent researcher. As I told you several times, I believe that you are a very talented person, and I wish you the best for the rest of your PhD. **Serhii**, it was very nice to have you around and introduce you to all the experiments. I really enjoyed working with

you and I hope that you will continue with your enthusiasm in physics. **Tristan**, I am happy that I had supervised you for your master thesis project. You are smart and good at problem solving. I hope that you will find something that you are passionate about during your PhD journey. **Sebastiaan**, you started your PhD at worst time of Covid and you have overcome the difficult moments. I hope that you can enjoy your PhD now more by trying out new experiments. **Jacqui**, it was very nice to have you around. You brought up the spirit to the group and positive energy to the people around you. I hope it will go smoothly for your PhD defence, too. **Joeri**, thank you for the amazing legacy you left in the lab. Electromigration, insepctra gadget, etc. really helped me a lot during my PhD. You are an amazing scientist and your advice is really helpful to me. **Sabina**, it was very nice to meet you when you were a postdoc in the group. You were very friendly and helpful to other students around you. I wish all the best for your academic career. **Ignacio**, thank you for helping out during my master project. I missed the lunch time we had as a group back then. **Josep**, it was always great to discuss about physics and experiments with you. If I knew you earlier, I might have started working on spintronics and 2D materials. **Talieh**, you always brought good insights and helpful ideas in scientific discussions. It was pleasure to meet you and I enjoyed the conversations we had. **Diana**, I really appreciate the yearly visit of you from Chile. You are fun and always brought us good energy in the group. Your crazy ideas always work and I think there is some magic in them. **Nikos**, it was a lot of fun talking to you. You crazy 2D material stacks are fascinating to me.

I also want to acknowledge the four master students I have supervised during my PhD: Tristan, Emma, Coen and Sam. **Emma**, you were a joyful member to have in the lab during the difficult time of Covid. I hope that you thrive in your career. **Coen**, I really appreciate your persistent attitude during your master thesis project. You are open-minded and willing to learn, which are very good qualities of you. **Sam**, you are very bright and you can grasp abstract ideas very quickly. I really think you can be a good researcher, but you should change your habit of sending emails at 4 a.m. Do something you enjoy and are passionate about after your graduation.

Next I would like to acknowledge the people in the department for their help during my PhD. **Martin**, my fellow McGill senpai, it was great to meet you here at Delft during my master and later shared the same office with you. You were the most hardworking PhD student I have ever met. Thank you for the helps and advice during my PhD. I really enjoyed all the time we spent together either in the office or having a tea break. **Thierry**, you were probably the most funny person in the QN department. I enjoyed the chats with you and the fun we had together during the PhD, like the nitrogen ice cream and BBQ. **Edouard**, thank you for the scientific discussions and conversations over all ranges of topics. You always brought up interesting view points of things and I learned a lot from you. **Makars**, you are an amazing scientist. Thank you for sharing your knowledge and experiences with me. It was nice to be your office mate. **Kars**, you are a kind and humble physicist with a lot of knowledge of the CISS effect. I am very happy to be on the same project as you. **Abbey**, thank you for the cool chiral molecules you synthesized.

It was nice to have you on the same project. **Ulderico**, you are a persistent and talented researcher. I like the jokes you made and I hope the best for you PhD journey. **Maurits, Gabriele**, you were the hidden van der Zant members. I hope that you can keep the strong tie between TNW and 3ME, and best luck for you PhDs. **Sonakshi**, it was amazing to have to around in QN. Thank you for arranging all the social events and creating a better mood in the department. I was lucky to start the PhD at the same time as you. **Luigi**, I like your jokes and positive energy in QN. Thank you for making QN a better place and I wish you the best for the academic career. **Helena**, good luck with the QN blog. I hope you will make it a QN tradition. **Toeno**, thank you for being my advisor. I appreciate the time you offered me for consultation and they really helped me. I want to thank all the **QN, Kavli staff** for the support, which makes things possible here. Special thanks to **Heleen**, **Etty** for the administration; **Tino**, **Allard**, **Ronald** for their technical support; **Marc**, **Marco**, **Bas**, **Charles**,**Eugene**, **Pauline**, **Roald**, **Hozanna**, **Lodi**, **Arnold**, **Anja** for all the clean room helps. It wouldn't be possible to do research without your contributions.

———————————- External ———————————-

I also want to acknowledge people outside of TU Delft for the helps and contributions. **Juan**, thank you for coming to Delft for the 3 months. It was very fun to hang out with you and your presence really lighted up the mood of the people around you. **Andres** and **Riccardo**, you were amazing experimental physicists. I really admire you pragmatic program solving skills, and how you can get interesting material properties out of seemly trivial matters. I enjoyed the time we spent together in Madrid and you really inspired me a lot. **Marko** and **Katharina**, thank you for hosting me at Max Planck during my master short project. I learned a lot of things from you and I enjoyed the Pingpong time we had. **Patrick, Ksenia, David**, thank you for your amazing molecules. I enjoyed the conferences we had and it was really nice to work with you guys. **Werner**, thank you for the theoretical support and collaboration. It was nice to collaborate with you.

It is also important for me to acknowledge my former supervisors from McGill because without them, I would not have been so interested in research. **Vahid**, you were most amazing postdoc I have ever met. I really appreciated the time you spent with me on research and I truly thank you for teaching me all the things about physics and 2D materials. **Thomas**, you were a great professor who really educated the students well not just scientifically but also personally. I am genuinely thankful for having opportunity to work in your lab and learn from you. I hope that I would see you again one day in the future. **Guillaume**, thank you for giving the opportunity to work in your lab. You were a friendly professor and really give the students the chances to explore and flourish. I wish the best for you.

Finally I want to thank my family for supporting me during my pursuit of education. In particular, I want to thank my **Dad** for the years of support when I was abroad. I know it was financially a burden especially during my bachelor degree. Thank you for raising me and provide me the opportunities to explore the world. I also want to thank my older **Sister** for the mental support over the years. Finally,

I want thank my wife **Min** for being with me during my PhD years. It was tough time for us because of the Covid, and the intense PhD program made it worst for me. Thank you for the company and I hope that we are able to explore the world again.

Curriculum Vitæ

Chunwei Hsu

13-03-1994 Born in Tainan, Taiwan.

Education

2009-2012 **High School**
H.B. Beal Secondary School, London, Ontario, Canada

2012–2016 **Bachelor in Physics** (First-class honours)
McGill University, Montréal, Québec, Canada
Thesis: Electronic and Magneto Transport Properties of Two-Dimensional Bismuth (111) Quantum Well
Supervisors: Prof. dr. G. Gervais and Prof. dr. T. Szkopek

2016–2018 **Master in Applied Physics** (Cum laude)
Delft University of Technology, Delft, The Netherlands
Project 1: Magnetotransport of $Bi_2Te_2Se/RuCl_3$ van der Waals heterostructure
Supervisors: Dr. M. Burghard and Prof. dr. K. Kern
(Max Planck Institute of Solid State Research, Stuttgart)
Project 2: 2D transition metal dichalcogenide thermoelectric & optical properties
Supervisors: Dr. A. Castellanos-Gomez and Dr. R. Frisenda
(Instituto de Ciencia de Materiales de Madrid, Madrid)
Thesis: Single-Molecule Transport in Mechanically Flexible Molecules
Supervisors: Prof. dr. H. S. J. van der Zant
(Delft University of Technology, Delft)

2019–2022 **PhD. in Physics**
Delft University of Technology, Delft, The Netherlands
Dissertation: Conformational and Spin Effects in Single-Molecule Electronic Transport
Promotors: Prof. dr. H. S. J. van der Zant
Prof. dr. J. M. Thijssen

List of Publications

16. S. Volosheniuk, D. Bouwmeester, **C. Hsu**, P. Gehring, H. S. J. van der Zant. *Yu-Shiba-Rusinov states revealed by thermocurrent spectroscopy*, in preparation.

15. T. Bras, **C. Hsu**, D. Vogel, M. Mayor, H. S. J. van der Zant. *Strong asymmetrically coupled Kondo effect in mechanically controlled break junction*, in preparation.

14. *S. Golightly, ***C. Hsu**, H. S. J. van der Zant. *Electromigration break junction with copper*, in preparation.

13. *S. van der Poel, *J. Hurtado-Gallego, **C. Hsu**, K. Reznikova, M. Mayor, N. Agraït, H. S. J. van der Zant. *Quantum-interference-enhanced thermoelectric effects in paracyclophane molecules*, in preparation.

12. S. Volosheniuk, D. Bouwmeester, **C. Hsu**, P. Gehring, H. S. J. van der Zant. *Implementation of SNS thermometers into molecule devices for cryogenic thermoelectric experiments*, in preparation.

11. **C. Hsu**, M. Rohde, G. Borin Barin, G. Gandus, D. Passerone, M. Luisier, R. Fasel , H. S. J. van der Zant, M. El Abbassi. *9-atom armchair graphene nanoribbon in a platinum nanogap field effect transistor*, in preparation.

10. ***C. Hsu**, *W. M. Schosser, *P. Zwick, D. Dulić, M. Mayor, F. Pauly, H. S. J. van der Zant. *Mechanical compression in cofacial porphyrin cyclophane pincers*, Chem. Sci. **13**, 8017-8024, (2022).

9. **C. Hsu**, T. A. Costi, D. Vogel, C. Wegeberg, M. Mayor, H. S. J. van der Zant, P. Gehring. *Magnetic Field Universality of the Kondo Effect Revealed by Thermocurrent Spectroscopy*. PRL **128**, 147701, (2022).

8. *W. M. Schosser, ***C. Hsu**, *P. Zwick, K. Beltako, D. Dulić, M. Mayor, H. S. J. van der Zant, F. Pauly. *Mechanical Conductance Tunability of a Porphyrin–Cyclophane Single-Molecule Junction*. Nanoscale **14**, 984–992, (2022).

7. E. Pyurbeeva, **C. Hsu**, D. Vogel, C. Wegeberg, M. Mayor, H. S. J. van der Zant, J. A. Mol, P. Gehring. *Controlling the Entropy of a Single-Molecule Junction*. Nano Lett. **21**, 9715–9719, (2021).

6. *K. Reznikova, ***C. Hsu**, *W. M. Schosser, A. Gallego, K. Beltako, F. Pauly, H. S. J. van der Zant, M. Mayor. *Substitution Pattern Controlled Quantum Interference in [2.2]Paracyclophane-Based Single-Molecule Junctions*. J. Am. Chem. Soc. **143**, 13944–13951, (2021).

5. P. Gehring, J. K. Sowa, **C. Hsu**, J. de Bruijckere, M. van der Star, J. Le Roy, L. Bogani, E. M. Gauger, H. S. J. van der Zant. *Complete Mapping of the Thermoelectric Properties of a Single Molecule*. Nat. Nanotechnol. **16**, 426–430, (2021).

4. *P. Zwick, ***C. Hsu**, M. El Abbassi, O. Fuhr, D. Fenske, D. Dulić, H. S. J. van der Zant, M. Mayor. *Synthesis and Transport Studies of a Cofacial Porphyrin Cyclophane*. J. Org. Chem. **85**, 15072–15081, (2020).

3. F. Carrascoso, G. Sánchez-Santolino, **C. Hsu**, N. M. Nemes, A. Torres-Pardo, P. Gant, FJ. Mompeán, K. Kalantar-zadeh, J. A. Alonso, M. García-Hernández, R. Frisenda, A. Castellanos-Gomez. *Direct Transformation of Crystalline MoO_3 into Few-Layers MoS_2*. Materials (Basel). **13**, 2293 (2020).

2. **C. Hsu**, R. Frisenda, R. Schmidt, A. Arora, S. M. Vasconcellos, R. Bratschitsch, H. S. J. van der Zant, A. Castellanos-Gomez. *Thickness-Dependent Refractive Index of 1L, 2L, and 3L MoS_2, $MoSe_2$, WS_2, and WSe_2*. Adv. Opt. Mater. **7**, 1900239 (2019).

1. D. Stefani, K. J. Weiland, M. Skripnik, **C. Hsu**, M. L. Perrin, M. Mayor, F. Pauly, H. S. J. van der Zant. *Large conductance variations in a mechanosensitive single-molecule junction*. Nano Lett. **18**, 5981-5988, (2018)

*Authors contributed equally

Figure 1: Cover art of by C. Hsu for the publication titled *Mechanical compression in cofacial porphyrin cyclophane pincers*.